Microkinetic Modeling of the Oxygen Evolution Reaction on Iridium- and Ruthenium-based Catalysts

Zur Erlangung des akademischen Grades eines
Doktors der Ingenieurwissenschaften (Dr.-Ing.)
von der KIT-Fakultät für Elektrotechnik und Informationstechnik des
Karlsruher Instituts für Technologie (KIT)

angenommene
Dissertation
von

Janis Geppert, M. Sc.

Tag der mündlichen Prüfung:	12. Juli 2024
Hauptreferentin:	Prof. Dr.-Ing. Ulrike Krewer
Korreferent:	Prof. Dr. rer. nat. Michael Eikerling

Kurzfassung

Die Protonen-Austausch-Membran-Elektrolyse wird aktuell als eine der erfolgversprechendsten Technologien für die Produktion von Wasserstoff innerhalb eines auf erneuerbaren Energien basierenden Energiessystems gesehen. Hierbei wird Wasser durch das Anlegen eines elektrischen Potentials in seine Bestandteile Wasserstoff und Sauerstoff gespalten. Die Leistungsfähigkeit der Wasserspaltung wird im Wesentlichen durch die träge Sauerstoffentwicklungsreaktion (OER) bestimmt, in der Wasser zu Protonen und molekularem Sauerstoff reagiert. Zur Beschleunigung dieses Anodenprozesses auf technisch relevante Umsatzraten bedarf es Katalysatoren, die eine hohe Aktivität und Stabilität aufweisen. Durch exzessives Materialscreening konnten stabile Ir- und performante Ru-basierte Übergangsmetalloxide identifiziert werden. Dennoch weisen selbst diese modernsten Katalysatoren hohe kinetische Verluste in Form von Überpotentialen von mehreren hundert Millivolt auf. Um die Verbesserung der OER voranzutreiben, ist nun ein fundamentales Verständnis einzelner Reaktionsschritte sowie quantitative Einblicke in deren Thermodynamik und Kinetik erforderlich.
In dieser Dissertation wird erstmalig ein umfassendes und dynamisches Mikrokinetik-Modell der OER entwickelt und mit cyclovoltammetrischen Experimenten validiert, um die individuellen Prozesse an den Katalysatoren zu analysieren. Die experimentell beobachtbare Oxidation der Katalysatoroberfläche und die damit verbundene Bildung von Intermediaten werden in Form von reversiblen Adsorptionsreaktionen modelltechnisch nachgebildet. Das resultierende System an Ratengleichungen wird bilanziert, mittels kinetischer Ratenkonstanten oder thermodynamischer Energiewerte parametriert und hinsichtlich seines Verhaltens auf einen dynamischen Potentialinput simuliert. Die direkte Reproduktion elektrochemischer Experimente dient der Modellvalidierung. Hiermit wird eine Quantifizierung der mechanistischen Reaktionspfade, der entstehenden Intermediate an der Oberfläche, der Reaktionsraten einzelner Schritte und essentieller, thermodynamischer Eigenschaften ermöglicht. Die Studien fokussieren sich auf unterschiedlich strukturierte Materialien: Das hydrierte Ir, die rutilen Übergangsmetalloxide IrO_2 und RuO_2 sowie binäre Übergangsmetalloxidmischungen basierend auf Ir und Ru.
Zunächst wurde ein grundlegendes mikrokinetisches Modell für die Mechanismusaufklärung der OER an hydiertem Ir etabliert und hiermit der dominierende Reaktionsmechanismus aus mehreren Varianten identifiziert. Die Simulationen implizieren eine überwiegende Sauerstoffproduktion über einen Reaktionspfad an einem einzigen aktiven Zentrum. Die Oxidationszustände des Katalysators können auf Basis des validierten Modells analysiert werden und liegen

zu etwa 7 % Ir(III), 25 % Ir(IV) und 63 % Ir(V), bei einem typischen OER Potential von 1,6 V gegenüber der reversiblen Wasserstoffelektrode, vor. Durch die quantitative Analyse der Intermediate und Reaktionsraten kann das kontraintuitive Auftreten einer reduzierten Ir-Spezies bei stark oxidierenden Potentialen durch eine kinetische Limitierung der Wasseradsorption erklärt werden.
Des Weiteren wurde das Modell durch die implizite Berücksichtigung thermodynamischer Energien erweitert. Mit dieser weiterentwickelten Methodik wurde erstmalig das Leistungs- und das Degradationsverhalten des aktuellen Standardkatalysators IrO_2 umfassend und quantitativ analysiert. Dabei zeigt sich, dass die OER maßgeblich durch drei Reaktionsschritte limitiert wird. Diese sind die Adsorption von Wasser, ein potentialgetriebener Deprotonierungsschritt und die Abspaltung von molekularem Sauerstoff. Ein wissenschaftlicher Durchbruch besteht darin, dass es mit der in dieser Dissertation entwickelten Methodik erstmalig möglich ist, degradierte Zustände des Katalysators tiefgreifend und quantitativ zu untersuchen. Im Ergebnis korreliert die Abnahme der elektrokatalytischen Aktivität mit einem Anstieg der Aktivierungsenergie aller Deprotonierungsschritte. Da die Auswirkungen elektrolytbezogener Parameter nicht zu einer solchen Abnahme führen, wird in der modellbasierten Analyse deutlich, dass die Ursache des Leistungsverlustes auf Materialveränderungen zurückzuführen ist.
Neben reinen Ir-Oxiden wurde die Methodik anschließend auch auf das Rutil RuO_2 und auf binäre Übergangsmetalloxide $Ir_xRu_{1-x}O_2$ angewandt, um den Einfluss der Materialzusammensetzung auf die Leistungsfähigkeit zu analysieren. Die Oberflächen der Mischungen weisen aktive Zentren sowohl aus Ir als auch aus Ru auf, an welchen die OER unabhängig und bei unterschiedlichen Überspannungen abläuft. Die potentialbestimmenden Reaktionsschritte an beiden Zentren unterscheiden sich und sind im Speziellen die Bildung der adsorbierten Spezies $^*OOH$ an RuO_2 und $^*OO$ an IrO_2. Werden beide Komponenten zu einem binären Übergangsmetall gemischt, bewirkt dies einen synergetischen Effekt, durch den die Reaktionsenergien der limitierenden Schritte abgesenkt werden und somit eine effizientere OER ermöglichen.
Mit der in dieser Dissertation erabeiteten modellbasierten Methodik wurde es erstmalig ermöglicht, die individuellen Prozesse der OER umfassend und quantitativ zu analysieren. Die Analyse umfasst sowohl die Thermodynamik und Reaktionskinetik sowie deren Effekte auf die Leistungsfähigkeit von initialen und insbesondere auch von degradierten Katalysatorzuständen. Aufgrund der erfolgreichen Untersuchungen verschiedener Katalysatormaterialien suggeriert der Ausblick dieser Arbeit, dass sich die Methodik als übertragbar und vorteilhaft für die zukünftige Analyse weiterer Elektrokatalysatoren und elektrokatalytischer Reaktionen erweisten wird.

Abstract

The proton exchange membrane electrolysis is currently seen as one of the most promising technologies for hydrogen production within an energy system based on renewable energies. In this process, water is split into its components, hydrogen and oxygen, by applying an electrical potential. The performance of water splitting is determined by the sluggish oxygen evolution reaction (OER), in which water reacts to protons and molecular oxygen. In order to accelerate this anode process to technically applicable conversion rates, highly active and stable catalysts are needed. Through excessive material screening, stable Ir- and active Ru-based transition metal oxides have been identified. Nevertheless, even these state-of-the-art catalysts exhibit high kinetic losses in the form of overpotentials of several hundred millivolts. A fundamental understanding of individual reaction steps and quantitative insights into their thermodynamics and kinetics is required to advance the improvement of the OER.

In this dissertation, a comprehensive and dynamic microkinetic model of the OER is developed for the first time and validated with cyclic voltammetry experiments to analyze the individual processes at the catalysts. The experimentally observable oxidation of the catalyst surface and the associated formation of intermediates are modeled in terms of reversible adsorption reactions. The resulting system of rate equations is balanced, parameterized using kinetic rate constants or thermodynamic energy values, and simulated for its behavior on a dynamic potential input. Direct reproduction of electrochemical experiments is used for model validation. The developed methodology allows quantification of the mechanistic reaction pathways, the intermediates formed at the surface, the reaction rates of individual steps, and essential thermodynamic properties. The studies focus on differently structured materials: the hydrous Ir, the rutile transition metal oxides IrO_2 and RuO_2, as well as binary transition metal oxide mixtures based on Ir and Ru.

At first, a fundamental microkinetic model was established to elucidate the mechanism of the OER on hydrous Ir, and thereby, the dominant reaction mechanism from several variants was identified. The simulations imply a predominant oxygen production via a reaction pathway at a single active site. The oxidation states of the catalyst can be analyzed based on the validated model and are present at about 7 % Ir(III), 25 % Ir(IV), and 63 % Ir(V), at a typical OER potential of 1.6 V versus the reversible hydrogen electrode. By a quantitative analysis of the intermediates and reaction rates, the counterintuitive occurrence of a reduced Ir species at strongly oxidizing potentials can be explained by a kinetic limitation of the water adsorption.

Furthermore, the model was extended by implicitly considering thermodynamic energies. With this advanced methodology, the performance and degradation behavior of the current standard catalyst IrO_2 was analyzed comprehensively and quantitatively for the first time. It is shown that three reaction steps significantly limit the OER. These are the adsorption of water, a potential-driven deprotonation step, and the detachment of molecular oxygen. A scientific breakthrough is that the methodology developed in this dissertation makes it possible for the first time to study degraded states of the catalyst in-depth and quantitatively. As a result, the decrease in electrocatalytic activity correlates with an increase in the activation energy of all deprotonation steps. Since the effects of electrolyte-related parameters do not lead to such a decrease, it becomes evident from the model-based analysis that the cause of the performance loss is due to material changes.

In addition to pure Ir oxides, the methodology was subsequently applied to the rutile RuO_2 and binary transition metal oxides $Ir_xRu_{1-x}O_2$ to analyze the influence of material composition on the performance. The surfaces of the mixtures exhibit active sites of both Ir and Ru, at which the OER proceeds independently and at different overpotentials. The potential-determining reaction steps at the two active sites differ and are in particular the formation of the adsorbed species $^*OOH$ at RuO_2 and $^*OO$ at IrO_2. Mixing both components to form a binary transition metal oxide results in a synergistic effect by which the reaction energies of the limiting steps are lowered, allowing for more efficient OER.

With the model-based methodology developed in this dissertation, it was possible for the first time to comprehensively and quantitatively analyze the individual processes of the OER. The analysis includes thermodynamics, reaction kinetics, and their effects on the performance of pristine and especially degraded catalyst states. Furthermore, due to the successful investigations of various catalyst materials, the outlook of this work suggests that the methodology will prove to be transferable and beneficial for the future analysis of further electrocatalysts and electrocatalytic reactions.

Acknowledgement

This dissertation covers the substantial results of my research work at the Institute of Energy and Process Systems Engineering and the Institute for Applied Materials – Electrochemical Technologies between 2018 and 2022. Many people supported me in completing this project during this time, and I would like to acknowledge them gratefully.

First of all, I sincerely thank my supervisor, Prof. Ulrike Krewer, for giving me the unique opportunity to conduct this research at her institutes, especially for her guidance, encouragement, and continuous support throughout the project. Further, I am grateful to Prof. Michael Eikerling for reviewing this dissertation as the second examiner.

I am particularly thankful to my group leaders, Dr. Philipp Röse and Dr.-Ing. Fabian Kubannek, for bringing their expertise and effort into the research project and to the students Ada Raya and Swantje Pauer for their contributions. I am grateful to all my colleagues who, with their inspiring work, achievements, and enthusiasm for science, have created an excellent research atmosphere at both institutes.

I also thankfully appreciate the scientific collaboration with all the partners in the SPP 2080 consortia research project. Thank you, especially Dr. Steffen Czioska, Dr. Daniel Escalera-López, Dr. Serhiy Cherevko, and Prof. Jan-Dierk Grunwaldt, for the collaboration and the fruitful discussions on such a high scientific level.

Finally, I would like to thank my wife and my family for their unlimited support.

Wolfsburg, July 2024 *Janis Geppert*

Publications within the Research of this Dissertation

Journal Publications

- **Geppert, J.**; Röse, P.; Czioska, S.; Escalera-López, D.; Boubnov, A.; Saraçi, E.; Cherevko, S.; Grunwaldt, J.-D.; Krewer, U. Microkinetic Analysis of the Oxygen Evolution Performance at Different Stages of Iridium Oxide Degradation. *J. Am. Chem. Soc.* **2022**, *144*, 13205-13217.

- **Geppert, J.**; Röse, P.; Pauer, S.; Krewer, U. Microkinetic Barriers of the Oxygen Evolution on the Oxides of Iridium, Ruthenium and their Binary Mixtures. *ChemElectroChem* **2022**, *10*, e202200481.

- **Geppert, J.**; Kubannek, F.; Röse, P.; Krewer, U. Identifying the Oxygen Evolution Mechanism by Microkinetic Modelling of Cyclic Voltammograms. *Electrochim. Acta* **2021**, *380*, 137902-137914.

- Escalera-López, D.; Czioska, S.; **Geppert, J.**; Boubnov, A.; Röse, P.; Saraçi, E.; Krewer, U., Grunwaldt, J.-D.; Cherevko, S. Phase- and Surface Composition-Dependent Electrochemical Stability of Ir-Ru Nanoparticles during Oxygen Evolution Reaction. *ACS Catal.* **2021**, *11*, 9300-9316.

- Czioska, S.; Boubnov, A.; Escalera-López, D.; **Geppert, J.**; Zagalskaya, A.; Röse, P.; Saraçi, E.; Alexandrov, V.; Krewer, U.; Cherevko, S.; Grunwaldt, J.-D. Increased Ir–Ir Interaction in Iridium Oxide during the Oxygen Evolution Reaction at High Potentials Probed by Operando Spectroscopy. *ACS Catal.*, **2021**, *11*, 10043-10057.

- Czioska, S.; Ehelebe, K.; **Geppert, J.**; Escalera-López, D.; Boubnov, A.; Saraçi, E.; Mayerhöfer, B.; Krewer, U.; Cherevko, S.; Grunwaldt, J.-D. Heating up the OER: Investigation of IrO_2 OER Catalysts as Function of Potential and Temperature**. *ChemElectroChem* **2022**, *9*, e202200514.

Conference Contributions

- **Geppert, J.**; Kubannek, F.; Röse, P.; Krewer, U. Identifying the Oxygen Evolution Mechanism by Microkinetic Modelling of Cyclic Voltammograms. *29th Topical Meeting of the International Society of Electrochemistry* **2021** (Talk).
- **Geppert, J.**; Röse, P.; Krewer, U. Monitoring Catalytic Changes by Microkinetic Modelling of the Oxygen Evolution Reaction. *12th European Symposium on Electrochemical Engineering* **2021** (Talk).
- **Geppert, J.**; Röse, P.; Krewer, U. The Microkinetic Performance Barriers of Ruthenium and Iridium Oxides during the Electrocatalytic Oxygen Evolution Reaction. *241st Electrochemical Society Meeting* **2022** (Talk).
- **Geppert, J.**; Röse, P.; Krewer, U. Microkinetic Modelling of the Oxygen Evolution Reaction (OER) on Hydrous Iridium. *54. Jahrestreffen Deutscher Katalytiker* **2021** (Poster).

Contents

Kurzfassung . . . . . **i**

Abstract . . . . . **iii**

Acknowledgement . . . . . **v**

Publications within the Research of this Dissertation . . . . . **vii**

1 Introduction **1**
1.1 Motivation 1
1.2 Current State and Objective 2
1.3 Scope and Structure of this Work 4

2 Microkinetic Modeling of Electrocatalytic Processes **5**
2.1 Principles of Electrocatalytic Water Splitting 5
2.2 Fundamental Description of the Surface Processes 8
2.2.1 Electrocatalytic Reaction Kinetics 8
2.2.2 Adsorption Isotherms 11
2.3 Experimental Methods 12
2.4 Microkinetic Model Developement 13
2.4.1 Model Equations and Parameters 14
2.4.2 Implementation 16
2.5 Model Analysis 16
2.5.1 Parameter Variations 17
2.5.2 Comparison of the Adsorption Isotherms 20
2.6 Concluding Remarks 22

3 Identification of the OER Mechanism on hydrous Iridium **23**
3.1 Introduction 23
3.2 Methods 25
3.2.1 Experimental Setup 25
3.2.2 Mechanistic Assumptions 25

3.2.3 Microkinetic Model Equations . . . 28
3.2.4 Simulation and Model Parameter Identification . . . 29
3.3 Results and Discussion . . . 30
3.3.1 Experimental Results . . . 30
3.3.2 Analysis of Adsorption Isotherms . . . 31
3.3.3 Model Parameters . . . 33
3.3.4 Microkinetic Insights of Mechanism M1 . . . 36
3.3.5 Microkinetic Insights of Mechanism M2 . . . 37
3.3.6 Surface Coverage of Intermediate Species and Oxidation States . . . 38
3.3.7 Thermodynamic Analysis . . . 39
3.4 Concluding Remarks . . . 41

4 Analysis of the Oxygen Evolution Performance at Different Stages of Iridium Oxide Degradation . . . 43
4.1 Introduction . . . 43
4.2 Methods . . . 45
4.2.1 The OER Mechanism on Rutile IrO_2 . . . 45
4.2.2 Microkinetic Model . . . 46
4.2.3 Model Parameterization . . . 47
4.2.4 Experimental Characterization . . . 48
4.3 Results and Discussion . . . 50
4.3.1 Experimentally Observed Electrocatalytic Behavior . . . 50
4.3.2 Energies and Further Model Parameters . . . 54
4.3.3 Interplay of Surface Processes and their Kinetic Impact . . . 58
4.3.4 Polarization Behaviour . . . 61
4.3.5 Kinetic Changes due to Degradation . . . 63
4.4 Concluding Remarks . . . 67

5 Microkinetic Barriers of the Oxygen Evolution on the Oxides of Iridium, Ruthenium and their Binary Mixtures . . . 69
5.1 Introduction . . . 69
5.2 Methods . . . 71
5.2.1 Experimental Characterization . . . 71
5.2.2 The OER Mechanism on Rutile Oxides . . . 72
5.2.3 Model Equations and Parameterization . . . 72
5.3 Results and Discussion . . . 73
5.3.1 Experimental Dynamic Current Response . . . 74
5.3.2 Kinetic Analysis of the OER at RuO_2 and IrO_2 . . . 76
5.3.3 Kinetic Analysis of the OER at Oxide Mixtures of $Ir_xRu_{1-x}O_2$ . . . 80

5.4 Concluding Remarks 85

6 Conclusion and Outlook 87
6.1 Conclusion 87
6.2 Outlook 89

Bibliography 91

List of Symbols and Abbreviations 105

A Modeling Details 109
A.1 Model Code of a PCET 109
A.2 Parameter Identification Process 114
A.3 Profile rmse Analysis 117
A.4 Simulations with Different Scan Rates 119
A.5 Simulations with Fixed Energy Values 121
A.6 Coverages of Adsorbed Species 122
A.7 Model Parameter Values 124

1 Introduction[1]

1.1 Motivation

While realizing a sustainable energy supply based on renewable resources, such as wind and solar energy, efficient conversion and storage strategies are needed.[4] One key technology is the proton exchange membrane (PEM) electrolysis due to its high performance in the electrocatalytic splitting of water into hydrogen and oxygen.[5, 6] It offers the advantages of a high current density operation at a pressure of up to 30 bar to approach the requirements of high-pressure storage and enables the production of pure hydrogen under dynamic operation conditions to follow the intermittent production of renewable electricity.[7, 8] To provide a high and durable efficiency, costly but electrocatalytically active and stable catalysts are required at both electrode processes: while the cathodic hydrogen evolution reaction (HER) $2\,H^+ + 2\,e^- \rightarrow H_2$ is efficiently catalyzed using carbon-supported Pt nanoparticles[9], its anodic counterpart the splitting of water in the oxygen evolution reaction (OER) $2\,H_2O \rightarrow 4\,H^+ + 4\,e^- + O_2$ is heavily limited by the sluggish and complex reaction kinetics.[6] In the last decades, multiple OER catalysts that resist the local acidic conditions have been screened.[7, 10, 11] Among them, Ir- and Ru-based materials were found to outperform most of the active transition metals and their oxides. While RuO_2 exhibits the highest electrocatalytic activity, IrO_2 provides excellent stability under the harsh OER process conditions with strongly oxidizing potentials in acidic media and still has reasonable activity properties.[12, 13] Enhanced Ir activity can be achieved by an electrochemical material treatment that produces so-called hydrous Ir. However, this modified catalyst is less stable than IrO_2.[14] So far, the most promising catalyst results from the combination of Ir and Ru oxides, as it benefits from both the high OER activity found for RuO_2 and the high stability of IrO_2.[15]
Despite the recent progress in the research field of OER catalysts, the primary performance loss in PEM electrolyzer cells is still attributed to the sluggish OER kinetics. It is quantified with an overpotential of about 350 mV at a current density of 3 A cm^{-2} on the state-of-the-art

[1] Parts of this chapter have been published in the following articles:
[1] **Geppert, J.**; Röse, P.; Czioska, S.; Escalera-López, D.; Boubnov, A.; Saraçi, E.; Cherevko, S.; Grunwaldt, J.-D.; Krewer, U. *J. Am. Chem. Soc.* **2022**, *144*, 13205-13217.
[2] **Geppert, J.**; Röse, P.; Pauer, S.; Krewer, U. *ChemElectroChem* **2022**, *10*, e202200481.
[3] **Geppert, J.**; Kubannek, F.; Röse, P.; Krewer, U. *Electrochim. Acta* **2021**, *380*, 137902-137914.

IrO_2 catalyst.[6] An in-depth understanding of the reaction kinetics of the intermediate and product species formation and the kinetically and thermodynamically limiting processes is urgently needed to optimize the catalysts. Experimental characterization methods reach their limits in quantifying and distinguishing between very fast processes occurring simultaneously. Hence, model-based approaches are more promising for a comprehensive analysis. At this point, kinetic modeling can contribute to insights into current scientific questions, which are:

- How can the complex electrocatalytic processes on Ir- and Ru-based anodes be described comprehensively in terms of modeling?
- How do the material structure and composition affect the reaction kinetics of intermediate and product species formation during a dynamic OER operation?

The motivation for this work stems from addressing the current research questions by providing an in-depth understanding of the kinetic limitations in electrocatalytic water splitting for a knowledge-based performance improvement in the energy conversion process in PEM electrolyzers. An appropriate modeling methodology is required to achieve this goal, as addressed in the first question. Since several approaches are already established and applied for the OER, a brief introduction to the current state is given, and the methodical objectives are derived in the following section. In the section after that, this dissertation's scope and structure are presented.

1.2 Current State and Objective

The catalytic activity of a material is typically calculated based on the density functional theory (DFT) or modeled using a reaction kinetic approach. In early publications, Rossmeisl et al. were able to link the OER activity of several materials to DFT-calculated binding energies of adsorbed intermediate species.[16, 17] This approach is commonly used to predict thermodynamically favorable surface species *ab initio* and is conducted for a wide range of electrocatalytic reactions. However, the calculations are restricted to the steady-state of thermodynamic equilibrium and ideal and well-defined catalyst surfaces. Various nanoparticles with different facets and edges, as well as amorphous or hydrous materials are typically deployed in PEM electrolyzers. The catalysts also tend to degrade during operation, which is assigned with a change in the surface near material structure and, thus, the thermodynamics. Since the actual active catalyst structure and surface present during the OER are not fully characterized in most cases, one lacks the input for the DFT-based calculations, and the main benefit of the *ab initio* approach diminishes. Instead, experimental validation of the results becomes necessary to guarantee correct results. In recent publications, DFT outcomes are correlated to the results of cyclic voltammetry (CV)[18–21] and surface-enhanced infrared absorption spectroscopy experiments[22] on well-defined material structures for validation. Despite the recent progress, DFT-based approaches are still limited to

the assumption of an ideal catalyst structure and will be restrained to the steady-state condition. Hence, a more comprehensive and versatile description of the processes at non-ideal catalysts can be achieved by employing the reaction kinetics approach.
Unlike DFT-based calculations, reaction kinetics or microkinetic modeling focuses on the formation processes rather than the presence of surface species. Microkinetic modeling is commonly based on the Butler-Volmer equation or the transition state theory and uses the rate equations of multiple reactions. They are used to calculate relevant variables, such as the current density and the surface coverage, as well as their behavior at an applied potential. Direct validation by experimental data is possible and allows quantifying reaction rates and identifying limiting steps within the overall electrocatalytic process. However, this method relies on assumptions such as the present surface species or mechanistic pathways, based on which the set of model equations is derived. To simplify the calculation, one of the following approximations is commonly taken into account: non-rate-determining steps are expected in quasi-equilibrium, or relevant variables, primarily the concentration of intermediates, are assumed to remain constant over time and fixed at steady-state.[23] However, both simplifications are accompanied by a loss of valuable insights. In particular, the number of unique Tafel slopes is underestimated[24], and the kinetic parameters[25], as well as the rate-determining step[26], are unidentifiable, especially if the step is similarly slow as another step or if it is substituted by a shift in potential[23]. Thus, the limitations of single steps are no longer identifiable by the comparison with experimental data.[24, 25] A promising way to overcome this downside is a kinetic model approach based on a comprehensive set of reaction rate equations, which can be simulated dynamically. Modeling without the quasi-equilibrium and steady-state approximations is crucial to perform simulations with dynamic inputs and no further restrains. Resulting models can reproduce multiple dynamic experiments such as CV[27–29] and potentiostatic mass transfer responses[30, 31], electrochemical impedance spectroscopy (EIS)[32–34], or nonlinear frequency response analysis[35–37]. They allow a more precise interpretation of measurements through the detailed analysis of processes at the catalyst surface. Such analyses would also benefit understanding the OER but have not been conducted so far. The main requirements for this modeling method are derived from the given delineation of the current state and are formulated in short as follows:

- Comprehensive description of electrocatalytic microkinetics
- Time-continuous modeling for dynamic simulations
- Validation and parameterization with experimental data
- Applicability to non-ideal or degraded catalyst materials

These requirements also give rise to the main objectives for the development of the model-based methodology to answer the scientific questions above. The scope and structure of how this will be realized in the present dissertation are presented in the following section.

1.3 Scope and Structure of this Work

This dissertation covers the derivation and development of a model-based methodology to attain the objectives described in the previous section. It is further analyzed and applied to describe and study the surface processes at selected Ir- and Ru-based catalyst surfaces during the electrocatalytic OER. Overall, this dissertation elaborates on the answers to the scientific questions formulated above by providing in-depth model-based and experimentally validated insights.
The following chapter describes the fundamentals of the OER on transition metal oxides based on the literature to give a basic understanding of the topic. It also includes findings on the occurring surface species, mechanistic insights, and the theoretical description of the electrochemical processes. In addition, the methodology of modeling the catalytic processes with kinetic rate equations is explained, and a fundamental analysis of the main model parameters and assumptions therein is conducted. The developed approach, including the experimental parameterization and validation method, is applied to OER electrocatalysts for various scientific purposes, as described in the following three chapters. Chapter three focuses on identifying the oxygen evolution mechanism at hydrous Ir. The subsequent chapter four describes the analysis of the oxygen evolution performance at different stages of Ir oxide degradation. Chapter five deals with the analysis of the microkinetic barriers of the oxygen evolution on the oxides of Ir, Ru, and their binary mixtures. After the in-depth analyses, a conclusion of the dissertation's main findings and the overall results, as well as a brief outlook, is given in chapter six.

2 Microkinetic Modeling of Electrocatalytic Processes[2]

This chapter provides an understanding of the principles of electrocatalytic water splitting and a fundamental description of the surface processes regarding available research. Based on these findings, a microkinetic description of a reaction system is derived. The resulting model is being analyzed using various parameter assumptions. It shows their effect on the model output and demonstrates that the model allows for dynamic simulations and the reproduction of experiments. Finally, this chapter will be concluded with a description of how this model provides the basis of the methodology for the kinetic analysis of the OER at transition metal oxides and how it allows addressing the scientific questions of this work in the following chapters.

2.1 Principles of Electrocatalytic Water Splitting

It is known that in PEM electrolyzer cells, the water-splitting process is mainly limited due to its reaction kinetics.[6] One solution for such bottlenecks in chemical engineering is the usage of suitable catalysts. They consist of metals, and their oxides or alloys, which interact with the reactant species and accelerate the formation of intermediate species. Instead of performing the overall reaction through molecular interaction alone, using catalytic materials supports additional pathways along the reaction coordinate. Consequently, they split the reaction into a series of intermediate steps with various activation energies. Thus, a substantial decrease in the maximum activation energy indicates a highly active catalyst and is usually correlated with a massive increase in the turnover of the desired reaction. This principle of such an active catalyst for water splitting is visualized schematically in Figure 2.1.

[2] Parts of this chapter have been published in the following article:
[1] **Geppert, J.**; Röse, P.; Czioska, S.; Escalera-López, D.; Boubnov, A.; Saraçi, E.; Cherevko, S.; Grunwaldt, J.-D.; Krewer, U. *J. Am. Chem. Soc.* **2022**, *144*, 13205-13217.

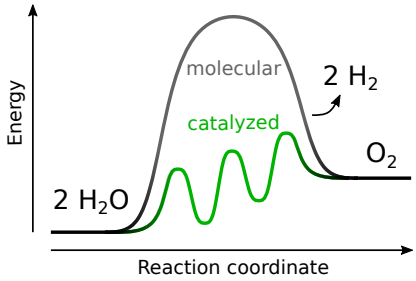

Figure 2.1: The principle of a catalyzed reaction is exemplified in the water-splitting reaction. The overall energy barrier of a molecular reaction is lowered due to the formation of multiple intermediate species along the reaction pathway.

In recent decades, the scientific community has focused on finding the most active catalytic materials for the water-splitting reaction given in equation 2.1.

$$2\,H_2O \rightarrow 2\,H_2 + O_2, \quad \Delta G^0 = 4.92\ \text{eV} \tag{2.1}$$

The Gibbs free energy ΔG^0 converted by the reaction under standard conditions can be calculated based on the thermodynamic principles.[38] In an electrochemical system, the water splitting reaction is divided into a reduction and an oxidation reaction, each with defined standard potentials E^0 and four transferred electrons. It was reported that the cathodic HER in equation 2.2 is best catalyzed with active and stable Pt. With this catalyst, only an overpotential of 15 mV is required to run the reaction effectively at a mass-specific current of 0.1 A mg^{-1} or the equivalent current density of 10 mA cm^{-2}.[9]

$$4\,H^+ + 4\,e^- \rightarrow 2\,H_2, \quad E^0 = 0\ \text{V} \tag{2.2}$$

The search for the optimal catalyst material for the OER, given in equation 2.3 for acidic media, is challenging since the complex reaction calls for both, high activity and stability under highly oxidizing potentials.

$$2\,H_2O \rightarrow 4\,H^+ + 4\,e^- + O_2, \quad E^0 = 1.23\ \text{V} \tag{2.3}$$

Various materials have been studied experimentally or based on calculations to identify the most suitable candidates.[7, 10, 13, 39, 40] The findings suggest transition metal catalysts and especially the very stable Ir-based and highly active Ru-based oxides, as the most beneficial. The material stability is measured in terms of the dissolution rate at a typical OER potential in acidic media. It shows a significantly lower value of 3 pg cm^{-2} s^{-1} for IrO_2, proving that it is more stable than RuO_2 with a value of 300 pg cm^{-2} s^{-1}.[12] The overpotentials define the catalytic activities and are quantified to 330 mV and 250 mV on IrO_2 and RuO_2 nanoparticles, respectively, with a transition metal mass-specific current of 0.1 A mg^{-1}.[41, 42] Although these overpotentials are among the lowest values observed so far for the OER[10, 43], they define the bottleneck of the overall water-splitting reaction, as they are still more than 16-fold higher than for the HER on Pt.

The processes and intermediate species occurring at the material surfaces are extensively studied to understand this limitation. Each electrocatalyst has properties, such as the physical material and electronic structure and its chemical composition, which affect the thermodynamics and kinetics of the OER in certain ways. They influence the formation of adsorbed intermediates and, thus, the pathway along the reaction coordinate, leading to a specific mechanism for each catalyst. Since the active sites of the materials form covalent bonds due to the chemical adsorption of electrolyte species, the oxidation state of the catalyst may change during the reaction. X-ray-based methods for physical characterization are, thus, widely exploited to observe the oxidation state and to investigate the underlying mechanism. Also, DFT-based calculations are used to study the thermodynamics of adsorbed species and to conclude on the energetically favorable pathway. This approach is auspicious since it can provide the highest energy barrier in the mechanism, which usually limits the turnover frequency, i.e., the rate at which the OER is operated. It is further a good value for estimating the experimentally observable overpotentials.

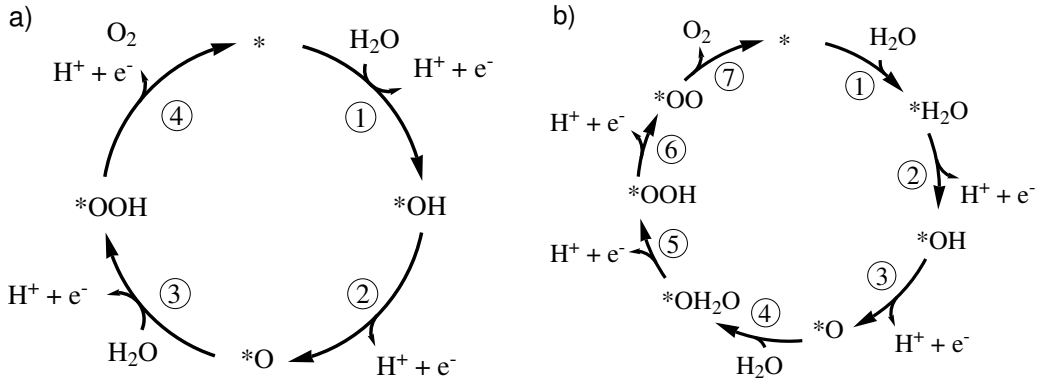

Figure 2.2: Mechanisms proposed for surface oxidation and the OER on IrO_2 and RuO_2 by a) Rossmeisl et al.[17], and b) Ping et al.[44] and Rao et al.[45].

Following the principles of electrocatalysis, the activity of IrO_2 and RuO_2 is explained by adsorbed intermediates that pave a thermodynamically efficient pathway alongside the reaction coordinate of the OER.[17, 46] It was concluded that the active site of the material consists of the coordinatively unsaturated site (CUS) denoted with *, on which the different species *OH, *O, and *OOH are formed depending on their specific binding energy.[17] These findings result in a simple four-step mechanism shown in Figure 2.2a: water is adsorbed from the electrolyte and deprotonated to form molecular oxygen in consecutive steps. Further studies reported that the steps of water adsorption and oxygen detachment play a crucial role during the OER.[44, 45, 47] By explicitly considering the involved intermediate species, namely $^*H_2O$, $^*OH_2O$, and *OO, the resulting mechanism is even more complex with seven reaction steps, as shown in Figure

2.2b. Each step in both mechanisms consists of either the adsorption or desorption of an electrolyte species with its reaction energy and energetic barrier to form an intermediate species on the catalytic surface. The following section explains how these individual steps can be described mathematically based on the available theoretical knowledge.

2.2 Fundamental Description of the Surface Processes

As the water-splitting reaction consists of several steps along a mechanistic pathway, a detailed characterization of each step is required to analyze its influence on the overall process. A fundamental mathematical description of the processes is well-established in the literature. It allows us to correlate the thermodynamics with the reaction kinetics and can, thus, link the energy levels at a given overpotential to the reaction rate and the current density. The essential equations described below lay the theoretical foundation for developing the microkinetic model.

2.2.1 Electrocatalytic Reaction Kinetics

In the scientific field of reaction kinetics, one of the most prominent and widely used concepts is manifested in the Arrhenius equation 2.4[48]:

$$k = k_0 \exp\left(\frac{-E_a}{k_B T}\right) \tag{2.4}$$

It describes the chemical rate constant k in dependence on the absolute temperature T and the activation energy E_a of a reaction with the pre-exponential factor k_0 and the Boltzmann constant k_B. As this equation is derived from empirical observations, only little mechanistic insights can be obtained from the pre-exponential frequency factor and the activation energy. To gain a fundamental understanding of both parameters, the transition state theory was developed, in which the transition state and the reactant state are assumed to be in quasi-equilibrium.[49, 50] Another approach, explicitly derived for electron transfer processes, is given in the Marcus theory.[51] Both theoretical concepts, though, are based on the assumption of an energy barrier, dividing the reactant and the product state. This barrier must be overcome to drive the reaction in either direction by applying a driving force, i.e., an electrical potential E for electrochemical reactions.[52] The effect of the potential on the energy states forming the barrier is shown schematically in Figures 2.3a and 2.3b. Using the Gibbs free energy G is convenient since such electrochemical processes occur at constant pressure p and constant temperature. Under electrochemical standard

conditions, the barrier energy $\Delta G^{\ddagger}$ for an elementary electron transfer step is written in equation 2.5 as an equivalent expression to the electrochemical potential.[53]

$$\Delta G^{\ddagger} = \Delta G_0^{\ddagger} \mp e\beta\Delta E \tag{2.5}$$

Here, β is the symmetry factor, e is the elementary charge, and $\Delta E = E - E^0$ is the difference in the applied potential and the potential at electrochemical standard conditions E^0. Rewriting the standard potential into the standard reaction free energy $\Delta G_r^0 = eE^0$ gives us a value that is only dependent on the energy difference of the reactant and product state. For an adsorption process, it can be identified as the difference in binding energies of adsorbed species. The energy term $\Delta G_0^{\ddagger}$ describes the kinetic activation free energy ΔG_a, which is equal in both, the forward and backward direction of the process.

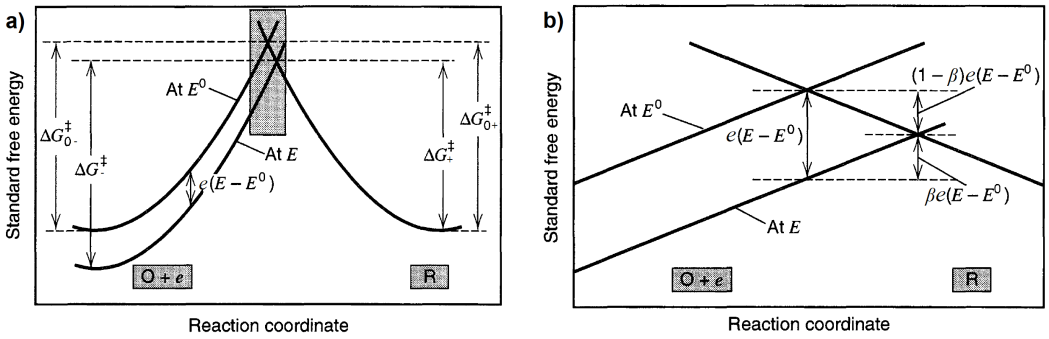

Figure 2.3: a) Schematic representation of an electrochemical energy barrier and the effect of an applied potential. b) Magnified picture of the shaded box in a). Both figures are slightly modified, taken from Bard et al.[52].

The rate constants for the process are defined by inserting the term of the barrier energy in equation 2.5 into Arrhenius equation 2.4. With the assumption of symmetric barriers (β = 0.5), equation 2.6 results for forward k_+ and backward k_- direction.

$$k_{\pm} = k_0 \exp\left(\frac{-\Delta G_{\pm}^{\ddagger}}{k_B T}\right) = k_0 \exp\left(\frac{-\Delta G_a \mp \beta\Delta G_r^0}{k_B T}\right) \tag{2.6}$$

It is worth noting here that in case of an asymmetrical barrier ($\beta \neq 0.5$), one would follow the notation in Figure 2.3 and use $(1-\beta)$ instead of β for the backward rate constant. However, a change in the symmetry factor does not influence the model output, as will be shown later in

section 2.5. Therefore, the following description is given with the assumption of $\beta = 0.5$. In any case, the equilibrium constant K is defined in equation 2.7 by the ratio of both rate constants.

$$K = \frac{k_+}{k_-} = \exp\left(\frac{-\Delta G_r^0}{k_B T}\right) \tag{2.7}$$

The expression for the reaction rates r in equation 2.8 is derived straightforwardly by multiplying the rate constant with the activity a of the respective reactant substance and the exponential term of the electric potential. Both terms are defined at non-standard conditions. This consideration becomes relevant, as by changing the activity to values other than unity or applying an electrode potential other than zero, the system is no longer in line with the electrochemical standard condition.

$$r_\pm = k_\pm \cdot a_\pm \cdot \exp\left(\frac{\pm \beta e E}{k_B T}\right) \tag{2.8}$$

For a one-electron transfer process on an electrode with a defined density of active sites ρ, the resulting current density can be calculated by multiplying the effective reaction rate with the elementary charge and the density of active sites in equation 2.9.

$$j = e\rho(r_+ - r_-) \tag{2.9}$$

Inserting equations 2.6 and 2.8 into equation 2.9 results in the Butler-Volmer equation 2.10 for a one-electron transfer reaction.[53]

$$j = j_0 \left[a_+ \exp\left(\frac{\beta e(E - E^0)}{k_B T}\right) - a_- \exp\left(\frac{-\beta e(E - E^0)}{k_B T}\right)\right] \tag{2.10}$$

The exchange current density is, thus, $j_0 = e\rho k_0 \exp\left(\frac{-\Delta G_a}{k_B T}\right)$. In the electrochemical equilibrium of compensating forward and backward reaction rates ($r_+ = r_-$), the current density equals zero. In this case, the term in the squared brackets in the Butler-Volmer equation 2.10 can be rearranged to the Nernst equation 2.11.[52]

$$E = E_0 - \frac{k_B T}{e} \ln\left(\frac{a_-}{a_+}\right) \tag{2.11}$$

The given derivation holds for elementary reaction steps of electrolyte species on an electrode. To also describe adsorption processes at the catalytically active sites, adsorption isotherms can be derived and need to be considered. They can be incorporated into the reaction rates and are explained in the following.

2.2.2 Adsorption Isotherms

In electrocatalytic processes, forming intermediate species reduces the overall energy barrier. These species are chemically adsorbed at the catalytically active sites. Multiple adsorption isotherms were derived based on different assumptions to quantitatively describe the adsorption and desorption processes. A selection of the formulated isotherms is given in Table 2.1 in equations 2.12 to 2.15. They describe the equilibrium state at equal rates of both desorption and adsorption. In this state, the activity of the adsorbate substance, which can also be expressed in terms of pressure or concentration for gasses or liquids, respectively, is proportional to a term containing the surface coverage θ of the adsorbed species. This term heavily depends on the assumptions during its derivation from the Gibbs adsorption isotherm given in the literature.[54–56] The underlying assumptions and resulting mathematical formulations will be explained in the following paragraphs.

Table 2.1: List of adsorption isotherms, slightly modified taken from Afonso et al. [57].

Name of isotherm	Assumptions	Equation	
Langmuir [58]	localized	$aK = \frac{\theta}{1-\theta}$	(2.12)
Frumkin [56]	localized, lateral interaction	$aK = \frac{\theta}{1-\theta}\exp(-g\theta)$	(2.13)
Volmer [54]	distributed	$aK = \frac{\theta}{1-\theta}\exp\left(\frac{\theta}{1-\theta}\right)$	(2.14)
Hill-de Boer [55, 59, 60]	distributed, lateral interaction	$aK = \frac{\theta}{1-\theta}\exp\left(\frac{\theta}{1-\theta} - g\theta\right)$	(2.15)

- Localized adsorption describes the process of species adsorbing locally at surface sites. Each adsorbed species is assumed to be pinned at a defined site, and lateral motion along the surface is neglected. Following these assumptions, the adsorption rate is only proportional to the activity and the coverage of free sites $(1-\theta)$, and the desorption rate is proportional to the coverage of the adsorbed species. This results in the elegant but usually oversimplified formulation in equation 2.12 found by Langmuir.[58] The derivation holds only for the adsorption of highly dilute gases at extensively oversized surface sites.[55]

- Distributed adsorption considers, in addition to the adsorption process itself, the lateral distribution of the already adsorbed species on the surface. The species usually face minor energetic barriers in moving to a neighboring site and are, thus, expected to spread on the surface.[55] The resulting distribution behavior can be described mathematically by inserting the two-dimensional non-ideal gas equation into the Gibbs adsorption isotherm.[55] The assumption of a two-dimensional gas is reasoned due to the planar adsorption surface. In addition, the species are assumed as non-ideal gas to account for the average free path length of the surface motion. Therefore, an areal correction term is expressed by considering the actual number of adsorbed species and either the areal extent of the species or the areal spacing of the sites.[55] The consequential adsorption isotherm was first derived with this areal correction term by Volmer[54], which resulted in the additional exponential term $\exp(\frac{\theta}{1-\theta})$ in equations 2.14 and 2.15.
- Lateral interactions imply the mutual attraction and repulsive forces between already adsorbed species. Such interactions occur in gases and liquids, known as van der Waals forces.[61] By considering these forces during the derivation of the adsorption isotherm, Frumkin found an additional exponential term $\exp(-g\theta)$ given in equation 2.13.[56] In recent literature, the formulation is also known as the Fowler-Guggenheim[57] or the Temkin[62] isotherm. The unit-less interaction factor g is associated with the free energy of interaction $\Delta G_{\text{int}} = -gk_{\text{B}}T$.[57] Combined with the term of distributed adsorption, the derivation by Hill[59, 60] and de Boer[55] results in equation 2.15. This formulation, also known as van der Waals adsorption isotherm, can be derived by inserting the famous van der Waals equation into the Gibbs adsorption isotherm.[63]

With the resulting isotherms, different adsorption types can be formulated and quantified. Equations 2.12 to 2.15 are employed in the following to set up the model equations to analyze and study the adsorption and desorption processes during the intermediate formation of the OER.

2.3 Experimental Methods

The electrocatalytic processes on the surface can be investigated experimentally using well-established electrochemical methods such as chronoamperometry (CA), CV and EIS. These methods are based on the principle of applying an electric potential to the electrode and measuring the response current resulting from transferred and accumulated electrons. By applying different time-dependent functions of the potential, relevant effects can be isolated and quantified. An overview of the characteristics and main outcomes of the methods are explained in the following paragraphs.

- CA is an experimental method in which the applied potential is kept constant in time and the resulting current is measured. The value of the potential is set to a point of interest, i. e. for the OER to a value at which the reaction is driven. As the measurement time progresses, the processes at the electrode and in the experimental setup tend to reach a steady state and the current converges. In this state, the limiting process determines the turnover and the current is a proportional measure of the turnover rate. By plotting the steady-state currents at different logarithmically scaled values of the potential, a Tafel plot is created, which is a commonly used illustration of the catalyst activity. In addition, the CA method is used to degrade the catalyst under defined operating conditions.
- CV describes an experiment in which the potential applied to the electrode is repeatedly changed linearly in time between two values. This enables to detect the current response of different processes such as redox reactions, adsorption and desorption of species, as well as charging the double layer. In addition, the limiting transport of reactant and product species can be measured by using a rotating electrode setup that allows to manipulate the Nernst diffusion layer. This method provides valuable insights into the rate of several processes and also indicates the potentials at which the processes take place. Due to their high informative value, the results obtained with CV measurements are used to parameterize the kinetic models presented in this dissertation.
- EIS is an experimental method in which the electrochemical response current of a sinusoidally changing potential with different frequencies is detected. The highly dynamic change is used to identify the response frequency of electrochemical processes and to quantify measures such as the capacitance and resistance, which are related to charging and transport processes, respectively.

In the work of this dissertation, the measurements were carried out in a three electrode setup with a rotating disc working electrode, a counter electrode and a reference electrode in a liquid electrolyte. A detailed description of the procedure, the used materials and the relevant parameters is given in the respective sections 3.2, 4.2 and 5.2.

2.4 Microkinetic Model Developement

In this section, a comprehensive mathematical model of the reaction kinetics is derived and presented. The developed physicochemical model will fulfill all the requirements in section 1.2, allowing for a comprehensive and dynamic simulation of an electrocatalytic reaction system. Therefore, the set of equations is derived from the fundamental description of the surface processes already presented in the section above. In contrast to standard kinetic models, which rely on steady-state or quasi-equilibrium assumptions, each reaction rate and the surface coverage of

each adsorbed intermediate species can be simulated individually and time-dependent. Furthermore, the details of the implementation into the MATLAB environment are described.

2.4.1 Model Equations and Parameters

A microkinetic model of multiple species j and possibly multiple reactions i requires both quantities to be predefined. The set of species $j \in \{\Omega_{\text{sur}};\ \text{e}^{-};\ \Omega_{\text{el}}\}$ contains the species on the electrode surface Ω_{sur}, the electrons e^{-}, and the species in the electrolyte phase Ω_{el}. The set of reactions $i \in \{1 \ldots N\}$ is defined by the total number of reactions N.
The **stoichiometric coefficient matrix** ν is defined by the respective matrices in forward ν_{+} and backward ν_{-} directions in equation 2.16. The entries in one row of the matrix specify the number of the individual reactant or produced species of the corresponding single reaction.

$$\nu = \nu_{+} - \nu_{-} = (\nu_{ij})_{\ i\,=\,1,\,\ldots,\,N;\ j\,=\,\Omega_{\text{sur}},\,\text{e}^{-},\,\Omega_{\text{el}}} \tag{2.16}$$

The **rate equations** in forward and backward directions are derived by inserting the term for the rate constant from equation 2.6 into equation 2.8.

$$r_{\pm} = a_{\pm} \cdot k_0 \cdot \exp\left(\frac{-\Delta G_{\text{a}} \mp \beta \Delta G_{\text{r}}^{0} \pm \beta e E}{k_{\text{B}} T}\right) \tag{2.17}$$

The activation free energy $\Delta G_{\text{a},i}$ and the reaction free energy $\Delta G_{\text{r},i}$ are defined for the reaction rates $r_{\pm i}$ of a specific reaction i. To consider the influence of different species, the product of the activities of all participating electrolyte species $a_j^{\nu_{\pm ij}}$ and the surface coverage of all participating species on the electrode $\theta_j^{\nu_{\pm ij}}$ is replacing the activity. Further, the absolute number of transferred electrons per reaction step $|\nu_{i\text{e}^{-}}|$ is inserted before the elementary charge to account for the difference between electrochemical and chemical reactions. The modified rate equation for multiple species and a set of multiple reactions is written in equation 2.18.

$$r_{\pm i} = \prod_j \left(a_j^{\nu_{\pm ij}} \cdot \theta_j^{\nu_{\pm ij}}\right) \cdot f_{\pm i}(\theta) \cdot k_0 \cdot \exp\left(\frac{-\Delta G_{\text{a},i} \mp \beta \Delta G_{\text{r},i} \pm \beta |\nu_{i\text{e}^{-}}| eE}{k_{\text{B}} T}\right) \tag{2.18}$$

The **adsorption function** $f_{\pm i}(\theta)$ can be derived from the adsorption isotherms given in section 2.2. This will be done in the following by using the Hill-de Boer isotherm formulation in equation 2.15 and adapting it for a reversible desorption step ${}^{*}\text{A} \rightleftharpoons {}^{*}\text{B} + \text{C}$, which includes two adsorbed species: reactant A and product B and a non-adsorbed product species C. Therefore, the coverage of the adsorbed species θ is identified with the reactant species θ_A or the notation $\prod \theta_j^{\nu_{+ij}}$ introduced above. As the coverage of the remaining sites $(1-\theta)$ does not necessarily match the coverage of the available sites for the adsorption process, the expression $(1-\theta)$ is

instead correctly written as the coverage of the product species θ_B or in the generalized notation as $\prod \theta_j^{\nu_{-ij}}$. Following the assumption that not only species A but also species B are distributed and interact laterally, a corresponding exponential term $\exp\left(\frac{\theta_B}{\theta_A} - g_B\theta_B\right)$ is introduced in the denominator. With all these adaptations, the isotherm can be written in equation 2.19.

$$K = \frac{\theta_A}{a_C \cdot \theta_B} \cdot \frac{\exp\left(\frac{\theta_A}{\theta_B} - g_A\theta_A\right)}{\exp\left(\frac{\theta_B}{\theta_A} - g_B\theta_B\right)} \tag{2.19}$$

Now one can adjust this isotherm, which is only valid for a single reaction, to the generalized notation of multiple reactions i and multiple species j. In addition, the unit-less interaction factor g_j is rewritten with the term given in section 2.2, which includes the interaction free energy of the adsorbed species $\frac{-\Delta G_{\text{int},j}}{k_B T}$. This results in the following notation:

$$K_i = \frac{\prod_j \left(a_j^{\nu_{+ij}} \cdot \theta_j^{\nu_{+ij}}\right)}{\prod_j \left(a_j^{\nu_{-ij}} \cdot \theta_j^{\nu_{-ij}}\right)} \cdot \frac{\exp\left(\prod_j \frac{\theta_j^{\nu_{+ij}}}{\theta_j^{\nu_{-ij}}} + \prod_j \left(\frac{\Delta G_{\text{int},j}}{k_B T}\theta_j\right)^{\nu_{+ij}}\right)}{\exp\left(\prod_j \frac{\theta_j^{\nu_{-ij}}}{\theta_j^{\nu_{+ij}}} + \prod_j \left(\frac{\Delta G_{\text{int},j}}{k_B T}\theta_j\right)^{\nu_{-ij}}\right)} \tag{2.20}$$

The first fraction of equation 2.20 is already included in the reaction rate in equation 2.18. For direct insertion of the remaining term in equation 2.18, it is rearranged algebraically to the adsorption function $f_{\pm i}(\theta)$, $\forall j \in \Omega_{\text{sur}}$, $\forall i$ given in equation 2.21.

$$f_{\pm i}(\theta) = \exp\left(\beta\left[\prod_j \left(\frac{\Delta G_{\text{int},j}}{k_B T}\theta_j\right)^{\nu_{\pm ij}} - \prod_j \left(\frac{\Delta G_{\text{int},j}}{k_B T}\theta_j\right)^{\nu_{\mp ij}} + \prod_j \frac{\theta_j^{\nu_{\pm ij}}}{\theta_j^{\nu_{\mp ij}}} - \prod_j \frac{\theta_j^{\nu_{\mp ij}}}{\theta_j^{\nu_{\pm ij}}}\right]\right) \tag{2.21}$$

The **species balance** in equation 2.22 allows dynamic solving of the set of rate equations. The sum of all surface coverages is set to unity $\sum \theta_j = 1$ as a boundary condition.

$$\frac{\mathrm{d}\theta_j}{\mathrm{d}t} = \sum_i \nu_{ij}\left(r_{-i} - r_{+i}\right) \tag{2.22}$$

The **charge balance** in equation 2.23 is implemented to ensure the conservation of charge q. It contains the double-layer capacitance C_{dl} as well as all sinks and sources in charge due to the electrochemical reactions and electrical conductors.

$$\frac{\mathrm{d}q}{\mathrm{d}t} = C_{\text{dl}} \cdot \frac{\mathrm{d}E}{\mathrm{d}t} = j(t) - F\rho\sum_i \nu_{ie^-}\left(r_{+i} - r_{-i}\right) \tag{2.23}$$

The **model input** is given with an applied starting potential E_0 and the change in potential with time $\frac{dE}{dt}$, defined as constant in absolute values, set to zero, or assumed as a sinusoidal signal in time to simulate CV, CA, or EIS experiments, respectively. Overall it results in a time-dependent function of the potential $E(t)$, as given in equation 2.24. The potential drop in the electrolyte is accounted for by the electrode area A and the ohmic resistance R.

$$E(t) = E_0 + t\frac{dE}{dt} - j(t)AR \tag{2.24}$$

Multiple variables can serve as the **model output** depending on the point of interest in a particular study. In the following model analysis and the studies of this work, the current density, the surface coverage, and the reaction rates are of significant interest. All three quantities are simulated dynamically with the presented model approach.
In addition to the presented model equations, a set of valid **parameter** values is required to gain proper simulation results. Some parameters can be derived from the assumed mechanism (ν) or gained directly from the experimental setup (R, A, a, T). Other parameters are not directly accessible with common experimental methods (ΔG_a, ΔG_r, ΔG_{int}, ρ, C_{dl}). For a model analysis, these parameters can be varied independently. However, quantification by a model-based parameter identification algorithm, such as a global random search or a pattern search, becomes necessary to reproduce the dynamic behavior of an experimental system.

2.4.2 Implementation

The model equations and the parameter identification algorithms are implemented in the MATLAB environment. The set of ordinary differential equations was solved by using the ode23s algorithm. High accuracy of the results is ensured by setting the absolute error tolerance to 10^{-12} and the maximum step size to 0.01 s. The model code of a single proton-coupled electron transfer (PCET) step with two adsorbed species (${}^*\mathrm{AH} \rightleftharpoons {}^*\mathrm{A} + \mathrm{H}^+ + \mathrm{e}^-$) is given in appendix A.1. This implementation constitutes a comprehensive description of the microkinetics of an electrocatalytic reaction as required. It is designed to allow for the dynamic modeling of a reaction system, which is crucial for answering the scientific questions of this work and conducting the model analysis in the next section.

2.5 Model Analysis

In this section, the derived model is analyzed to understand the dynamic response with the assumption of different parameter values and adsorption isotherms. To intuitively comprehend the complex model approach, a careful analysis of isolated effects is helpful. Therefore, this section

gives a systematic analysis of key parameters and their impact on the model output of a single PCET ($^{*}\mathrm{AH} \rightleftharpoons {}^{*}\mathrm{A} + \mathrm{H}^{+} + \mathrm{e}^{-}$). The stoichiometric coefficients of the forward and backward reactions are defined in equation 2.25.

$$\begin{aligned} & & \overbrace{\qquad\qquad}^{j \in \Omega = \{\mathrm{H}^{+};\ \mathrm{e}^{-};\ {}^{*}\mathrm{AH};\ {}^{*}\mathrm{A}\}} \\ \boldsymbol{\nu}_{+} = & & \begin{pmatrix} 0 & 0 & 1 & 0 \end{pmatrix} \\ \boldsymbol{\nu}_{-} = & & \begin{pmatrix} 1 & 1 & 0 & 1 \end{pmatrix} \end{aligned} \tag{2.25}$$

Further, the effect of using different adsorption isotherms is compared and discussed. Overall, this analysis is conducted to ensure that the model implementation allows the reproduction of the characteristics of experimental CV curves, an essential requirement for the scientific work in the following chapters.

2.5.1 Parameter Variations

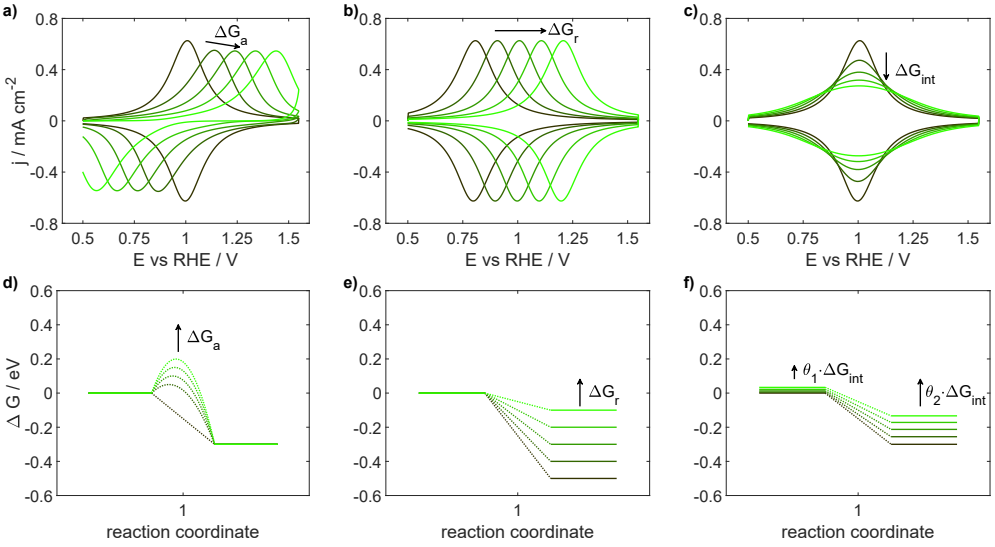

Figure 2.4: a-c) Simulated dynamic behavior of an elementary deprotonation step and d-f) respective energy diagrams at E = 1.3 V vs RHE with the variation of the activation free energy in a) and d), of the reaction free energy in b) and e) and of the interaction free energy in c) and f). Arrow directions indicate an increase in denoted values. The parameters are given in Table 2.2.

Figure 2.4 shows the effect of the variation of different energy parameters with values given in Table 2.2. Only one parameter is varied for the simulations in each diagram. In Figure 2.4a, the

Table 2.2: Values of the model parameter variation study with a single proton-coupled electron transfer in Figure 2.4. Bold numbers indicate the values held constant during the variation of the other parameters. Further parameters such as the symmetry factor, the double-layer capacitance, and the density of active sites are set to the respective bold values in Table 2.3.

variation	ΔG_a / eV	ΔG_r^0 / eV	ΔG_{int} / eV
1	**0.00**	0.8	**0.00**
2	0.20	0.9	0.05
3	0.35	**1.0**	0.10
4	0.30	1.1	0.15
5	0.35	1.2	0.20

simulated current density indicates an increasing difference in the anodic and cathodic absolute peak maxima with increasing values of the activation free energy. The energy diagram in Figure 2.4d shows the increase in the kinetic energy barrier associated with the activation free energy, which causes the peak-to-peak shift in the CV. The simulations with incrementally ascending reaction free energy parameter values are given in Figure 2.4b and describe an overall shift of the redox transition to higher potentials. In the corresponding energy diagram in Figure 2.4e, a higher energy state of the product species is observable with an increasing value of the reaction free energy. This behavior explains the higher electric potential required to trigger the reaction. In Figure 2.4c, the simulations with simultaneous variations of the interaction free energy of both reactant and product species result in a flattened peak shape accompanied by increasing parameter values. As the impact of the interaction energy is linked to the coverage of the individual adsorbed species, a slight but unequal shift in the energy states of both species is observable in

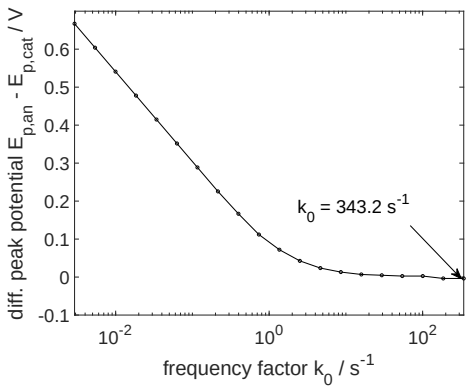

Figure 2.5: The simulated peak-to-peak position of a one-electron transfer reaction depends on the pre-exponential frequency factor k_0 with the activation free energy value set to 0 eV.

the energy diagram in Figure 2.4f. The dissimilarity arises due to the higher amount of the product species present, as most of the electrons are already transferred at the given potential of 1.3 V. Though, for identical values of both interaction energies, the energy states of the two species are affected equally, which results in a symmetric peak shape in the CV curves.
When assuming no activation barrier, the peak-to-peak potential of anodic and cathodic redox transition converges to 0 V at a pre-exponential frequency factor of roughly k_0 = 343.2 s^{-1}, as shown in Figure 2.5. This value was chosen because one can identify the activation free energy from the peak-to-peak potential. In consequence, the lower limit of the activation free energy is defined as ΔG_a = 0 eV.

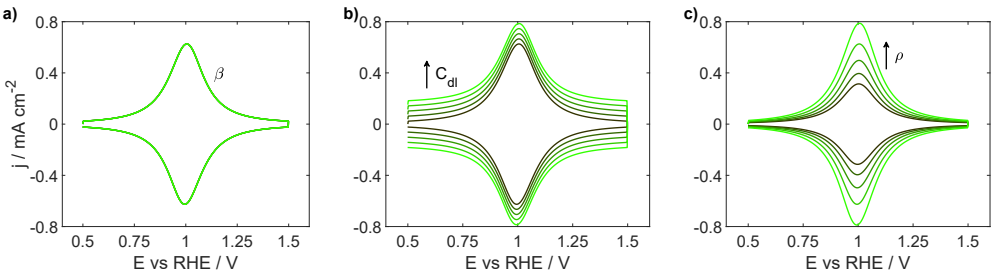

Figure 2.6: Simulated dynamic behavior of an elementary deprotonation step with the variation of a) the symmetry factor, b) the double-layer capacitance, and c) the density of active sites. Arrow directions indicate an increase in denoted values. The parameters are given in Table 2.3.

The model behaviors with the variations of the symmetry factor, the double-layer capacitance, and the density of active sites are presented in Figure 2.6, and the respective values are given in Table 2.3. A variation of the symmetry factor shows no effect in the simulated CV curve in Figure 2.6a. In consequence, an asymmetric barrier does not affect the effective reaction rate. This finding justifies the assumption of a symmetry factor $\beta = (1-\beta) = 0.5$ in the model equations.

Table 2.3: Values of the model parameter variation study with a single proton-coupled electron transfer in Figure 2.6. Bold numbers indicate the values held constant during the variation of the other parameters. The energy parameters are set to the respective bold values in Table 2.2.

variation	β / -	C_{dl} / F m^{-2}	ρ / mol m^{-2}
1	0.3	$\approx$ **0**	$10^{-4.3}$
2	0.4	2.0	$10^{-4.2}$
3	**0.5**	4.0	$10^{-4.1}$
4	0.6	6.0	$\mathbf{10^{-4.0}}$
5	0.7	8.0	$10^{-3.9}$

However, in Figure 2.6b, a higher double-layer capacitance causes an increase in the absolute current density, which is constant over the whole potential range. Even though the overall charge changes, the number of transferred electrons by the reaction remains the same. In contrast to this observation, the density of active sites is correlated with the number of electrons involved in the reaction. This results in a significantly higher current density of the simulated redox transitions with an increasing density of active sites in Figure 2.3c.
In conclusion, the conducted analysis demonstrates that the model description allows for a dynamic simulation of a PCET step. Except for the symmetry factor, all of the varied parameters affect the model output in a particular and well-distinguishable way. Thus, the model provides an essential basis for estimating the parameter values of more complex mechanisms later. However, besides the differently assumed parameter values, the simulation of multiple adsorption isotherms is possible, which will be analyzed in the following subsection.

2.5.2 Comparison of the Adsorption Isotherms

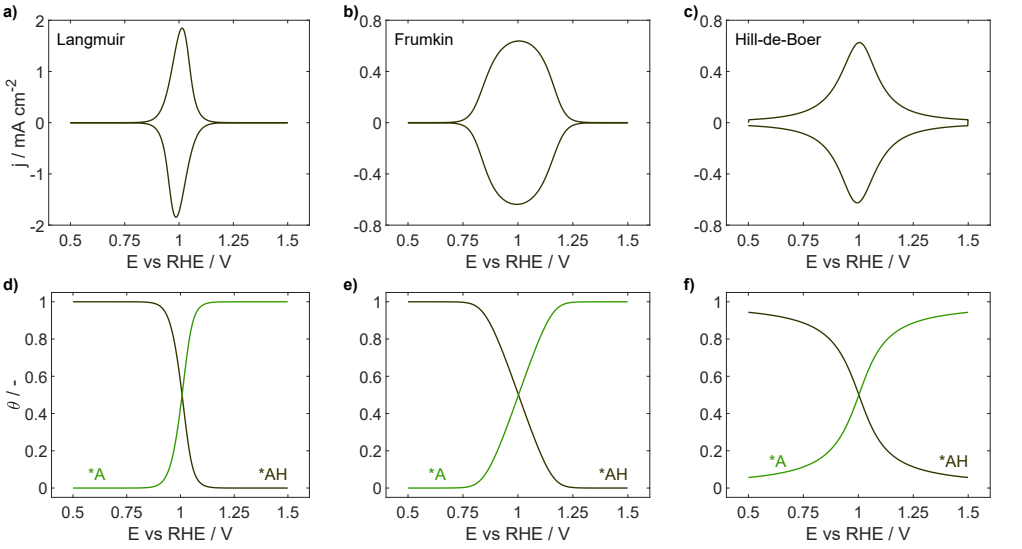

Figure 2.7: Simulated dynamic behavior of an elementary deprotonation step with the assumption of different adsorption isotherms derived a) by Langmuir, b) by Frumkin, and c) by Hill-de Boer. For the simulation shown in b), the interaction energy is assumed to be a value of 0.1 eV for the reactant and produced species. The surface coverages of the adsorbed species are shown in d), e), and f), respectively.

To elaborate on the effect of different adsorption isotherms, simulations with the most common ones are conducted, published by Langmuir, Frumkin, and Hill and de Boer. The respective mathematical descriptions are derived from the literature and are given in Table 2.1. Similarly

to the derivation of the Hill-de Boer adsorption function in section 2.4, the adsorption functions of all three isotherms are formulated. Based on the Langmuir isotherm, the derived adsorption function in equation 2.26 is simply unity.

$$f_{\pm i,\text{Langmuir}}(\theta) = 1 \tag{2.26}$$

The respective formula derived from the Frumkin isotherm is given in equation 2.27.

$$f_{\pm i,\text{Frumkin}}(\theta) = \exp\left(\beta\left[\prod_j\left(\frac{\Delta G_{\text{int},j}}{k_\text{B}T}\theta_j\right)^{\nu_{\pm ij}} - \prod_j\left(\frac{\Delta G_{\text{int},j}}{k_\text{B}T}\theta_j\right)^{\nu_{\mp ij}}\right]\right) \tag{2.27}$$

CV simulations of a single PCET step are conducted to analyze their effect on the model output. The resulting current density is shown in Figure 2.7. Firstly, it can be noted that the number of electrons transferred and, thus, the overall charge remains identical for all simulations. However, there are significant differences in the kinetics. The Langmuir desorption type is shown in Figure 2.7a and starts at a comparably high potential of 0.85 V but the current increases rapidly to a maximum of about 1.8 mA cm^{-2}. The fast reaction rate comes with a rapid increase in the corresponding surface coverage of the product species once the reaction is started, as given in Figure 2.7d. For comparison and given in Figure 2.7b, the Frumkin desorption type starts at a lower potential of 0.75 V, and the current density reaches an overall maximum of just about 0.6 mA cm^{-2}. As the lower current density indicates slower kinetics also the coverage of the product surface species is increasing with a smaller gradient along the potential in Figure 2.7e. The simulation of the Hill-de Boer type of desorption is shown in Figure 2.7c and shows the broadest redox transition feature. Here, the reaction already takes place at the starting potential of 0.5 V, and the slope of the current density increases monotonously until the maximum of about 0.6 mA cm^{-2}. Consequently, the amount of produced surface species in Figure 2.7f is not linearly correlated to the applied potential.

In conclusion, the simulations of the three adsorption functions show significant disparities. With the dynamic modeling approach and the model output of a CV-adapted input signal, one can discriminate between the fundamental isotherms. The model-based analysis allows one to validate or falsify any isotherm assumption with experimental data. Additionally, considering the results of the parameter variation analysis, one can conclude that the approach is viable for modeling catalytic surface processes and dynamically simulating the microkinetics for various parameter values and adsorption types.

2.6 Concluding Remarks

Based on the principles of electrocatalysis and the fundamental descriptions of surface processes, a model for a comprehensive microkinetic simulation of intermediate adsorption on the catalyst active sites is presented. In contrast to recent scientific work on the kinetic modeling of the OER, no simplifying approximations based on quasi-equilibrium or steady-state assumptions are applied. Instead, the set of model equations is derived to allow for time-continuous, thus, dynamic simulation, e.g., of a cyclic potential input. Such CV simulations are performed during the model analysis and identified as an adequate data set for parameterization since significant parameter variations provide unique output signals. In addition, the CV simulations can be used to distinguish adsorption types, represented by isotherms of localized, distributed, and lateral interacting adsorption. Consequently, validation of model assumptions and parameter values is possible through widely applied CV experiments, which means that the energy parameters do not rely on *ab initio* calculations. This liberation from defined material structures also allows processes on non-ideal and degraded electrocatalysts to be evaluated and quantified. The derived and analyzed modeling approach satisfies the requirements specified in section 1.2 and can serve as a fundamental component of the methodology for elucidating the complex processes on relevant OER catalysts. Its application is covered in the following chapters of this dissertation.

3 Identification of the OER Mechanism on hydrous Iridium[3]

3.1 Introduction

In an acidic environment, anodically grown hydrous iridium is revealed as highly active and has been widely studied concerning its electrochemical characteristics.[64–66] The stability during the OER seems promising: hydrous Ir[14] but also metallic Ir[40] and the oxide IrO_2[12] exhibit lower dissolution rates compared to their highly active competitors based on Ru[12]. In direct comparison, metallic Ir is more active but less stable than IrO_2. Hydrous Ir is even more active since sites in the near-surface structure also catalyze the OER.[67] Knowledge of the microkinetics of a reaction allows for identifying slow and fast steps and deducing possible improvements. For studying the microkinetics, a valid mechanism assumption based on a good understanding of the surface changes is needed. The present understanding of processes during the OER is briefly summarized in the following paragraph.

During the OER, electrocatalytically active catalysts are known to form adsorbed hydroxide and oxygen at its catalyst-electrolyte interface.[46] The appearance of faradaic currents at anodic potentials before the onset of the OER is either attributed to the adsorption of additional hydroxy groups[68–71] on the hydrous iridium surface or to deprotonation steps[72–74]. X-ray emission spectroscopy allowed the detection of increasing overall oxygen content in the hydrous Ir material, and the electron diffraction pattern suggests the formation of pseudo-rutile IrO_2.[75] This finding matches with *in situ* X-ray absorption spectroscopy (XAS) measurements since, in acid media, it is concluded that the intermediate state at approximately 1.05 V vs RHE fits the Ir–O distance of crystalline IrO_2.[76] According to *in situ* X-ray photoelectron spectroscopy (XPS) analysis of different binding energies of the O 1s level, there is a decreasing hydroxy and an increasing oxide content with increasing potential in the range of approximately 0 up to 1.5 V vs RHE.[74] In the near-surface region, the observation of adsorbed hydroxide and oxygen is additionally confirmed using atom probe tomography and could furthermore be correlated to a

[3] Parts of this chapter have been published in the following article:
[3] **Geppert, J.**; Kubannek, F.; Röse, P.; Krewer, U. *Electrochim. Acta* **2021**, *380*, 137902-137914.

metastable state with an IrO and OH ratio of roughly 1.[67]
XPS analysis reveals the co-existence of +III and +IV oxidation states.[77–79] The picture of the surface transformation process is complemented by XAS analysis, which allows differentiating three main potential regions: (i) between 0.2 and 0.7 V vs RHE, multiple studies agree on an oxidation state of +III.[78, 80, 81] (ii) The potential range ongoing from 0.7 up to approximately 1.1 V vs RHE shows mainly Ir(IV).[81, 82] (iii) At potentials higher than 1.1 V vs RHE, an increasing oxidation state up to +V and even higher can be obtained.[80, 81] During the OER, different oxidation states, namely +III, + IV, and +V, were detected.[81, 83]
To complement these experimental findings, modeling methods are used to extend the analysis by identifying the mechanism, quantifying its kinetics, and proving thermodynamic consistency. Energetically favorable intermediate states on metals[16] and oxides[17, 44] are extensively postulated using calculations based on DFT. The vaguely defined structure of the hydrous material surface complicates the DFT calculations of the material itself and, in consequence, also of adsorbed or intermediate species. In order to address this issue, the binding energies of the intermediate species during different mechanisms at various modified Ir surfaces are compared.[84] According to this work, the reaction pathway is heavily influenced by the near-surface material structure. However, to correlate these theoretical mechanistic results to the experimental insights of the hydrous Ir material, model-based kinetic analysis is needed.
As previously stated, the quasi-equilibrium and steady-state assumptions lead to problems in microkinetic analysis. A more complex and fully dynamic analysis is advisable. Such models allow for simulating and quantitatively analyzing the experimentally frequently used dynamic measurements. Modeling without quasi-equilibrium and steady-state assumptions is crucial to perform simulations with dynamic input values with no further restraints. A first study of such kind is presented for OER at hydrous iridium in this chapter. Carefully conducted CV experiments, the deduction of the two most likely reaction mechanisms from literature, and a model-based study on the microkinetics are presented. This includes changes in surface coverage with multiple adsorbed species and the formation of a reduced species at highly oxidative potentials. The results resolve how the potential affects the reaction rates and changes the rate-limiting steps. Further, the thermodynamic properties are derived from the model, which enables bridging the gap between experiments and *ab initio* calculations such as DFT and molecular dynamics based simulations.

3.2 Methods

3.2.1 Experimental Setup

All electrochemical experiments were carried out in a polytetrafluoroethylene (PTFE) cell combined with a rotating disc electrode (RDE) setup from PINE Research Instrumenation Inc., connected to a Gamry Reference 600+ potentiostat. Deionized water (Merck MilliQ, 18.2 MΩ cm) was used as a solvent and for extensively rinsing the cell prior to the measurements. Sulfuric acid ROTIPURAN® Supra 95 % from Carl Roth GmbH + Co. KG was purchased to produce the 0.1 M H_2SO_4 electrolyte solution. The working electrode consisted of a polycrystalline iridium cylinder produced and pre-polished by Mateck GmbH and embedded planar into a polyether ether ketone (PEEK) electrode holder. A PTFE shroud assures sealing and a back-sided gold pin electrical conductivity with the RDE rotator shaft. The experiments were performed as follows: prior to the measurement, the available circular electrode area $A = 0.1963$ cm^2 was polished with 0.05 µm aluminium containing polish media to remove a remaining hydrous film. The cell was filled with 200 ml electrolyte solution and purged with Argon ($\geq$ 99.996 %) for 10 min before and during the complete experiments. A platinum wire counter and HydroFlex reversible hydrogen reference electrode from Gaskatel mbH were inserted directly into the cell. The hydrous iridium film was produced by cycling the polycrystalline iridium electrode 100 times in the potential scan range from $E = 0.05$ to 1.55 V vs RHE with a potential rate of $\mathrm{d}E/\mathrm{d}t = 500$ mV s^{-1}. This method is widely used in multiple studies.[73, 85, 86] Once the film has been established, potential-driven EIS was performed at open circuit potential with frequencies ranging from $f = 10^5$ to 10^{-1} Hz with an amplitude of $\hat{E} = 10$ mV. Subsequently, three consecutive CV curves were measured with potential rates $\mathrm{d}E/\mathrm{d}t = \{500, 200, 100, 50, 20, 10\}$ mV s^{-1} in between potentials of $E = 0.3$ and 1.6 V vs RHE. All potentials are given versus RHE if not otherwise stated.

3.2.2 Mechanistic Assumptions

In order to establish a microkinetic model for the OER at hydrous iridium, the assumption of at least one mechanism is required. Figure 3.1 provides an overview of literature-proposed mechanisms, including the respective pathways and oxidation states. While Figures 3.1a to 3.1c are formulated based on experimental findings on hydrous iridium[12, 74, 81, 87, 88], the mechanism in Figure 3.1d is widely used in DFT calculations of the OER on metal and oxide catalysts, e.g., on rutile IrO_2[17, 44, 84].
Since the output of a microkinetic model depends strongly on the assumed mechanism, careful validation of the reaction mechanisms provides the basis to set up the model successfully. Therefore, an evaluation is done by comparing the mechanisms with four major experimental findings.

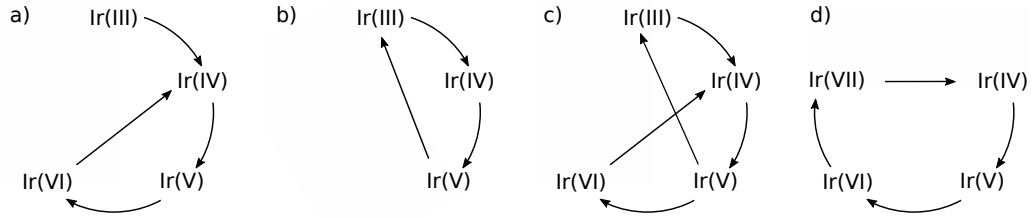

Figure 3.1: Mechanisms proposed for surface oxidation reaction steps and OER for hydrous Ir by a) Kötz et al.[74], b) Cherevko et al.[12], Minguzzi et al.[81] and Steegstra et al.[87], c) Kasian et al.[88], and d) for rutile IrO_2 by Rossmeisl et al.[17] and Klyukin et al.[84]

(i) CV results from the literature[12, 70, 74, 75] and own experiments (see section 3.3.1) exhibit at least two distinct electron transfer reactions in addition to the exponential onset of the OER. This requires a minimum of three distinguishable electrochemical reactions to be present in the overall mechanism. (ii) *In situ* XPS and XAS studies[74, 80, 81] imply oxidation states ranging from +III up to at least +VI. Additionally, XAS findings[81] state the occurrence of a reduced oxidation state +III even at high potentials of approximately 1.6 V. (iii) XPS measurements[74, 83] reveal an increasing amount of covalent oxygen bindings with increasing potential. Iridium hydroxide bonds are present at several potentials and even in the OER region. (iv) Atom probe tomography detected the material composition to contain IrO and OH with a ratio of roughly 1:1.[67] According to these results, the hydrous Ir consists of the species IrO(OH) initially.

In the following, reaction mechanisms are formulated that take the various theories and findings into consideration. As the experimental and DFT-derived mechanisms deviate significantly, it is useful to evaluate and compare both concepts. Firstly, a reaction mechanism is set up inspired by the DFT studies on rutile IrO_2 that takes into account the findings (i) to (iv). All reactions are adapted accordingly, but instead of Ir(IV) $\equiv$ IrO_2, the initial species is defined as Ir(III) $\equiv$ IrO(OH), the hydrous Ir in Figure 3.2a. Species with oxidation states of +III are oxidized stepwise up to +VII or +V and reduced back to +III, while oxygen is released as a single site or a dual site step. Herewith, one is able to formulate a first mechanism (M1) which can be described by eight reaction steps in equations 3.1 to 3.8 and is closely related to the mechanism widely used in DFT calculations for several oxides in Figure 3.1d.

Additionally, to respect the studies that experimentally derived the OER mechanisms in Figures 3.1a to 3.1c, a second mechanism was taken into account for the kinetic modeling. The mechanism in Figure 3.1a contradicts finding (iii) since the reduced +III oxidation state is not present in the OER circle. Mechanism Figure 3.1b contains only two electrochemical steps and, therefore, might be able to describe the OER but not the potential range prior to the OER completely. In principle, the mechanism in Figure 3.1c is a combination of the two previous ones and, thus, is in line with all major experimental findings. Therefore, the mechanism is written down by Kasian et al.[67] is chosen as the second evaluated mechanism (M2). It is displayed in Figure 3.2b and

can be described by six reactions in equations 3.9 to 3.14.
Since H_2O adsorption on oxides was found to be energetically favorable,[44, 45] it is implemented as an individual chemical step, decoupled from further electrocatalytic PCET. Both mechanisms, M1 and M2, are visualized in 3.2, starting with the initial hydrous iridium species Ir(III) ≡ IrO(OH) found by atom probe tomography. They provide a sound basis for formulating the kinetic models presented in the following.

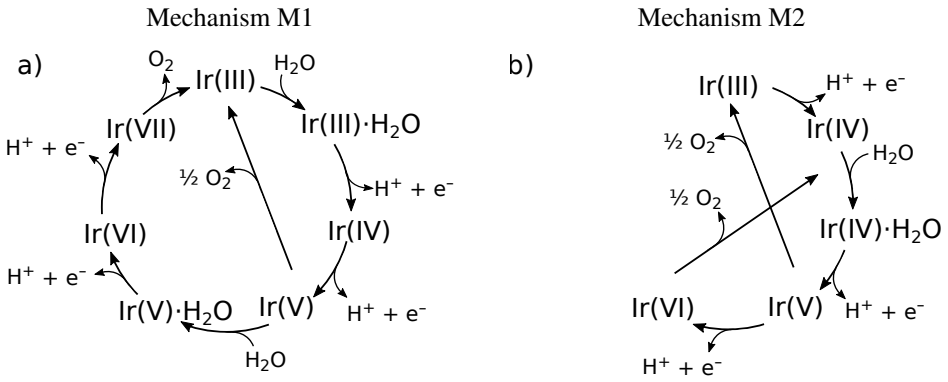

Figure 3.2: a) Visualization of the reaction mechanism M1 based on assumptions published for DFT calculations on several oxides. b) Scheme of mechanism M2, derived by Kasian et al.[88], based on experimental results of hydrous iridium.

Mechanisms M1 and M2 are converted into a form consisting of active catalyst sites, denoted with *, on which single surface species can adsorb, desorb and react. This enables microkinetic modeling and balancing of the species.

Mechanism M1
$^* \equiv \mathrm{IrO(OH)} \equiv \mathrm{Ir(III)}$

$$^* + H_2O \overset{r_1}{\rightleftharpoons} {}^*H_2O \tag{3.1}$$
$$^*H_2O \overset{r_2}{\rightleftharpoons} {}^*OH + H^+ + e^- \tag{3.2}$$
$$^*OH \overset{r_3}{\rightleftharpoons} {}^*O + H^+ + e^- \tag{3.3}$$
$$^*O + H_2O \overset{r_4}{\rightleftharpoons} {}^*OH_2O \tag{3.4}$$
$$^*OH_2O \overset{r_5}{\rightleftharpoons} {}^*OOH + H^+ + e^- \tag{3.5}$$
$$^*OOH \overset{r_6}{\rightleftharpoons} {}^*OO + H^+ + e^- \tag{3.6}$$
$$2\,{}^*O \overset{r_7}{\rightarrow} 2\,{}^* + O_2 \tag{3.7}$$
$$^*OO \overset{r_8}{\rightarrow} {}^* + O_2 \tag{3.8}$$

Mechanism M2
$^* \equiv \mathrm{IrO(O)} \equiv \mathrm{Ir(IV)}$

$$^*H \overset{r_1}{\rightleftharpoons} {}^* + H^+ + e^- \tag{3.9}$$
$$^* + H_2O \overset{r_2}{\rightleftharpoons} {}^*H_2O \tag{3.10}$$
$$^*H_2O \overset{r_3}{\rightleftharpoons} {}^*OH + H^+ + e^- \tag{3.11}$$
$$^*OH \overset{r_4}{\rightleftharpoons} {}^*O + H^+ + e^- \tag{3.12}$$
$$2\,{}^*O \overset{r_5}{\rightarrow} 2\,{}^* + O_2 \tag{3.13}$$
$$2\,{}^*OH \overset{r_6}{\rightarrow} 2\,{}^*H + O_2 \tag{3.14}$$

3.2.3 Microkinetic Model Equations

The reaction kinetics modeling of mechanisms M1 and M2 is methodically inspired by previous studies [28, 32, 89, 90] and based on the rate equation 2.18 for chemically and electrochemically driven reactions. The derivation of the equation is given in section 2.4, and the rate equations for the single reaction steps are written out in [3].
Forward r_{+i} and backward r_{-i} rates are calculated separately, by using parameters for the reaction rate constants k_{+i} and k_{-i} given in equation 2.6 instead of free energy parameters. The activities a_j of the electrolyte species $j \in \Omega_{\mathrm{el}} = \{H^+, H_2O, O_2\}$, surface coverages θ_j for the species $j \in \Omega_{\mathrm{sur}}$ $\{^*, {}^*H, {}^*H_2O, {}^*OH, {}^*O, {}^*OH_2O, {}^*OOH, {}^*OO\}$ and further parameters as explained in chapter 2 are employed for the simulations. Adsorption functions f_+ and f_- account for non-idealities of adsorption processes that affect the kinetics. The electrode coverage θ_j of surface-bound intermediates j is taken into account, and since for hydrous iridium, the broadened peak behavior[87] implies surface coverage dependent adsorption energies with species interaction, a van der Waals adsorption isotherm is assumed[55, 91, 92]. This considers an areal spacing of surface sites and the interaction of adsorbed species[55]. For an in-depth discussion, see section 3.3.2. The adaptation of this adsorption behavior into the reaction equations, which was done in an analogous manner for Frumkin/Temkin adsorption,[93, 94] results in the functions $f_\pm$ given in equation 2.21. For parameterization, the unit-less interaction factor $g = -\frac{\Delta G_{\mathrm{int}}}{k_B T}$ was used as a relative measure of the interaction free energy.

The dynamic behavior during a CV is arising by the single potential dependent de- and adsorption processes, which trigger the change in surface coverage $\theta_j \in [0, 1]$ of the intermediate species over time t. In order to account for this, the equation 2.22 for the species balance, equation 2.23 for the dynamic charge balance and equation 2.24 for the dynamically applied potential are used. The formal mean oxidation state OS_m is calculated by summing up the coverage weighted oxidation states of all assumed species j:

$$OS_m = \sum_j (\theta_j \cdot OS_j), \ \forall j \in \Omega_{sur} \tag{3.15}$$

3.2.4 Simulation and Model Parameter Identification

The electrochemical model equations were implemented in MATLAB, and the respective set of ordinary differential equations was solved using the ode23s algorithm with a given set of kinetic parameters over time. Simulations were performed by applying a constant input potential rate within the same voltage range as in the experiment.
Parameterization of the model equations is done based on values directly gained from experiments and by optimizing the model output on experimental CV curves. Easily accessible parameters such as temperature T = 298.15 K and the geometrical electrode area A = 0.1963 cm^2 are inserted directly in the model. The electrolyte resistance R = 19 Ω was gained by measuring with EIS and quantifying the real component at a high frequency of 10^5 Hz. A constant double-layer capacitance of C_{dl} = 25 µF cm^{-2} is assumed following experimental findings in the literature[95]. The activities of liquid species at the interface are assumed to be equalized with their respective bulk values due to fast transport. In addition, their concentrations in the electrolyte are very high compared to consumption and production, so the steady-state assumption is plausible. Therefore, relevant electrolyte activities are set to a constant value of $a_{H_2O} = 1$ and $a_{H^+} = c_{H^+}/c_0 = 0.1$ with the standard concentration c_0 = 1 mol L^{-1} to replicate the experimental specifications of the 0.1 M aqueous solution. Proton activity, reported with values of 0.078 [96] and 0.132 [97], might deviate from the assumed value and, thus, influence the parameterized kinetic rate constants of the protonation steps. The constants correlate linearly and perfectly negatively with a possible deviation in proton activity as one proton is transferred at each step. Nevertheless, further results, such as reaction rates and coverages, are unaffected. Standard Gibbs free reaction energy values are as well unaffected due to the correction with respect to electrochemical standard conditions.
The kinetic rate constants of the oxygen adsorption steps for M1 k_{-7} and k_{-8} and for M2 k_{-5} and k_{-6} are set to zero since the oxygen evolution is assumed to be irreversible due to its high reaction energies. The remaining rate constant values k_i, the dimensionless adsorption parameter g_j, and the density of active sites ρ are identified with an optimization algorithm using the third

experimental CV curve at dE_{ext}/dt = 200 mV s^{-1}. This scan rate was chosen as it gives well-pronounced and clearly distinguishable features in the experimental data (see section 3.3.1). The algorithm modifies all parameters successively by a defined value $\pm m$ in case the variation results in a decrease of the root mean square error (rmse) in equation 3.16. This procedure was repeatedly performed until the error reached its minimum and iterated for several modification values $m \in \{10^{-1}, 10^{-2}, 10^{-3}, 10^{-4}\}$ for g_j, 10^m for $k_{\pm i}$ and $10^{0.1 \cdot m}$ for ρ.

$$\mathrm{rmse} = \sqrt{\frac{1}{N}\sum_{n}(j - j_{\mathrm{exp}})^2} \tag{3.16}$$

Since the amount of kinetic parameters is very high, the algorithm for parameter identification uses a two-step procedure. First, the rate constants and adsorption coefficients of reactions $i \in \{1, 2\}$ for M1 and reaction $i \in \{1\}$ for M2 as well as the density of active sites were identified by minimizing the rmse in the potential range $0.45 < E_{ext} < 1.1$ V. This is applicable since the reactions are assumed to occur in this region and be responsible for the observed current peaks. Hence, its parameters are sensitive in this potential region. In a second step, the rest of the rate constants and adsorption coefficients of reactions $i \in \{3, 4, 5, 6, 7, 8\}$ for M1 and reaction $i \in \{2, 3, 4, 5, 6\}$ for M2 were identified by minimizing the rmse at potentials $E > 1.3$ V. With this procedure a set of parameters was obtained, which is able to describe the experimental data at dE_{ext}/dt = 200 mV s^{-1} with sufficient low rmse.

3.3 Results and Discussion

In the following, firstly, the experimentally recorded CV curves are discussed, and the characteristic features are highlighted. Then, the results of the parameterization processes will be given and explained. Simulation results and the quantification of microkinetic insights, such as reaction rates and coverage of intermediate species, are described and discussed. At the end of this section, the thermodynamic parameters from the simulations are deduced and compared with the literature.

3.3.1 Experimental Results

Cyclic voltammograms on hydrous Ir films were recorded in the potential range between E = 0.35 and 1.6 V vs RHE in 0.1 M H_2SO_4. The results for each third cycle are given in Figure 3.3. They exhibit four features in current (A_0, A_1, A_2, and OER) that arise from different electrocatalytic processes: (i) the first anodic peak A_0 at E = 0.6 V is related to the oxidation of the underlying metallic bulk Ir.[95] (ii) Hydrous film oxidation from Ir(III) to Ir(IV) via a PCET step results in the

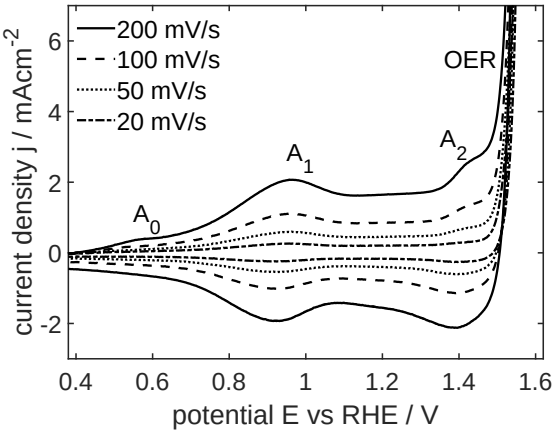

Figure 3.3: Experimentally recorded cyclic voltammograms of hydrous Ir in 0.1 M H_2SO_4 for various scan rates. The third cycle is displayed respectively. Characteristic features A_0, A_1, A_2, and OER are marked.

broadened peak A_1 with an anodic maximum at approximately E = 0.95 V.[74, 98] (iii) A further PCET, resulting in a change of oxidation state from Ir(IV) to Ir(V)[74, 81], takes place at E = 1.4 V and is seen in the feature A_2 prior to (iv) the OER, which is identified with the exponential increase in current at E = 1.5 V. Sufficient peak separation and the correlation with a change in oxidation state by one of each of the features A_1 and A_2 are observed. This allows for the conclusion that the present features are not linked to differently oriented surfaces. The results are, therefore, in agreement with the widely accepted assumption of a porous and amorphous structured material.[67, 99] As can be seen, the different scan rates do not cause a qualitative change in the spectrum; all peaks are still visible in the same potential area. The most pronounced peaks are obtained at 200 mV s^{-1}. The analysis of electrochemical impedance spectra at open circuit potential and high frequency of $f = 10^5$ Hz reveals an electrolyte resistance of R = 19 Ω. There is no impact or limitation due to diffusion in the electrolyte since the rotation of the electrode shows no significant change in current density over the full CV potential range.

3.3.2 Analysis of Adsorption Isotherms

In this section, a brief description is given of the adsorption function taken into account in the model. There are several common adsorption isotherms, so the first step is to evaluate which one describes the present electrocatalytic system best. Therefore, three isotherms are selected from the literature, which are based on the work of Langmuir[58], Temkin/Frumkin [56], and van der Waals/Hill-de Boer[91, 92]. The theory and derivation are given in the literature in detail[55] and briefly summarized in chapter 2. While Langmuir adsorption is restricted to the total number

of adsorption sites, Frumkin adsorption takes into account the interaction of adsorbed species and van der Waals, additionally, the area occupied by each species. We follow up here on the equations derived in section 2.4.1. The conversion of the equation into a form, which takes forward and backward adsorption into account, is done following the work of Laviron[93], who conducted this explicitly for Frumkin adsorption. The implementation of the kinetic equations used in the model (equation 2.18) was deduced from the work of Vidaković[94] and derived in detail in chapter 2. This gives the adsorption functions of a forward f_+ and backward f_- reaction for each respective adsorption process with the surface coverages θ and the symmetry factor β:

$$f_{\pm,\,\text{Langmuir}} = 1 \tag{3.17}$$

$$f_{\pm,\,\text{Frumkin}} = \exp\left(\beta\left[\prod_j (g_j\theta_j)^{\nu_{\pm ij}} - \prod_j (g_j\theta_j)^{\nu_{\mp ij}}\right]\right) \tag{3.18}$$

$$f_{\pm,\,\text{Hill-de Boer}} = \exp\left(\beta\left[\prod_j (g_j\theta_j)^{\nu_{\pm ij}} - \prod_j (g_j\theta_j)^{\nu_{\mp ij}} + \prod_j \frac{\theta_j^{\nu_{\pm ij}}}{\theta_j^{\nu_{\mp ij}}} - \prod_j \frac{\theta_j^{\nu_{\mp ij}}}{\theta_j^{\nu_{\pm ij}}}\right]\right) \tag{3.19}$$

To evaluate which of the adsorption terms describes the electrocatalytic system best, a single electron PCET step of a reduced to an oxidized adsorbed species (Red $\overset{r}{\rightleftharpoons}$ Ox + e^-) is assumed. The reaction is implemented and simulated as described in section 3.2.3. The parameters are optimized onto the feature A_1 ($0.6 < E < 1.1$ V) of the experimental data shown in Figure 3.3.

Table 3.1: Parameter values were identified with the assumption of different adsorption types.

Adsorption type	k_+	k_-	g_{Red}	g_{Ox}	ρ	rmse
	mol m^{-2} s^{-1}		-		mol m^{-2}	mA cm^{-2}
Langmuir	$1.0 \cdot 10^{-9}$	$4.0 \cdot 10^{9}$	-	-	$1.6 \cdot 10^{-4}$	6.2
Frumkin	$5.2 \cdot 10^{-10}$	$2.0 \cdot 10^{9}$	4.7	4.8	$3.4 \cdot 10^{-4}$	2.0
van der Waals	$1.6 \cdot 10^{-10}$	$7.7 \cdot 10^{8}$	3.3	3.5	$5.0 \cdot 10^{-4}$	0.9

The simulation results of modeling several adsorption isotherms in comparison with experimental data in the range $0.4 < E < 1.4$ V are shown in Figure 3.4. Quantifications of best optimization results gain rmse values of 6.2, 2.0, and 0.9 mA cm^{-2} for Langmuir, Frumkin/Temkin, and van der Waals adsorption, respectively. Langmuir fails to describe the experimentally observed broad adsorption peak, as it assumes a surface coverage-independent adsorption energy and thus leads to a narrow peak. This is in agreement with studies reporting that the broad adsorption peak in the CV data can not be explained by Langmuir adsorption [12, 87]. Temkin shows a broader peak as the adsorption energy depends already on coverage, but it is not in line with the experimental

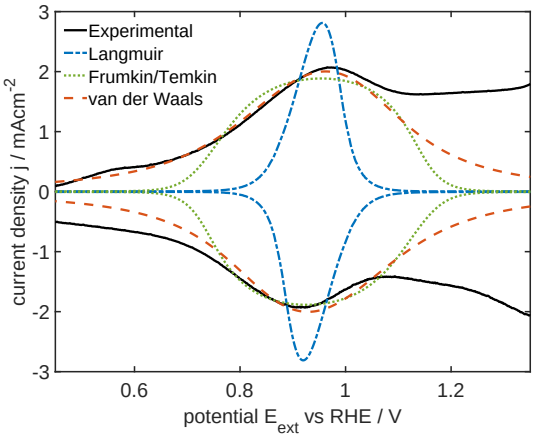

Figure 3.4: Simulation of Langmuir, Frumkin/Temkin, and van der Waals adsorption currents of a PCET reaction in comparison to experimental data. Kinetic parameters (k_+, k_-, g_{Red}, g_{Ox}, and ρ are identified in order to gain the lowest rmse values (equation 3.16) for each of the simulations separately.

data at potentials $E < 0.8$ V and $E > 1.1$ V. In best agreement is the kinetic simulation using van der Waals adsorption as it fits the data over a wide potential range with low rmse value. With these results, it is concluded that van der Waals, also known as Hill-de Boer, adsorption is present at the electrode-electrolyte interface. This is plausible as its theoretical derivation is based on two major assumptions [55], which are both in agreement with the studied electrode system: the defined areal spacing and the interaction of adsorbed species. Hence, Hill-de Boer adsorption $f = f_{\text{Hill-de Boer}}$ is used in the model equation 2.21.

3.3.3 Model Parameters

As explained above, several model parameters are gained from experiments via model-based identification with a potential rate input of $\mathrm{d}E/\mathrm{d}t$ = 200 mV s^{-1}. CV simulations using the identified parameter set for M1 and the parameter set for M2 are in good agreement with the experimental data, as they reproduce the main features observed in the experiment shown in Figures 3.5a and 3.5b. Firstly, the simulation with a scan rate of 200 mV s^{-1} is discussed. The rmse values of the first adsorption process A_1 ($0.75 \leq E \leq 1.1$ V) equals 0.14 mA cm^{-2} for M1 and 0.13 mA cm^{-2} for M2 and display high accuracy. At the second adsorption peak A_2 and OER ($1.3\ \mathrm{V} \leq E$), the respective values for both mechanisms 0.31 (M1) and 0.41 (M2) mA cm^{-2} are slightly higher. Major discrepancies are visible at $E < 0.7$ V and $1.1 < E < 1.3$ V leading to rmse values of 0.27 (M1) and 0.37 mA cm^{-2} (M2) for the full CV. The features in the low potential region around and below A_0 are known to correlate with the reduction of the bulk metallic Ir.[95] This process is not considered in the model, leading thus to the discrepancy at $E < 0.7$ V. The second potential

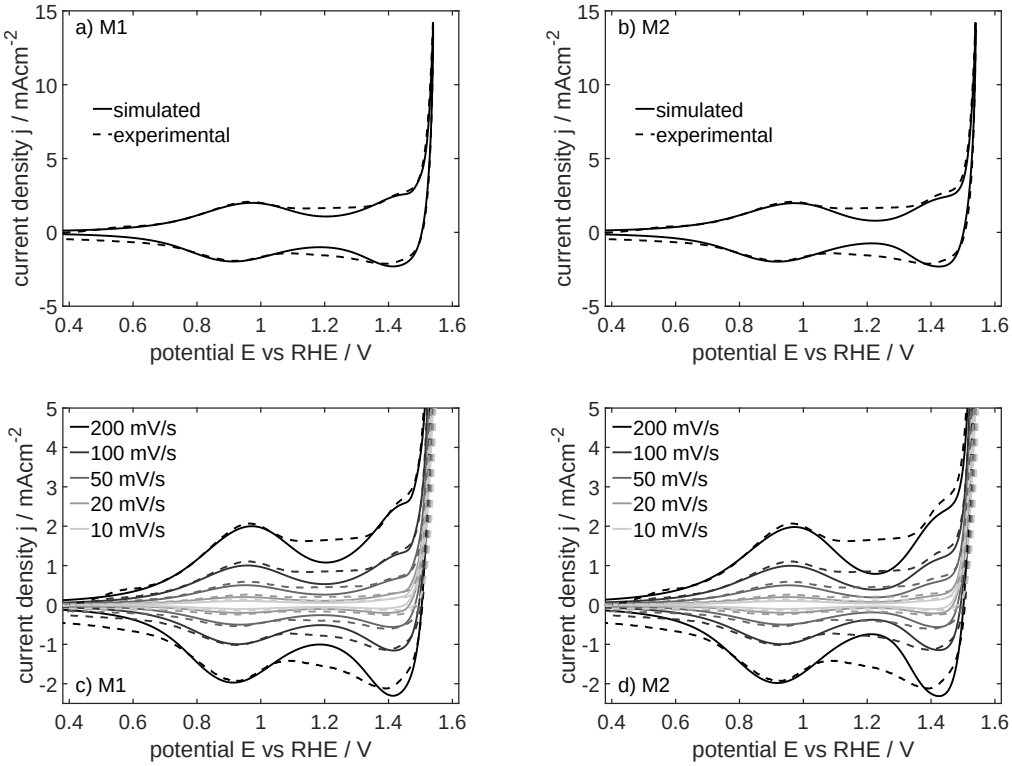

Figure 3.5: Simulated CV curves resulting from the parameter identification process at a potential rate of 200 mV s^{-1} of a) mechanism M1 and b) mechanism M2, in comparison to the third cycle of the experimental results. Using the identified parameters at 200 mV s^{-1}, simulation of CV curves at different potential rates $dE/dt = \{200, 100, 50, 20, 10\}$ mV s^{-1} of c) mechanism M1 and d) mechanism M2 are conducted (line) and plotted with the respective experimental data (dashed line).

region ($1.1 < E < 1.3$ V) might cover either a non-faradaic influence or an additional adsorption process. The model fails to reproduce this feature, and, to the best of my knowledge, neither does any experimental report have an explanation for the behavior observed in this region. Regardless, the discrepancy is comparably small. Both models are also similarly able to reproduce the experimental CV features when changing the scan rate shown in Figures 3.5c and 3.5d. Overall it is concluded that both mechanisms can reproduce the dynamic experimental electrochemical data very well at different potential rates. Thus discrimination needs additional analysis, as discussed in section 3.3.4.

In the following, the identified parameters for the mechanisms M1 and M2 listed in Table 3.2 are discussed. The obtained density of accessible and active sites is roughly two orders of magnitude higher compared to the value reported in the literature for a (110) oriented surface of IrO_2

Table 3.2: Parameter values were identified from the CV curves with mechanisms M1 and M2.

	Mechanism M1				Mechanism M2			
index	k_{+i}	k_{-i}	g_j	ρ	k_{+i}	k_{-i}	g_j	ρ
	mol m^{-2} s^{-1}		-	mol m^{-2}	mol m^{-2} s^{-1}		-	mol m^{-2}
1	$1.0 \cdot 10^{-5}$	$6.3 \cdot 10^{-28}$	0.9	$4.6 \cdot 10^{-4}$	$9.4 \cdot 10^{-12}$	$1.1 \cdot 10^{6}$	3.9	$5.0 \cdot 10^{-4}$
2	$1.0 \cdot 10^{-11}$	$7.1 \cdot 10^{5}$	3.6		$1.9 \cdot 10^{-4}$	$1.3 \cdot 10^{2}$	4.0	
3	$1.3 \cdot 10^{-14}$	$1.5 \cdot 10^{12}$	3.6		$1.4 \cdot 10^{-13}$	$2.7 \cdot 10^{11}$	6.5	
4	$1.0 \cdot 10^{-13}$	$1.9 \cdot 10^{8}$	0.3		$2.0 \cdot 10^{-16}$	$3.7 \cdot 10^{13}$	1.2	
5	$7.8 \cdot 10^{-15}$	$8.8 \cdot 10^{13}$	0.1		$1.0 \cdot 10^{0}$		0.0	
6	$1.6 \cdot 10^{-12}$	$1.8 \cdot 10^{15}$	0.3		$2.4 \cdot 10^{-6}$		0.0	
7	$7.8 \cdot 10^{-12}$		0.0					
8	4.4		0.0					

$\rho_{IrO_2(110)} = 8.3 \cdot 10^{-6}$ mol m^{-2}.[100] The value is plausible as hydrous Ir forms multiple electrochemically active layers during the cyclic treatment [75] prior to the measurement. Although the three-dimensional film is continuously growing with each cycle and with this the number of active sites, the changes during one cycle are rather small. With respect to a preceding study[101], the thickness of the experimentally produced film is estimated to be 3.7 nm after 100 cycles. This results in a volumetric density of active sites in the film of 0.13 mol cm^{-3}. Further, it was found that the adsorption parameter g does influence the van der Waals adsorption terms quite significantly. In some reactions r_i (M1: $i \in \{2, 3\}$; M2: $i \in \{1, 2, 3\}$), high g values lead to flattened but broader faradaic current peaks A_1 and A_2 in the potential region prior to the OER onset. As shown in section 3.3.2, neither Langmuir nor Volmer adsorption allows for a broad peak. Thus, the assumption of a van der Waals isotherm seems to be justified, including the underlying assumption of the areal spacing of surface sites and the interaction of adsorbed species. Kinetic rate constants k of the electrochemical deprotonation steps follow a clear tendency: forward reaction rate constants are lower by more than 20 times the order of magnitude compared to their backward counterparts. This is plausible due to the fact that potential is given versus reversible hydrogen reference electrode and not to the equilibrium potential of each process. As the reaction rates of the chemical reactions are rather independent of the electrochemical potential, consequently, the respective rate constants deviate from this trend. The impact of the parameter values on the microkinetics and a detailed discussion about the reaction rates, the coverages, and the thermodynamics of the system is given in the following sections for both mechanisms M1 and M2 separately.

3.3.4 Microkinetic Insights of Mechanism M1

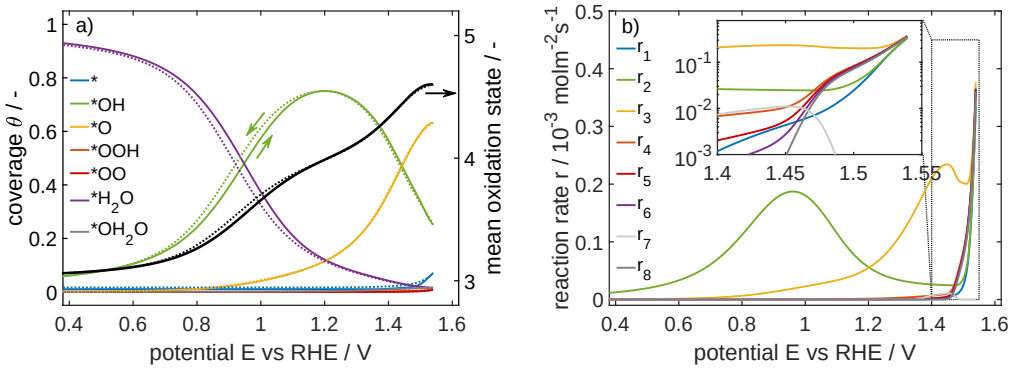

Figure 3.6: Simulation results of mechanism M1. a) Coverage of intermediate surface species with dynamically upwards (bold lines) and downwards (dotted lines) sweeping potential on the left axis. The mean iridium oxidation state value is indicated by the bold black line with respect to the right axis. b) Effective reaction rates during the forward scan of the CV.

Figure 3.6a shows the surface coverages, and Figure 3.6b the reaction rates calculated for mechanism M1. The first and second PCET steps, i.e. the oxidation resulting in adsorbed species *OH and *O, dominate the pre-OER potential region. Both can be assigned to define the respective current peaks A_1 and A_2 reaching effective reaction rates $r_i = r_{+i} - r_{-i}$ of r_2 = 0.19 and r_3 = 0.24 mmol m^{-2} s^{-1}. In this region, all other reactions are slow, with effective rates below 0.05 mmol m^{-2} s^{-1}. At potentials E > 1.5 V, O_2 is predominantly forming via the single site pathway ($^*\mathrm{OO} \xrightarrow{r_8} {}^* + \mathrm{O_2}$). The effective oxygen production rate reaches its maximum of r_8 = 0.36 mmol m^{-2} s^{-1} at the highest simulated potential. Production rate via the dual site reaction pathway $2\,{}^*\mathrm{O} \xrightarrow{r_7} 2\,{}^* + \mathrm{O_2}$, in which two oxygen atoms from neighboring sites form one oxygen molecule as assumed in the reaction step 7 is calculated to $r_7 < 0.29 \cdot 10^{-6}$ mmol m^{-2} s^{-1} and thus multiple orders of magnitude slower. Whereas during lower potentials prior to the OER, rates of reactions occur individually, the increase in potential in the OER region comes with an increase in multiple reaction rates. This is clearly visible in the inset of Figure 3.6b. Except for the dual site step, all other reactions in the cycle converge to the same curve, which allows a continuous oxygen evolution under the participation of all oxidation states. In the potential range from 0.4 < E < 1.2 V, reaction $^*\mathrm{H_2O} \overset{r_2}{\rightleftharpoons} {}^*\mathrm{OH} + \mathrm{H^+} + \mathrm{e^-}$ is predominant, which results in a high amount of present $^*\mathrm{OH} \equiv$ Ir(IV) of 25.1 %. At higher potentials above 1.2 V, the second deprotonation reaction rate $^*\mathrm{OH} \overset{r_3}{\rightleftharpoons} {}^*\mathrm{O} + \mathrm{H^+} + \mathrm{e^-}$ increases significantly and produces a considerable amount of adsorbed *O. This is additionally supported by the fact that chemical H_2O adsorption via step $^*\mathrm{O} + \mathrm{H_2O} \overset{r_4}{\rightleftharpoons} {}^*\mathrm{OH_2O}$ is balanced heavily towards the side of the educt. The resulting availability of *O gives rise to r_7 and the OER. The minor extent of the oxygen production via this pathway

might be explained by high activation barriers, as there are two sites involved. At potentials above 1.45 V, the rate of this dual-site pathway rapidly decreases because the competing pathway, including the steps r_4, r_5, r_6, and r_8, becomes favorable. The inset of Figure 3.6b shows that all four reaction rates converge and ascend exponentially. The increase in potential accelerates especially the effective rates of both deprotonation steps $^*OH_2O \overset{r_5}{\rightleftharpoons} {}^*OOH + H^+ + e^-$ and $^*OOH \overset{r_6}{\rightleftharpoons} {}^*OO + H^+ + e^-$. In consequence, the chemical adsorption rate r_4 follows to compensate for the depletion of $^*OH_2O$, and oxygen is chemically evolving with a rate r_8 directly linked to the amount of produced $^*OO$.
Regardless of the increase in reactions r_4, r_5, r_6, and r_8, $^*O \equiv$ Ir(V) remains the major available intermediate species and covers 63.4 % of the surface sites. This is explained only by a limitation of the overall cyclic process by the chemical H_2O adsorption r_4. H_2O adsorption, therefore, is a crucial step. This becomes additionally visible in the slight increase in the number of free surface sites * at potentials above 1.5 V up to a total amount of 7.0 % at 1.55 V. In Figure 3.6a, slow H_2O adsorption r_1 forces the first deprotonation reaction rate r_2 to undercut the single site OER rate r_8. As r_1 tends to converge with r_8 from below and the reduced intermediate species $^* \equiv$ Ir(III) is produced, this H_2O step is limiting at high potentials.
Overall, for mechanism M1, one can conclude that the definition of the rate-determining step becomes challenging in the dynamic context. An accumulation of three species Ir(III), Ir(IV), and Ir(V) is occurring at the high potentials $E > 1.5$ V relevant for electrolysis. This is a clear sign that the subsequent reactions r_1, r_4, and r_5, which use these species as reactants, are slow and define the overall turnover.

3.3.5 Microkinetic Insights of Mechanism M2

For mechanism M2, surface coverages and reaction rates are shown in Figures 3.7a and 3.7b, respectively. In analogon to mechanism M1, there are distinct regions in the pre-OER potential region in which one or two reactions are dominant. At potentials below 1.2 V, deprotonation via reaction $^*H \overset{r_1}{\rightleftharpoons} {}^* + H^+ + e^-$ describes the feature A_1, and the slow H_2O adsorption leads to an accumulation of $^* \equiv IrO_2 \equiv$ Ir(IV) species. Above 1.2 V, H_2O adsorption $^* + H_2O \overset{r_2}{\rightleftharpoons} {}^*H_2O$ and the deprotonation $^*H_2O \overset{r_3}{\rightleftharpoons} {}^*OH + H^+ + e^-$ increase significantly and are the major observed reactions. Hence, the amount of present $^*OH \equiv$ Ir(V) rises with higher potentials and enables oxygen to evolve chemically via the dual site pathway $2\,{}^*OH \xrightarrow{r_5} 2\,{}^*H + O_2$. The oxygen evolution via this pathway reaches its highest rate of $r_5 < 0.25$ mmol m^{-2} s^{-1} at the highest simulated potential. The second OER pathway $2\,{}^*O \xrightarrow{r_6} 2\,{}^* + O_2$ becomes dominant at potentials above 1.52 V since potential-driven deprotonation $^*OH \overset{r_4}{\rightleftharpoons} {}^*O + H^+ + e^-$ provides a sufficient amount of $^*O \equiv$ Ir(VI). Both rates r_4 and r_6 converge at the highest potential at a value of 0.43 mmol m^{-2} s^{-1} and are comparably faster than r_5. At OER potentials, each of the processes of H_2O adsorption r_2

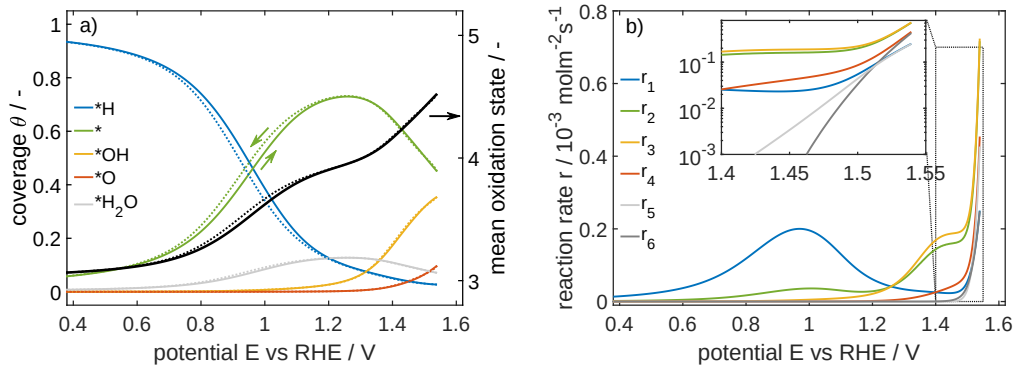

Figure 3.7: Simulation results of mechanism M2. a) Coverage of intermediate surface species with dynamically upwards (bold lines) and downwards (dotted lines) sweeping potential on the left axis. The mean iridium oxidation state value is indicated by the bold black line with respect to the right axis. b) Effective reaction rates during the forward scan of the CV.

and deprotonation r_3 equal the total oxygen evolution rate, i.e., the sum of both oxygen evolving steps r_5 and r_6. Since species $^* \equiv$ Ir(IV) accumulates and covers 45.0 % of the surface sites, even at high potentials, the H_2O adsorption step is mainly limiting both OER pathways. Additionally, both oxygen evolution pathways are determined by the chemical desorption of oxygen r_5 and r_6, since they converge from below and both of the reactants Ir(V) and Ir(VI) are present with quite a high amount of 35.5 % and 9.8 %, respectively.
In conclusion, the oxygen evolution in mechanism M2 is, as well as in mechanism M1, limited due to H_2O adsorption and due to the dual site desorption of oxygen. An accumulation of three species, Ir(IV), Ir(V), and Ir(VI), is occurring, and the respective subsequent reactions r_2, r_3, and r_6 define the overall turnover.

3.3.6 Surface Coverage of Intermediate Species and Oxidation States

With the change in the intermediate states over the whole potential range, the mean oxidation state increases monotonously from +3 to approximately +4.7. The ascending trend matches X-ray spectroscopy results at the Ir L_1 and L_3 edges[80, 81] quite well. At an OER potential of 1.6 V vs RHE, the surface species Ir(V) covers 63.4 % and 35.5 % of the surface for the mechanisms M1 and M2, respectively, which also is found to be present experimentally by X-ray spectroscopy measurements[81]. Ir(IV) covers 25.1 % (M1) and 45.0 % (M2). Interestingly, in mechanism M1 the fraction of the reduced species Ir(III) increases with high potentials, starting from its minimum of 0.01 % at 1.35 V vs RHE to a coverage of 7.0 % at the highest simulated potential. This species arises due to a limitation of the non-electrochemically driven adsorption reaction

of H_2O, as discussed above. A reported analysis of X-ray spectroscopy results matches these findings as it suggests the presence of a species with a low oxidation state of +3.3±0.2[81]. In contrast, the simulation of mechanism M2 exhibits Ir(III) to decrease strictly monotonic to a value of 2.7 % at OER potentials.
Thus, one may conclude the following: both mechanisms strongly differ in the adsorbed species and oxidation states, and only M1 shows some more reduced species at very high potentials. Further, M1 matches and also explains experimental findings of low oxidation states at high potentials. They are attributed to a slow water adsorption process. This suggests that the theory-derived mechanism, M1, seems to be the more likely mechanism and that accelerating OER requires better water adsorption at the catalyst.

3.3.7 Thermodynamic Analysis

The presented microkinetic models use the transition state theory. This allows the calculation of thermodynamic Gibbs free reaction energies ΔG_r right away from the simulation results for each reaction i:

$$\Delta G_{\mathrm{r},i} = -k_\mathrm{B}T \cdot \ln\left(\frac{k_{+i}}{k_{-i}}\right) \tag{3.20}$$

In the experimental setup, the reversible hydrogen electrode serves as a reference at pH $\approx$ 1. In consequence, all parameters are identified with respect to this special condition. in order to allow appropriate comparability with other studies, the energy value is corrected with respect to the generally accepted electrochemical standard conditions. This is conducted by using the following equation:

$$\Delta G^0_{\mathrm{r},i} = \Delta G_{\mathrm{r},i} + k_\mathrm{B}T \cdot \ln(a_{\mathrm{H}^+}) \tag{3.21}$$

The results of the PCET and H_2O adsorption steps are given in Figure 3.8a for mechanism M1 and Figure 3.8b for mechanism M2. Additionally, the standard Gibbs free energy of 1.23 eV of the overall oxygen formation is represented by the dotted line. In M1 the overall catalytic process is limited mainly by the highest energy value, which is $\Delta G^0_{\mathrm{r},5}$ = 1.60 eV. Step 6 follows without further thermodynamic limitation since $\Delta G^0_{\mathrm{r},6} < \Delta G^0_{\mathrm{r},5}$. Values gained for the electrochemical steps in mechanism M1 are qualitatively in good agreement with DFT-based calculations for rutile (110) IrO_2 surface[84]. This suggests the hydrous iridium mechanism M1 to be related to IrO_2 DFT results not only from a mechanistic point of view but as well backed by the thermodynamic analysis. In M2, the most unfavorable and, hence, limiting step is $\Delta G^0_{\mathrm{r},4}$ = 1.67 eV. No comparable values are found in the literature for M2.
Specific H_2O adsorption energies are calculated to $\Delta G^0_{\mathrm{r},1}$ = -135.4 kJ mol^{-1} at Ir(III) and $\Delta G^0_{\mathrm{r},4}$

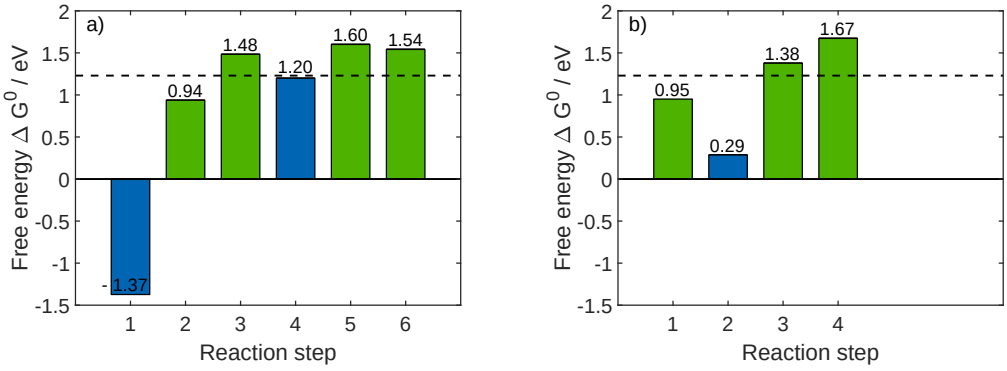

Figure 3.8: Gibbs free energy for the electrochemical deprotonation reactions (green) and H_2O adsorption steps (light blue) at the hydrous Ir surface under electrochemical standard conditions for a) mechanism M1 and b) mechanism M2.

= 114.5 kJ mol^{-1} at Ir(V) for mechanism M1 and $\Delta G^0_{r,2}$ = 31.4 kJ mol^{-1} at Ir(IV) for mechanism M2. In comparison, the calculation for (110) and (011) surfaces of rutile IrO_2 by *ab initio* molecular dynamics[102] obtain energy values of $\Delta E_{(110)}$ = -211.5 kJ mol^{-1} and $\Delta E_{(011)}$ = -145.9 kJ mol^{-1} for dissociative H_2O adsorption. This shows for $\Delta G^0_{r,1}$ of M1 good agreement with *ab initio* results.

Only taking the thermodynamics into account reveals a simplified description: the energy values are directly correlated to the potentials, above which the oxidation product of the respective reaction is energetically favorable. Thermodynamic energies are widely gained *ab initio* with DFT[17, 84] and used to calculate CV curves with the generalized computational electrode method[103]. But since the OER is a highly dynamic reaction cycle, an analysis purely based on energy values might be oversimplified. The energy diagram of mechanism M1 claims the formation of Ir(VI) via reaction r_5 to be energetically favorable at potentials higher than 1.60 V and with this the overall OER. In contrast, the results of the kinetic study suggest Ir(V), Ir(IV), and Ir(III) be present in descending order and give evidence that oxygen is already produced. Such details need to be taken into account while analyzing complex catalytic systems. Still, the energy diagrams provide an outstanding way to compare DFT-based calculations with kinetic modeling. Overall one can conclude that energy values provide an elegant way to validate microkinetic models or compare the results with other methods, such as molecular dynamics or DFT-based calculations. A study approach purely based on thermodynamics simplifies the occurrence of multiple surface species and misses out on important insights regarding kinetics.

3.4 Concluding Remarks

Within this chapter, a systematic model-assisted approach is presented to evaluate mechanistic reaction pathways, underlying blocking species, and limiting reactions, as well as to quantify essential microkinetic parameters based on CV. For the first time, electrocatalytic surface adsorption and deprotonation steps prior to and during the OER on hydrous Ir are analyzed based on microkinetic modeling. Two reaction mechanisms were compared: while mechanism M1 is inspired by DFT studies and mechanism M2 is proposed based on experimental insights, both are able to describe experimental CV data properly. However, findings of reduced Ir(III) species at typical OER potentials and low water adsorption energy indicate clearly that only the DFT-inspired mechanism M1 is able to describe the catalytic system to the full extent. Simulations based on this mechanism give potential-dependent reaction rates for individual electrocatalytic steps. Oxygen is predominantly formed via a single site pathway $^{*}\mathrm{OO} \xrightarrow{r_8} {}^{*} + \mathrm{O_2}$. Dual site evolution although occurring at a less oxidized Ir state is negligible. Stepwise deprotonation by consecutive PCET processes reveals an increasing mean oxidation state ranging from +III at 0.45 V up to approximately +4.7 at 1.55 V. This goes along with the formation of higher oxidized intermediate states, which results in a surface covered by roughly 7 % Ir(III), 25 % Ir(IV) and 63 % Ir(V) species at 1.55 V. During the OER, non-electrochemically driven and therefore comparably slow H_2O adsorption was found to be a crucial step in the electrocatalytic cycle. This explains experimental findings of reduced Ir(III) species at high potentials and further, water adsorption is also identified as a slow step at lower potentials. Furthermore, the Gibbs free energies and the H_2O adsorption energy were found to be equivalent to values calculated by DFT and *ab initio* molecular dynamic simulations. By considering these findings, mechanism M1 and the presented kinetics are able to describe all major aspects of the OER. The results suggest, that the search for catalysts and process conditions which favor or support the adsorption of water at the surface might be a promising subject for further investigations to increase the activity of the OER.
Besides analyzing the mechanistic details as shown in this chapter, the applied modeling method can also provide insights into the degradation behavior of OER catalysts. This is especially relevant for long term electrolyzer operation and will be covered in the following chapter 4, in which a model based analysis of the highly stable rutile structured IrO_2 is presented.

4 Analysis of the Oxygen Evolution Performance at Different Stages of Iridium Oxide Degradation[4]

4.1 Introduction

Multiple OER catalysts have been screened over the last decade. Among them, IrO_2 was found to outperform most active transition metals and their oxides and it provides the highest stability under harsh process conditions with strong oxidizing potentials in acidic media.[12, 13] Therefore, it is considered a benchmark material in PEM water electrolysis.[6, 7, 41, 106] However, due to its global scarcity, the efficient use of the material is of high interest in the scientific community.[107] Recent research focuses on the performance of the material and the degradation behavior under OER operation.

In a PEM cell assembly operated at 3 A cm^{-2}, only minor overpotentials are induced by hydrogen mass transport (~20 mV), proton conduction resistance (~20 mV), and the ohmic losses are reported to account for 155 mV.[6] The major loss arises due to the OER kinetics, even for high active IrO_2 quantified with an overpotential of about ~350 mV in the PEM cell assembly.[6] An in-depth understanding of the microkinetics at the surface and the kinetically and thermodynamically limiting processes is, thus, of significant interest to optimize the catalytic system. Moreover, high operation potentials are applied to reach technically relevant conversion rates. These provoke side reactions and processes that lead to catalyst degradation and, as a result, a lowered activity.[108] A recently reported process that leads to a performance decrease during operation is the formation of nano- and micro-sized oxygen bubbles in the electrolyte phase.[109]

[4] Parts of this chapter have been published in the following articles:
[1] **Geppert, J.**; Röse, P.; Czioska, S.; Escalera-López, D.; Boubnov, A.; Saraçi, E.; Cherevko, S.; Grunwaldt, J.-D.; Krewer, U. *J. Am. Chem. Soc.* **2022**, *144*, 13205-13217.
[104] Czioska, S.; Boubnov, A.; Escalera-López, D.; **Geppert, J.**; Zagalskaya, A.; Röse, P.; Saraçi, E.; Alexandrov, V.; Krewer, U.; Cherevko, S.; Grunwaldt, J.-D. *ACS Catal.*, **2021**, *11*, 10043-10057.
[105] Czioska, S.; Ehelebe, K.; **Geppert, J.**; Escalera-López, D.; Boubnov, A.; Saraçi, E.; Mayerhöfer, B.; Krewer, U.; Cherevko, S.; Grunwaldt, J.-D. *ChemElectroChem* **2022**, *9*, e202200514.
Results that did not originate from the work of the author of this dissertation are marked accordingly.

As a degradation process, the dissolution of the active IrO_2 material was detected and quantified using a scanning flow cell coupled downstream to an inductively coupled plasma mass spectrometer.[12, 110] The use of *operando* XAS has recently proven the formation of oxygen vacancies during the OER.[104] Interestingly, their formation led to a stabilization of crystalline IrO_2. The extent and way in which degradation affects the microkinetics of the IrO_2 surface processes is still unresolved, although it accounts for the major impact on the catalytic performance. This demonstrates the urgent need to analyze and quantify activity-defining processes at the catalyst surface and their degradation-related changes under operation conditions.

The electrocatalytic activity of IrO_2 is explained by adsorbed intermediates that pave a thermodynamically efficient pathway alongside the reaction coordinate of the OER.[17, 46] Although the free-energy values were extensively studied by DFT approaches,[44, 47] the reaction energies and even the identified reaction that constitutes the overpotential defining step vary drastically with the applied computational details.[111] Kinetic modeling approaches have been employed to circumvent this issue. They rely on rate equations parameterized by Tafel slope data and DFT results to study the energy profile and the coverage of the surface at different applied potentials under steady-state conditions.[112, 113] Recent analyses suggest two different rate-determining steps depending on the applied overpotential,[114] and a corresponding change in the charge is correlated to the surface coverage of adsorbed species.[115]

Experimental studies on rutile structured IrO_2, prepared by exposing it to increasing calcination temperatures, widely conclude on increasing electrocatalytic stability but decreasing activity.[77, 110] In a recent interesting work, the kinetics of the stability-related dissolution processes was modeled with a network structure approach.[116] So far, there are no reported microkinetic studies on the effect of degradation on the OER kinetics on rutile IrO_2 itself. However, the effect of material degradation on the OER performance is one of the most relevant issues to address to ensure long-term stability. In general, degradation studies are rare and focus mostly on experimentally observable values such as overpotential and current density.[117] To date, it is still unknown which interactions of surface processes define the OER performance on IrO_2, and how they change due to operation-related degradation. In the present chapter, the novel model-assisted microkinetic methodology is provided for the degradation analysis of electrocatalysts using CV and employed for the first time for the degradation analysis of the important OER benchmark catalyst. This allows to access and quantify all relevant degradation parameters, thus enabling a holistic understanding of the OER performance.

Present state-of-the-art approaches for the model-based reaction analysis of the OER use DFT to calculate energy values for ideal catalyst surfaces with ideal conditions, not nanoparticulated catalysts in an electrolyte. Only a few microkinetic modeling studies on the OER on IrO_2 exist, where ideal DFT values predict the microkinetics and process rates.[44, 112] In contrast, the method presented here starts at the experiment and quantifies the kinetics and thermodynamic energies from dynamic experimental data using a kinetic model. This ensures a realistic analysis of the complex situation at the nanoparticulated catalyst surface of CV experiments. Analyzing

the drift of these parameters with time due to degradation is a further natural step presented in this chapter, which does not require bottom-up guessing of degradation mechanisms. The methodology can, thus, be applied to analyze catalyst surfaces during OER operation over multiple hours. Herewith, not only the performance limitations are revealed, but also the effect of catalyst degradation on the most relevant thermodynamic parameters.
The structure is as follows: After presenting the model and its parameterization using experimental CV results, the energy profile alongside the OER reaction coordinate is revealed, and the limiting surface processes on the pristine IrO_2 material over a wide potential range are identified. Due to the fact that the model approach is not restricted to a particular material state, degradation-related changes of the geometry as well as energy parameters are quantified, and the performance losses are traced back to changes in the energies of single reaction steps. As a result, this study provides essential new mechanistic, kinetic, and thermodynamic insights into the OER performance at degrading IrO_2.

4.2 Methods

In this section, the formulation of the OER mechanism, the microkinetic model, and the experimental methods are described. The methodology comprises the following steps: firstly, the reaction mechanism of the surface processes is identified based on already published studies. Based on the mechanism, rate equations for the processes at the electrode surface are formulated. To reproduce experimental CV data, the reaction rates are determined for a dynamic input signal, a cyclic potential in $E(t)$, by balancing the coverage of all adsorbed surface species. In addition, the resulting time-dependent current density $j(t)$ is calculated by employing a charge balance. To estimate the unknown kinetic energy parameters and the density of active sites, global and local optimization algorithms are used, which identify those values that allow to best reproduce the experimental data. The procedure is used for fresh and degraded catalysts alike.

4.2.1 The OER Mechanism on Rutile IrO_2

The first step in the methodology comprises the formulation of a detailed OER mechanism on rutile IrO_2, which provides the basis for the microkinetic model. Over the last decades, multiple OER mechanisms were used to explain the electrocatalytic formation of oxygen from water.[46] A selection of proposed mechanisms was reported recently for iridium oxide by Naito et al.[118] Using DFT, a four-step proton-coupled electron transfer mechanism has been proposed for OER on IrO_2[17]: on the free Ir CUS denoted with *, adsorbed intermediates *OH, *O and *OOH

are formed by deprotonation of either water or the adsorbed species itself. Recent DFT studies show process limitations due to oxygen detachment and water adsorption.[44, 47] Similar limitations are found with the kinetic model for OER on hydrous IrO_x as described in chapter 3.[3] To take these steps into account, the four-step proton-coupled electron-transfer mechanism of Rossmeisl et al.[17] is complemented by elementary reaction steps on water adsorption and oxygen detachment, which results in the assumption of three additional surface species: $^*OO$, $^*H_2O$, and $^*OH_2O$. For the latter species, DFT results disagree on whether it is energetically favorable for one of the protons to adsorb on a neighboring $^*O$ site[44] or on the outermost lattice oxygen[47]. In the mechanism for the microkinetic kinetic model, a single site is assumed as further discrimination does not affect the kinetics. The proposed mechanism here is given with equations 4.1 to 4.7 and consists of two water adsorption steps: equations 4.1 and 4.4, four deprotonation steps: equations 4.2, 4.3, 4.5, and 4.6, and the oxygen detachment: equation 4.7.

$$^* + H_2O \overset{r_1}{\rightleftharpoons} {}^*H_2O \tag{4.1}$$

$$^*H_2O \overset{r_2}{\rightleftharpoons} {}^*OH + H^+ + e^- \tag{4.2}$$

$$^*OH \overset{r_3}{\rightleftharpoons} {}^*O + H^+ + e^- \tag{4.3}$$

$$^*O + H_2O \overset{r_4}{\rightleftharpoons} {}^*OH_2O \tag{4.4}$$

$$^*OH_2O \overset{r_5}{\rightleftharpoons} {}^*OOH + H^+ + e^- \tag{4.5}$$

$$^*OOH \overset{r_6}{\rightleftharpoons} {}^*OO + H^+ + e^- \tag{4.6}$$

$$^*OO \overset{r_7}{\rightarrow} {}^* + O_2 \tag{4.7}$$

4.2.2 Microkinetic Model

In this section, the mathematical model is briefly summarized. The input function is defined as the electrode potential $E(t)$ in the form of equation 2.24. Reaction rates are implemented with equation 2.18, in which a_j is the activity of the electrolyte species $j \in \Omega_{\text{el}} = \{H^+;\ H_2O;\ O_2\}$, and θ_j is the surface coverage of adsorbed species and the free sites * $j \in \Omega_{\text{sur}} = \{^*;\ ^*H_2O;\ ^*OH;\ ^*O;\ ^*OH_2O;\ ^*OOH;\ ^*OO\}$. The matrix of stoichiometric coefficients $\boldsymbol{\nu} = \boldsymbol{\nu}_+ - \boldsymbol{\nu}_-$ of all species Ω and reactions r are given in equations 4.8 and 4.9, respectively.

$$\boldsymbol{\nu}_{+} = \overbrace{\begin{matrix} 0 & 1 & 0 & 0 & 1 & 0 & 0 & 0 & 0 & 0 & 0 \\ 0 & 0 & 0 & 0 & 0 & 1 & 0 & 0 & 0 & 0 & 0 \\ 0 & 0 & 0 & 0 & 0 & 0 & 1 & 0 & 0 & 0 & 0 \\ 0 & 1 & 0 & 0 & 0 & 0 & 0 & 1 & 0 & 0 & 0 \\ 0 & 0 & 0 & 0 & 0 & 0 & 0 & 0 & 1 & 0 & 0 \\ 0 & 0 & 0 & 0 & 0 & 0 & 0 & 0 & 0 & 1 & 0 \\ 0 & 0 & 0 & 0 & 0 & 0 & 0 & 0 & 0 & 0 & 1 \end{matrix}}^{j \in \Omega = \{H^+;\ H_2O;\ O_2;\ e^-;\ *;\ {}^*H_2O;\ {}^*OH;\ {}^*O;\ {}^*OH_2O;\ {}^*OOH;\ {}^*OO\}} \tag{4.8}$$

$$\boldsymbol{\nu}_{-} = \begin{pmatrix} 0 & 0 & 0 & 0 & 0 & 1 & 0 & 0 & 0 & 0 & 0 \\ 1 & 0 & 0 & 1 & 0 & 0 & 1 & 0 & 0 & 0 & 0 \\ 1 & 0 & 0 & 1 & 0 & 0 & 0 & 1 & 0 & 0 & 0 \\ 0 & 0 & 0 & 0 & 0 & 0 & 0 & 0 & 1 & 0 & 0 \\ 1 & 0 & 0 & 1 & 0 & 0 & 0 & 0 & 0 & 1 & 0 \\ 1 & 0 & 0 & 1 & 0 & 0 & 0 & 0 & 0 & 0 & 1 \\ 0 & 0 & 1 & 0 & 1 & 0 & 0 & 0 & 0 & 0 & 0 \end{pmatrix} \tag{4.9}$$

To consider the effect of changes in the surface energy state due to areal spacing of the surface sites and the lateral interaction energy of adsorbed species $\Delta G_{\mathrm{int},j}$, the function of the van der Waals isotherm, also known as the Hill-de Boer isotherm, is adapted to the model in the form of a function $f(\theta)$, which is described in detail elsewhere[3, 55, 57] and in section 2.4 and given in equation 2.21. The surface species balance and the charge balance by taking equation 2.22 and equation 2.23 into account, respectively.

4.2.3 Model Parameterization

The final step in the modeling methodology contains parameterization. Experimental parameters such as electrolyte resistance R = 18.2 Ω, electrode area A = 0.1963 cm^2, the activity of electrolyte species a_{H^+} = 0.2 and a_{H_2O} = 1 and temperature T = 298.15 K can be inserted directly, as well as the stoichiometric parameters, which are deduced from the mechanism. The symmetry factor β = 0.5 and the pre-exponential frequency factor k_0 = 343.2 s^{-1} are defined by the symmetric peak-to-peak position as described in section 2.5.
The remaining parameters, that is, the energy values, the density of active sites, and the double-layer capacitance, need to be determined from the CV measurements. The process of model-based parameter identification is of major importance to gain a reliable and valid model. Two identification algorithms were combined. In the first step, the dynamic model output of one million randomly selected sets of parameters was compared to experimental CV data by evaluating

the rmse. The 250 sets with the best agreement were further optimized locally by minimizing the rmse with a pattern search algorithm. Details of the overall procedure are given in appendix A.2. For the parameterization of the processes at the degraded material, the pattern search algorithm is employed and values of the previous modeled state are used as initial parameter values.
To avoid model overfitting by the usage of an unjustified high number of model parameters, four main requirements are considered. First, only physical parameters are used, which are well established in the recent literature. Second, the mechanism is chosen based on widely accepted insights in the scientific community working on the OER on IrO_2 and on further materials. Thirdly, experimental CV curves are selected to get the maximum number of characteristic features to correlate them to kinetic steps. Fourth, the model validity is tested by predictions of further experiments, such as dynamic CV curves with other scan rates or steady-state polarization curves.
With the described model approach, one is able to reproduce and analyze the ongoing electrocatalytic processes at the electrode surface, which will be discussed in detail in the result section. Prior to this, the experimental characterization of the catalytic material is briefly introduced.

4.2.4 Experimental Characterization

The IrO_2 nanoparticles used in this study were provided by the Institute for Chemical Technology and Polymer Chemistry at KIT. They were produced by flame spray pyrolysis and have been calcined at 600 °C.[104, 110] In previous publications by Escalera-López et al.[110] and Czioska et al.[104], they have been extensively characterized by physical methods such as transmission electron microscopy, XPS, X-ray diffraction, and *operando* XAS, as well as by electrochemical methods such as CV and potential steps, whereas the dissolution was analyzed with an inductively coupled plasma mass spectrometer.[5]
For the experimental electrochemical analysis in this study CV, EIS, and chronoamperometry measurements are used. All electrochemical experiments were conducted with a working electrode from PINE research Instrumentation Inc., which consists of a glassy carbon disc electrode tip fixed in a PEEK shroud with an available circular area of $A = 0.1963\ cm^2$. Back-sided electric connection to a Gamry Reference 600+ potentiostat was ensured via the rotator shaft of a RDE setup from PINE research Instrumentation Inc. Deionized water (16 MΩ cm) was used for rinsing the PTFE cell prior to the experiments, and as a solvent to prepare the aqueous 0.1 M H_2SO_4 electrolyte solution from concentrated sulfuric acid (98 %, Carl Roth). The catalyst ink was prepared by weighing 2 mg of the IrO_2 nanoparticles and adding 750 µL of deionized water, 250 µL of isopropanol, and 8.58 µL of Nafion 5 % dispersion (D-520, VWR). Further, 1.2 µL of

[5] Production of the particles, X-ray diffraction and *operando* XAS characterization were done by S. Czioska. Transmission electron microscopy, XPS and dissolution measurements were conducted by D. Escalera-López.

1 M KOH is added to achieve a pH value of ca. 11, which is reported to homogenize particle distribution on the electrode.[119] After ultrasonication for 10 min, 10 µL of the dispersion was dropped onto the glassy carbon electrode, which had been mirror-polished with 0.05 µm alumina suspension prior to drop-coating. To gain a uniform film distribution,[120] the electrode was rotated at 700 rpm for 30 min during drying under atmospheric conditions. The procedure resulted in a catalyst loading of approximately 0.1 mg_{cat} cm^{-2}.

For the electrochemical experiments, a Pt wire and a HydroFlex RHE from Gaskatel GmbH served as counter and reference electrodes in the 250 mL aqueous 0.1 M H_2SO_4 electrolyte solution, respectively. Electrochemical analysis of the pristine catalyst material was conducted by, first, potentiostatic impedance spectroscopy at the open-circuit potential with frequencies from $f = 10^5$ to 10^{-1} Hz and a perturbation amplitude of $\hat{E}$ = 10 mV. Second, three consecutive cyclic voltammograms were recorded at each of the following scan rates: dE/dt = {200, 100, 50, 25, 200} mV s^{-1} in between potentials of E = 0.05 and 1.60 V. All potentials are given with respect to RHE and were *iR*-corrected after the measurements by the electrolyte resistance R, which in turn was gained from the impedance spectra at high frequencies at a phase angle of $\phi = 0°$.

Degradation of the catalyst was monitored with the following protocol: first, potentiostatic impedance spectroscopy at the open-circuit potential was conducted as described before to monitor electrolyte resistance. Next, three consecutive cyclic voltammograms with a potential scan rate of dE/dt = 200 mV s^{-1} in between potentials of E = 0.05 and 1.60 V were performed, followed by holding a constant operation potential of 1.2, 1.5, 1.55 or 1.6 V for 30 min. The variation in operation potentials allows studying conditions at which no, low, moderate, and high OER activity can be expected, respectively. This step was repeated 30 times, which resulted in 30 sets of CV measurements over an operating time span of roughly 15 hours for each operation potential. For better visualization, only CV curves after every 150 min and only the last of three CV measurements of the respective set will be shown in the result section. At the end of the degradation test, the impedance measurement was repeated to reveal possible changes in the electrolyte resistance. The electrode was rotated at 2000 rpm during the complete protocol to ensure fast electrolyte transport and avoid the blockage of the catalytically active area by evolving oxygen bubbles.

For characterization of the steady-state, polarization curves were measured under a constant rotation of 2000 rpm. To guarantee reproducibility, the protocol consists of two subsequent sequences of 17 constant potential steps, where each potential is held for 120 s. The first sequence was conducted by starting at 1.4 V and increasing by 0.025 V up to 1.8 V, and the second sequence was conducted by decreasing the potential after each step by 0.025 V back to 1.4 V. The measurement was repeated three times on freshly prepared electrodes, and the current measured at the end of each potential step was used to calculate the mean value and standard deviation over all measurements at a certain potential.

4.3 Results and Discussion

In this section, the experimental CV results are discussed first; then, the identified model parameter values are analyzed, and the interplay of surface processes and their impact are revealed under dynamic and steady-state conditions. In the last subsection, this analysis is extended to degraded catalyst states, in which the impact of material degradation on the electrocatalytic performance and parameters is explained.

4.3.1 Experimentally Observed Electrocatalytic Behavior

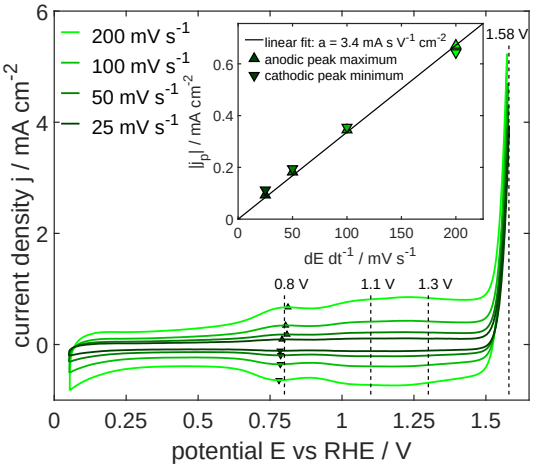

Figure 4.1: Cyclic voltammograms of pristine rutile IrO_2 nanoparticles in 0.1 M H_2SO_4 at different scan rates. The inset shows the linear current behavior of the absolute peak maximum at around 0.8 V. All potentials are referred to RHE and are *iR*-corrected.

In the following, the experimental CV curves are analyzed to identify features that correspond to electrochemical reactions and analyze the changes in these features, which relate to catalyst degradation. Figure 4.1 shows the third cycle of CV curves at various potential scan rates. The *iR*-corrected OER overpotential is quantified to 350 mV at the lowest potential rate of 25 mV s^{-1} and at a current density of 4 mA cm^{-2} or roughly 40 mA mg_{cat}^{-1}, which is similar to previously reported data with minor deviations due to the particle size and geometric area.[12, 41, 121] Currents in $0.25 < E < 1.5$ V vs RHE depend linearly on the applied potential scan rate, which is exemplarily shown for the maximum peak position at 0.8 V in the inset of Figure 4.1 and are, therefore, attributed to pseudocapacitive processes. Constant current contributions at $0.25 < E < 0.5$ V occur due to the charging of the double layer. Above 0.5 V, three partially overlapping redox transitions

are visible at roughly 0.8, 1.1, and 1.3 V, which are reported in the literature as subsequent deprotonation steps oxidizing the Ir CUS and the adsorbed oxygen.[83, 106, 115, 122] The transition at approximately 0.8 V is correlated to the first deprotonation step $^*H_2O \rightleftharpoons {}^*OH + H^+ + e^-$. This is in good agreement with DFT calculations of this reaction on (110) IrO_2, which gave reaction free energy values of ΔG_r = 0.67 to 0.88 eV, depending on the employed revised Perdew-Burke-Ernzerhof functionals accounting for van der Waals interactions and assuming the presence of explicit water.[111] The broad response in current in $0.9 < E < 1.5$ V covers approximately double the amount of transferred charges of the previously discussed transition. It is thus attributed to two deprotonation steps $^*OH \rightleftharpoons {}^*O + H^+ + e^-$ and $^*OH_2O \rightleftharpoons {}^*OOH + H^+ + e^-$ with higher reaction free energy values, ranging from ΔG_r = 1.21 to 1.56 eV and from ΔG_r = 1.26 to 1.68 eV, respectively.[111] The exponential current increase at potentials $E > 1.5$ V implies that all species in the circular mechanism are rapidly reacting in the forward direction, driving the formation of molecular oxygen. In conclusion, the CV curves show four different electrochemically limited current response features and provide a substantial data set to identify the model parameters. This will allow us to differentiate further processes by the model-based approach, which are not easily accessible with experiments, and to analyze their interactions and performance limitations of the pristine IrO_2.

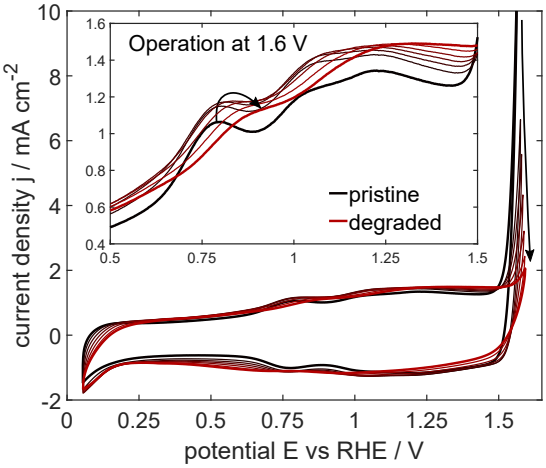

Figure 4.2: Changes in experimental CV curves with a scan rate of 200 mV s^{-1} during 15 h of OER operation at a constant potential of 1.6 V vs RHE. The third CV curve, recorded every 150 min, is displayed with colors changing from pristine (black) to degraded state (red); changes are indicated by arrows. The inset magnifies the shift in anodic redox transitions.

One of the major concerns regarding the actual performance of a catalyst material is its long-term stability. Therefore, the long-term electrochemical behavior of the IrO_2 nanoparticles was monitored by (i) applying a constant potential at which the OER occurs for 15 h in total and

(ii) measuring during these 15 h cyclic voltammograms every 30 min in order to gain dynamic current response of the steadily degrading system. The resulting CV curves in Figure 4.2 show a strong decrease in the OER current density at the maximum applied potential of 1.6 V from 10.4 to 2.1 mA cm^{-2}. This follows other literature reports stating that the catalytic system undergoes strong degradation in acidic media.[123] Interestingly, at potentials below OER, a slight absolute increase in the redox transition current is observed, alongside a shift of the anodic deprotonation peak positions toward higher potentials (inset of Figure 4.2) and of the cathodic peak positions toward lower potentials. Both effects, the decrease of OER current and the gradual change in the redox transitions, are strongly dependent on the applied operation potential: experimental results at lower operation potentials reveal significantly smaller changes and, thus, lower degradation, as shown in Figure 4.3.

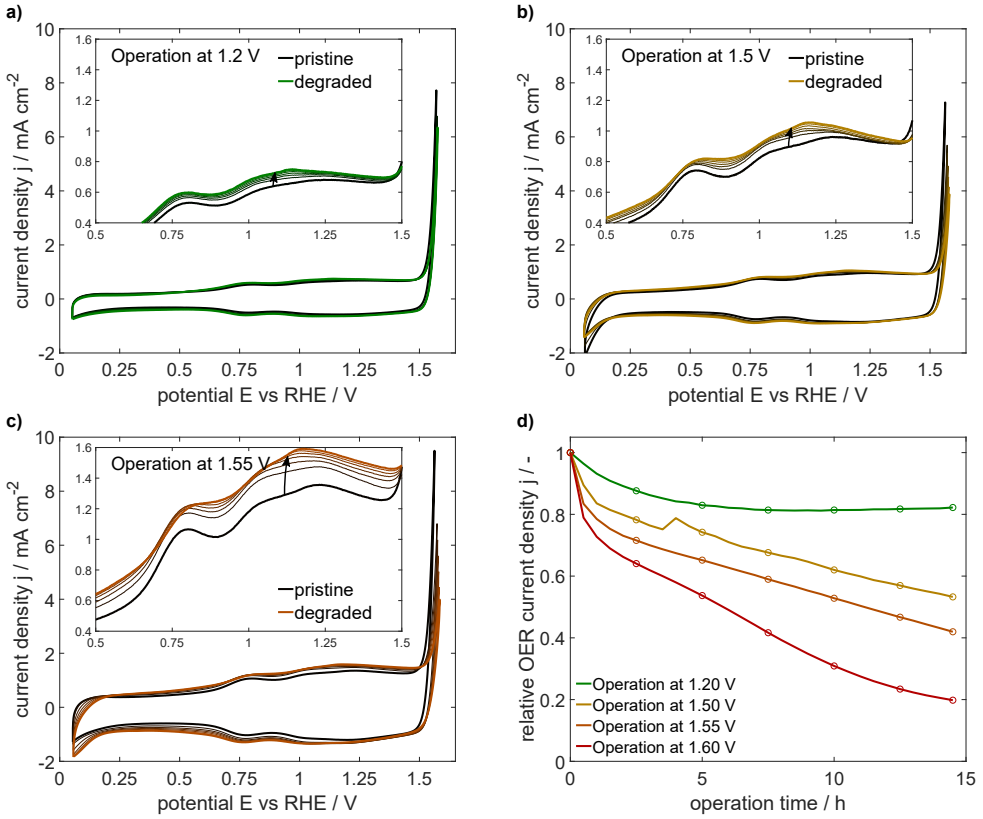

Figure 4.3: CV curves are recorded every 150 min in between applying a constant potential of a) 1.2, b) 1.5, and c) 1.55 V over 15 h. The respective insets show the shift of the anodic redox transition with operating time. d) Relative change in current density at the highest applied potential during the CV is shown over the operation time.

The application of a constant operating potential for a total duration of 15 hours in the acidic electrolyte leads to a decrease in the OER activity of the catalytic system. The dependence of changes in the CV on the constant potential is shown in Figure 4.3 for 1.2, 1.5, 1.55, and 1.6 V. The CV curves recorded every 150 minutes during the 15 hours constant potential protocol are given. Only a minor absolute increase in redox transition current density and a decrease of OER turnover frequency of 19 % is observable for the CV recorded in between an operation at a potential of 1.2 V in Figure 4.3a. Both observations are even more pronounced with higher applied potentials of 1.5 V in Figure 4.3b and 1.55 V in Figure 4.3c. This reveals a bigger loss in OER activity with higher applied potential, as indicated by the relative OER loss in Figure 4.3d. It is noteworthy that no decrease in the redox transition current is observed in the insets of Figures 4.3a to 4.3c, which indicates that, in this case, a loss of active material or the blockage by oxygen bubbles can be neglected. The EIS measurements at open circuit potential prior to and after the protocol exhibit the electrolyte resistances to vary insignificantly with values changing from R = 19.2 to 19.0 Ω, from R = 26.0 to 24.8 Ω, remaining constant at R = 20.0 Ω and changing from R = 18.2 to 18.4 Ω at the applied potentials of 1.2, 1.5, 1.55 and 1.6 V respectively.

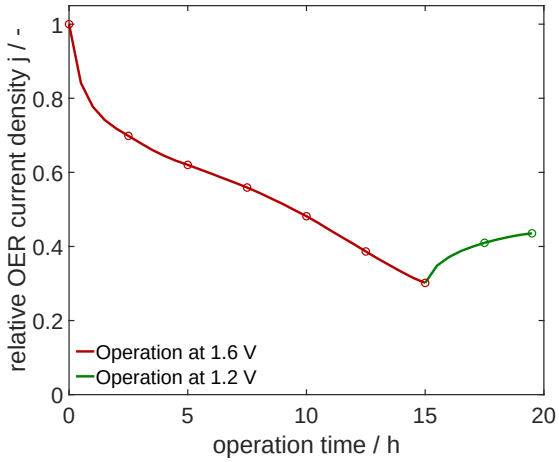

Figure 4.4: Change in relative current density of the CV curves in between applying a constant potential of 1.6 V over 15 h followed by a constant potential of 1.2 V over 5 h.

This change in performance cannot be attributed to electrolyte concentration changes, as discussed in the following. The electrolyte resistance before and after all long-term measurements remained almost constant. Therefore, a significant change in the concentration of protonic charge carriers and, thus, pH value is disproved. Further, the local oxygen concentration gradient is held constant due to a high electrode rotation speed of 2000 rpm. One might argue that the formation of oxygen micro-bubbles leads to a decrease in catalytic currents, as recently reported.[109]

However, in the experiments, it is clearly shown that the absolute current of the redox transitions does not decrease and, thus, possibly produced bubbles at high potentials are either reduced completely while applying reductive potentials prior to the third of the consecutive cyclic scans or transported away from the electrode by the fast electrode rotation. Also, only a slight recovery of the activity is observable in Figure 4.4 while applying a moderate constant potential of 1.2 V for 5 h after the OER operation for 15 h. Anyhow, no major blockage of active surface sites is detectable in the CV curves. In summary, this change in dynamic current behavior due to long-term operation is attributed exclusively due to the progressive degradation of the catalytic material itself.

In the following section, two remaining aspects will be tackled by the model-based analysis: first, which microkinetic processes are affected by this material degradation, and second, how to quantify the change leading to this loss in activity with physically meaningful values. Beforehand, the parameters and the simulation output of the pristine material are discussed, which reveal the performance-limiting steps.

4.3.2 Energies and Further Model Parameters

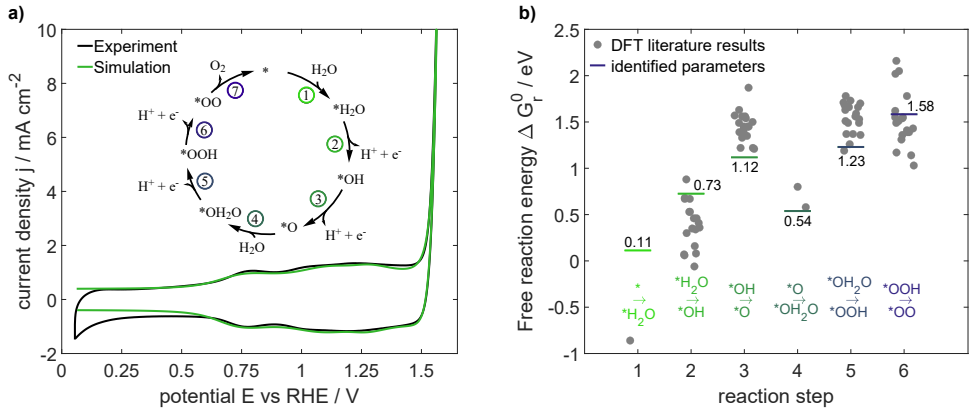

Figure 4.5: a) Comparison of the experimental and simulated CV curves for a scan rate of 200 mV s^{-1} at the pristine state with the best set of parameters. b) Identified reaction free energy parameters for steps 1-6 at electrochemical standard conditions in comparison to DFT-calculated values reported in the literature.[44, 47, 111] Adsorbed reactants are displayed for each of the reaction steps, that is, equations 4.1 to 4.6.

With the parameter estimation procedure described in the method section, a set of parameters was elaborated, which allows the reproduction of the experimental CV data with extremely low deviation (a rmse value of 0.066 mA cm^{-2}), as seen in Figure 4.5a. All major features, the redox transitions, and the exponential increase of the OER are reproduced. The soundness of the model and its parameterization are further confirmed, as the simulations with the same parameter set

can also reproduce experimental cyclic voltammograms at different scan rates: the scan rate dependence of the cyclic voltammograms and the features matches nicely, as shown in the appendix in Figure A.4e and A.4f. This is a further clear indication that the model is not overfitted. In addition, profile rmse analysis was conducted on the reaction free energy parameters. The results given in appendix A.3 confirm the high parameter identifiability. The resulting energy parameter values for the pristine catalytic system are listed in Table 4.1 and will be discussed in the following paragraphs to give a sound analysis of the model-based findings. Further identified parameters are the double-layer capacitance of C_{dl} = 19.4 F m^{-2} and the density of active sites of $\rho = 1.40 \cdot 10^{-4}$ mol m^{-2}.

Table 4.1: Values for the reaction free energy, the activation free energy, and the reactant species interaction energy of reaction steps 1 to 7 on IrO_2 identified by reproducing CV with the microkinetic model.

step	ΔG_r^0 / eV	ΔG_a / eV	ΔG_{int} / eV
1	0.11	0.15	0.18
2	0.73	0	0.10
3	1.12	0	0.11
4	0.54	0	0.13
5	1.23	0	0
6	1.58	0.04	0.03
7	-0.39	0.43	0.02

Figure 4.5b allows a comparison of the reaction free energies at electrochemical standard conditions to reported values obtained by DFT. The high fluctuations in the DFT-based values are due to different revised Perdew-Burke-Ernzerhof functionals. For all electrochemical processes, that are, reaction steps 2, 3, 5, and 6 with respective equations 4.2, 4.3, 4.5, and 4.6, the energies estimated by the kinetic model are in good accordance with the DFT studies.[47, 111] Also, the reaction energy of the second water adsorption step, equation 4.4, matches the range of reported data. Only the first water adsorption step, equation 4.1, differs roughly 1 eV from the single available DFT-based literature value.[44] To the best of my knowledge, no further values are reported to compare with, probably because the intermediate species $^*H_2O$ was often neglected in DFT studies as it is not electrochemically limiting. As the DFT-values for the other steps showed strong deviations and thus reliance on a single DFT-value is not recommended, a wide range of -3 eV up to 1 eV for this parameter is evaluated, in which a value of 0.11 eV was identified to describe the dynamic behavior best. It is concluded that this methodology enabled indeed to

identify the free reaction energies of the mechanism while nicely describing the dynamic behavior.

Activation free energies describe the energy barriers of transition states along a reaction coordinate. For all electrochemical deprotonation processes, low values of 0.04 and 0 eV, as shown in Table 4.1, were identified, and, thus, no or marginal barriers hamper the protons to desorb. This is in good agreement with a barrier of < 0.05 eV reported in a recent DFT study.[112] Water adsorption steps are also found to face marginal activation energies of $\Delta G_{a,1}$ = 0.15 eV or $\Delta G_{a,4}$ = 0 eV. In contrast, a high activation energy $\Delta G_{a,7}$ = 0.43 eV is identified for the oxygen detachment process ($^*OO \rightarrow {}^* + O_2$), meaning that the microkinetic reaction rate is restrained by an additional energy barrier alongside the reaction coordinate, which is in accordance to a recently reported DFT study.[47]

The interaction energies of adsorbed species ΔG_{int} are also identified with the model-based approach and are given in Table 4.1. Derived by Frumkin[56] and de Boer[55], the interaction energy in equation 2.21 affects the adsorption process with increasing coverage of the adsorbed species. A physically meaningful ascription is given by two independent interpretations: (i) de Boer stated that the energy covers lateral molecular interactions, nowadays known as van der Waals forces.[55] This explanation does hold for the studied catalytic system since permanent charges and dipoles are involved in the adsorption process. (ii) Temkin, in contrast, accounts for a non-uniform catalytic surface.[124] As for IrO_2 nanoparticles, different surface orientations, (110), (101), and (100), are reported by analyzing the Wulff construction;[102, 125] also, the explanation by Temkin is applicable to this material. In a recent DFT study by Rao et al. on electrocatalytically highly related RuO_2, free energies of adsorbed species occurring in the OER mechanism were found to differ due to the different assumed facets with values ranging from 0.02 eV up to 0.33 eV.[22] In conclusion, both reported interpretations hold for the studied catalytic system and might influence the adsorption process. The interaction energy values were identified for the multiple species as given in Table 4.1 and range from 0 eV for $^*OH_2O$ to 0.18 eV for the free active site *. This is in the range of values reported for the adsorption of different alcohols.[63, 126] From a microkinetic point of view, a higher interaction energy of a reactant species increases the reaction rate initially due to high reactant coverage but lowers the rate by the ongoing production of the product species. This behavior leads to the broadened current response of the electrochemical reactions shown exemplarily for a PCET step in Figure 2.4. Although the microkinetic analysis is able to quantitatively identify the interaction energies very precisely, future research may focus on this parameter to elucidate its origin and to prospectively resolve whether the behavior is caused by different surface facets or the impact of van der Waals interactions of neighboring species.

The estimated specific double-layer capacitance is C_{dl} = 19.4 F m^{-2} with respect to the geometrical electrode area. It is in good agreement with previously reported data.[127] The density of active sites is quantified to $\rho = 1.40 \cdot 10^{-4}$ mol m^{-2}, which corresponds to 84.2 sites per nm^{-2} with respect to the geometrical electrode area. Assuming nominal particles with an iridium to oxygen

ratio of 1:2, a percentage of 3.1 % of all iridium atoms contained in the particles serve as active sites for electrocatalysis.

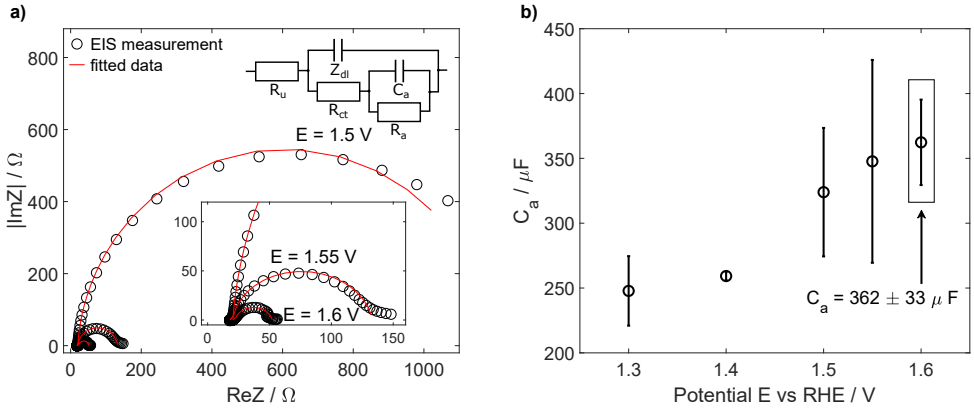

Figure 4.6: a) Measured EIS and the best fit gained with the displayed equivalent circuit model are shown for three different potentials. b) Mean fitted values for the adsorption capacitance are given, with errors denoting the standard deviation of two independently analyzed measurements.

To evaluate the electroactive surface area (ECSA), a method reported by the group of Bandarenka[128] was applied, using their reference value for the specific adsorption capacitance of IrO_x. For this analysis, impedance spectroscopy measurements were conducted at potentials of 1.3, 1.4, 1.5, 1.55, and 1.6 V with frequencies from $f = 10^5$ to 10^-1 Hz and a perturbation amplitude of E = 10 mV. Selective results are shown in Figure 4.6a, and following Bandarenka's publication, a simple equivalent circuit model was used to reproduce the spectra and identify parameters.[128] Thus, the adsorption capacitance C_a was quantified as given in Figure 4.6b. It is the only parameter correlated to the ECSA. It shows the same increasing trend with increasing potential up to 1.6 V, as reported for IrO_x.[128] To determine the ECSA from C_a, the procedure and value of the active-area specific adsorption capacitance C'_a from the Bandarenka group are used[128]. Here, the capacitance $C_{a,B}$ measured by EIS was normalized to the $ECSA_B$ of an IrO_x thin film determined by atomic force microscopy, which resulted in $C'_a = C_{a,B}/ECSA_B$ = 135 ± 25 µF cm^{-2}. This value is used to calculate the actual ECSA of the present system ECSA = C_a/C'_a = 2.7 ± 0.6 cm^2, which is consequently 13.7 ± 2.8 times larger than the geometrical electrode surface. By combining this value with the model-based identified density of the active site, the actual density value normalized to the ECSA of $\rho_{ECSA} = \rho \cdot A \cdot ECSA^{-1}$ = 6.2 ± 1.3 nm^{-2} is received. This value can now be directly compared to reported literature values. It is in good agreement with the reported iridium CUS density in rutile IrO_2 (110) and (100) facets of 5 and 7 nm^{-2}, respectively.[100] The large uncertainty arises due to the quantification of the specific adsorption capacitance from the impedance spectra.

The above given in-depth analysis and literature comparison proves that the model-based parameter identification process applied on CV curves provides reliably estimated values of the thermodynamic energies, the double-layer capacitance, and the density of active sites. The physically meaningful parameters are in good overall accordance with reported data and independently describe different aspects of the catalytic system. Thus, it is conclusively shown that the present model is not overfitted. With this fully parameterized physicochemical model, the interplay of reactions and surface species and the resulting impact on the performance and its kinetic limitations will be analyzed in the following.

4.3.3 Interplay of Surface Processes and their Kinetic Impact

To gain an understanding of the relationship between electrochemical behavior, the performance of the catalyst, and the microkinetic processes, a model-based analysis is conducted. The advantage of a parameterized microkinetic model is the possibility to analyze with it the behavior and interactions of elementary reaction steps as well as single limitations that affect the overall electrochemical behavior and performance at a given potential. For this purpose, CV simulations with a scan rate of 200 mV s^{-1} are analyzed to provide insights into the reversible and potential-dependent changes in reaction rates and the surface coverage of adsorbed species. The evolution of these variables over the third full cycle is shown in Figure 4.7.

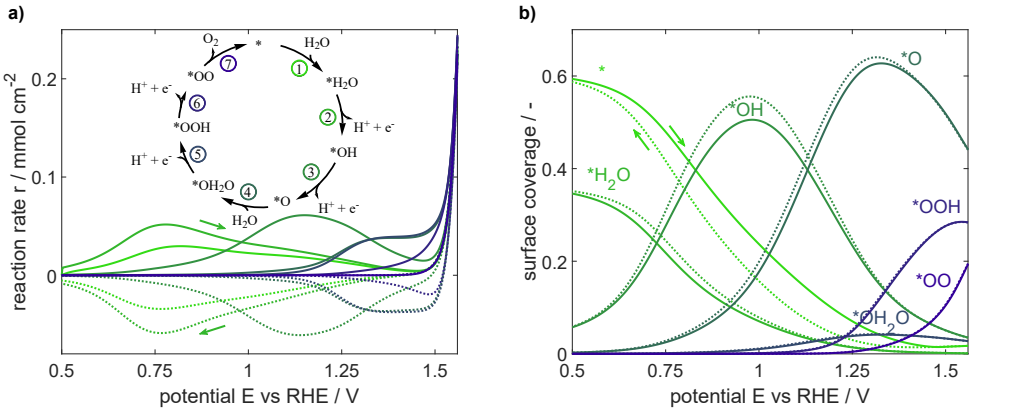

Figure 4.7: Simulated a) effective reaction rates according to the color-coded mechanism in the inset and b) surface coverages of adsorbed species during a cyclic voltammogram with a scan rate of 200 mV s^{-1}. Solid and dashed lines indicate forward and backward potential cycling directions, respectively, as indicated by the arrows.

High reversibility of all reactions can be concluded from the similar coverage curves for forward and backward scans and the corresponding mirrored reaction rates. Furthermore, it is clearly

observable that at different potentials, individual reactions kinetically limit the electrocatalytic conversion. At low potentials up to 0.9 V, water adsorption ($^* + H_2O \rightleftharpoons {}^*H_2O$) and the following deprotonation step ($^*H_2O \rightleftharpoons {}^*OH + H^+ + e^-$) are predominant, resulting in an increase in adsorbed *OH. In the potential range from 0.9 up to 1.3 V, the second deprotonation process ($^*OH \rightleftharpoons {}^*O + H^+ + e^-$) sets in and becomes predominant, resulting in a high amount of *O covering the surface's active sites with a share of up to 60 % at ∼1.3 V. With the further increase of the potential above 1.3 V, the amount of *O slightly decreases to 44 % and the amount of *OOH increases. As two deprotonation processes, that is, production of *O and of *OOH, occur predominantly in the potential range from 0.9 up to 1.5 V, the experimentally observed broadened current feature comprises the transferred charges of both processes. Above 1.5 V, further reactions, including oxygen release, set in, which finally leads to an exponential rise of oxygen evolution and, thus, the overall OER turnover frequency. The fact that *O only slowly decreases and very little $^*OH_2O$ can be observed suggests that water adsorption partially limits the OER. This outcome is expectable as, in contrast to the electrochemical steps, which accelerate with potential, chemical rates are not directly dependent on the applied potential. In addition, the fourth deprotonation step ($^*OOH \rightleftharpoons {}^*OO + H^+ + e^-$) is observable to limit the overall OER electrochemically as its rate increases rather only slightly at a high potential of 1.5 V and, hence, it contributes significantly to the overpotential of the OER. The limitation is also manifested in the high coverage share of 28 % of adsorbed *OOH at 1.56 V. At the highest simulated potential of 1.56 V, *OO species accumulate and cover a share of 20 % of the surface. This indicates a third limitation in the oxygen detachment step ($^*OO \rightarrow {}^* + O_2$). It is worth mentioning that this step is not explicitly influenced by the applied potential as no electrons are transferred; however, it is indirectly impacted as its rate depends on the coverage of the surface with the reactant species *OO, which gets significantly increased with a higher potential as shown in Figure 4.7b.

From the dynamically simulated coverages of adsorbed species, the mean oxidation state of the iridium active site is derived. Starting from the free iridium CUS $^* \equiv Ir^{o+\delta}$ with the nominal oxidation state o and $\delta = 0$, the difference δ assigns the further influence due to the adsorption processes.[118] Therefore, for the following adsorbed species, the difference in iridium oxidation state is given: $^*: \ \delta = 0,\ ^*H_2O: \delta = 0,\ ^*OH: \delta = 1,\ ^*O: \delta = 2,\ ^*OH_2O: \delta = 2,\ ^*OOH: \delta = 1,\ ^*OO: \delta = 1$. The surface coverage, which corresponds to the share of surface covered by a species or its probability to be found at the surface, is multiplied by the difference in oxidation state. The results are shown in Figure 4.8 for direct comparison to *operando* XAS measurements[6], which were published by Czioska et al. in [105] and described in detail there. In direct comparison to the white line peak position of the Ir L_3-edge absorption spectra at constant applied potentials, simulated and experimental results correspond to two main trends: (i) For both, an increase in the mean oxidation state with potential is observed in the range of 0.6 to 1.35 V.

[6] *Operando* XAS measurements are conducted by S. Czioska, A. Boubnov and J. Geppert. Data analysis was done by S. Czioska and A. Boubnov.

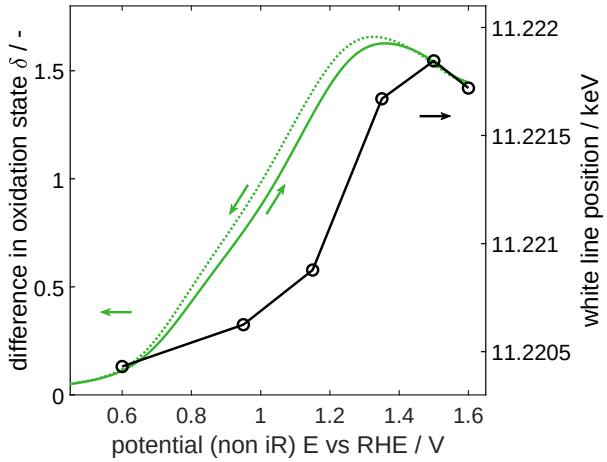

Figure 4.8: Potential dependence of the simulated difference in mean oxidation state and the white line position of the absorption edge measured by *operando* XAS from Czisoka et al.[105].

(ii) Both also show that at higher potentials, a maximum oxidation state is reached, after which the oxidation state decreases. Thus, the active sites are reduced. The stepwise oxidation is accompanied by an increase in the mean oxidation state of Ir CUS by roughly 1.6. This trend is confirmed by performing X-ray adsorption measurements, which result in a corresponding shift of the absorption edge in *operando* X-ray absorption spectra. The connecting point between microkinetic modeling of IrO_2 and *operando* spectroscopy is a helpful link to correlate insights and study further catalytic materials.

An intuitive way to visualize the limitations by electrochemical and chemical steps as a function of potential is shown in the energy diagram in Figure 4.9. Such representation allows us to easily study the changes in energy levels with respect to potential. Figure 4.9 shows that the low activation energies of deprotonation steps facilitate the highly reversible microkinetics. The only notable activation barrier is found to be present for the oxygen detachment step, step 7. It leads to a limitation in the OER. At high potentials of 1.58V, besides this step, only the reaction energies of both water adsorption steps pose an additional notable energy barrier. All three limitations can be kinetically overcome by increasing the amount of the respective reactant species. However, this is at the cost of the subsequent reactions: for example, the third deprotonation step ($^*OH_2O \rightleftharpoons {}^*OOH + H^+ + e^-$) proceeds at a potential roughly 0.5 V higher compared to the second deprotonation step ($^*OH \rightleftharpoons {}^*O + H^+ + e^-$) shown in Figure 4.7a, although both reaction energies differ only by about 0.11 eV. Here, the kinetic analysis provides further input to describe the interactions. The scarce availability of $^*OH_2O$ due to the sluggish water adsorption process consequently increases the potential at which the subsequent electrochemically driven reaction kicks in. This is particularly relevant at the highest potential of 1.58 V: Here, all electrochemical

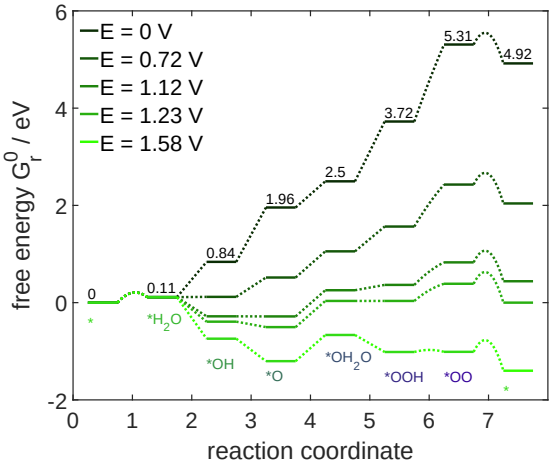

Figure 4.9: Energy diagram for the oxygen evolution microkinetics for potentials between 0 and 1.58 V vs RHE. Displayed are the cumulated reaction energies (plateaus) and activation energies (dashed lines) of the single steps 1 - 7 (equations 4.1 - 4.7). The numbers given at $E = 0$ V are the free energy values at electrochemical standard conditions of $a = 1$ and $T = 25$ °C.

reactions are thermodynamically favorable, but the high amount of the reactant species *O and *OO, which are required for the two chemical steps of water adsorption and oxygen detachment, respectively, indicates that especially these steps limit the overall OER cycle. Since no electrons are transferred in both steps, they are not explicitly accelerated by higher applied potentials. The reader should bear in mind that this is a dynamic scan. Whether the limitations are similar during steady-state operation will be analyzed in the following section.

4.3.4 Polarization Behaviour

Cyclic voltammograms are inherently dynamic and do not show steady-state behavior and limitations as they would occur during the practical operation of PEM water electrolyzers. Here instead, steady-state measurements such as a polarization curve are of more help. Therefore, the CV-parameterized model is analyzed for its steady-state performance and checked whether it could reproduce experimental behavior and aim to analyze the underlying loss processes. This is accomplished by comparing experimental polarization results to simulated ones, as shown in the Tafel plot in Figure 6. The original energy parameter set from the CV simulations was taken, and a good match was achieved between the experiment and the simulation. This proves that the model, which was parameterized with CV curves up to 1.58 V, is not only able to reproduce steady-state behavior in the same range but also able to predict even the steady-state currents at

higher OER potentials such as 1.67 V. This positive outcome confirms the validity of the presented OER model and its parameters. It should be further noted that – as to be expected for such a complex process – the simple approach of mapping the kinetics to a single Tafel slope is not feasible: both curves show a slightly curved profile with a continuously changing slope, which is especially visible for the simulation. Thus, there is not a single Tafel slope across the OER operating window, neither experimentally nor in simulation. This corresponds to a recent analysis of published Tafel slopes for CO_2 reduction, which showed an extremely broad distribution between ca. 30 and 200 mV dec^{-1}.[129] It is thus highly recommended to conduct model-assisted microkinetic analysis, as given in this work, to understand such limitations.

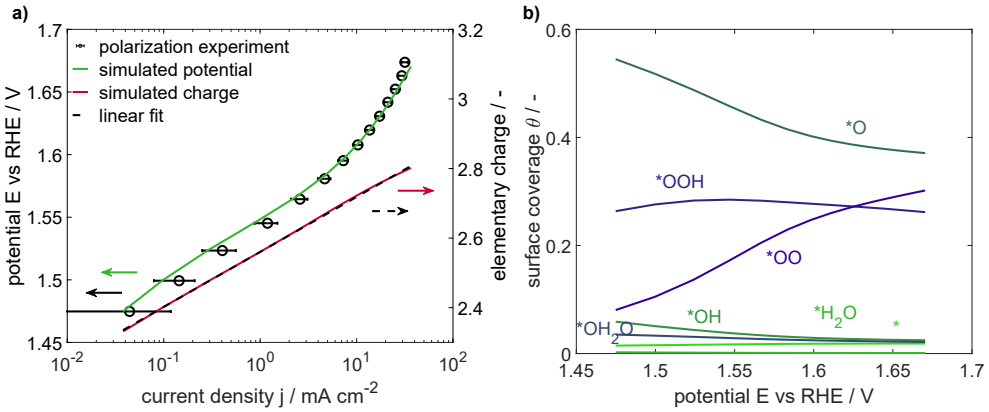

Figure 4.10: a) Experimental and simulated polarization curves for technically relevant potentials and the simulated change in elementary charge per active site. Experiments were repeated three times. b) Corresponding surface coverages of the steady-state simulation.

The corresponding coverages of surface sites during the OER are also given in Figure 4.10 and show interesting additional insights: the surface is mostly covered by species *O, *OOH, and *OO, which corresponds to slow water adsorption on *O, slow deprotonation of *OOH and slow O_2 desorption.

While most of the species remain at a rather constant amount, the share of adsorbed oxygen *O continues to decrease with potential down to 37 %, and conversely, the share of the *OO species increases up to 30 %. As a consequence, this replacement leads to a change in accumulated charge in the surface species. By calculating the number of accumulated elementary charges per active site, a logarithmic increase in the number of elementary charges per active site with current density is found, increasing from 2.3 e at 1.47 V to 2.8 e at 1.67 V, as displayed in Figure 4.10a. This logarithmic trend was recently reported as a common relation of the OER[115], and further confirms the validity of the microkinetic model. This model-based analysis shows clearly that not only the potential-driven reaction ($^*\mathrm{OOH} \rightleftharpoons {}^*\mathrm{OO} + \mathrm{H}^+ + \mathrm{e}^-$) is limiting, but also the

two chemical steps, the water adsorption on $^*O$ and O_2 detachment, are limiting. Therefore it is proposed that an increase in OER activity and performance of the Ir oxide can be reached by improving the ability to adsorb water and detach $^*OO$ species efficiently. It is concluded that the microkinetic model is a powerful and versatile tool for in-depth analysis of the OER behavior of Ir oxide. This brings us to the last part of this chapter, where the model is used to answer the question of how the kinetic behavior changes during catalyst degradation.

4.3.5 Kinetic Changes due to Degradation

Understanding the process of degradation of a catalyst and its performance opens the opportunity for knowledge-driven improvement of its long-term stability. Loss in activity may be associated with a change in the mechanism[130], which would require adapting the model equations. Alternatively, it may be related to a loss in active sites or in their ability to catalyze the reaction steps efficiently. The latter would be reflected by a change in the model parameters for the kinetics (e.g., free energies) or of geometric specifications (e.g., the density of active sites). Finally, external conditions, for example, electrolyte-related values such as proton concentration and conductivity, might have changed, whereas the model equations and parameters remain valid. To evaluate if the experimentally observed degradation can be attributed to a change in mechanism, kinetics, or electrolyte, it was checked if adjusting certain sets of parameters of the pristine system allows to fully reproduce the experimental CV data of the degrading system. If reproduction is possible, the mechanism is valid, and changes in performance can be attributed to kinetics, geometry, or electrolyte, depending on the affected parameters.
For the analysis, different combinations of parameters were changed, and the resulting rmse were monitored, as shown in Figure 4.11. Experimental CV data shown in Figure 4.2 in between applying a potential of 1.6 V vs RHE are used for evaluation. Adjusting the density of active sites alone or in combination with the resistance or electrolyte concentration did not allow to explain the experimentally observed degradation behavior. Nevertheless, in all the following analyses, the density of active sites is also adjusted to account for the known and likely degradation effects of material dissolution[110], particle detachment[131], particle cracking, and loss of binder material[132]. The changes in proton concentration, electrolyte resistance, and double-layer capacitance are individually evaluated, and the maximum rmse values of 0.33, 0.18, and 0.26 mA cm^{-2} are gained, respectively, in Figure 4.11a to 4.11c. Although the change in electrolyte resistance is evaluated with the lowest rmse so far, a maximum parameter value of R = 392 Ω is required to describe the completely degraded system, which is in contrast to the experimentally observed 18.2 Ω. Due to the high discrepancies, any correlation between the electrolyte-related parameters and the degradation behavior is disproved. By analyzing both cases of changing the electrolyte resistance and double-layer capacitance, the simulated behaviors do not match with

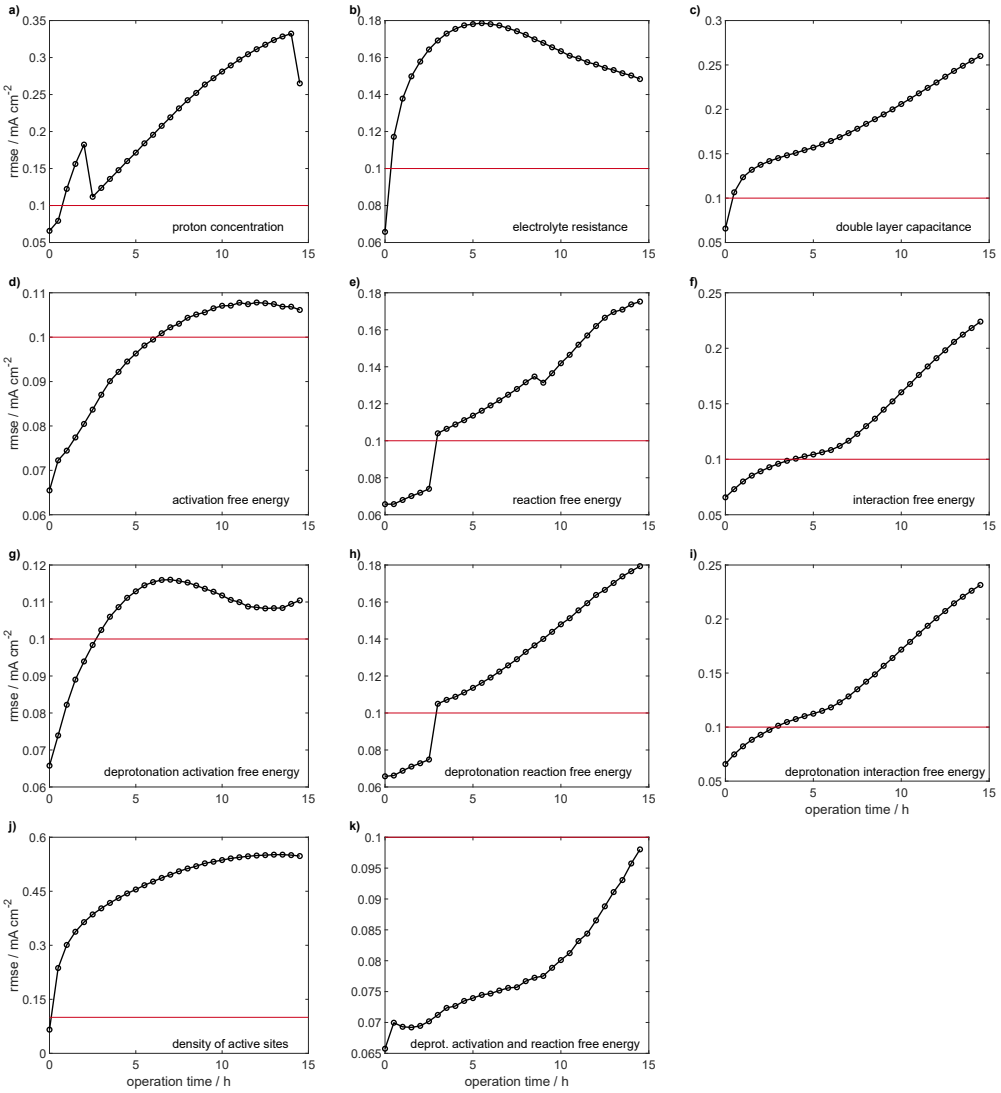

Figure 4.11: The resulting rmse estimators for the parameterization process of the CV curves during system degradation are evaluated with different optimized sets of parameters noted in the bottom right of each graph. The red line defines the threshold under which the best results were gained. Please note the different scaling of the vertical axis.

experimental observation. Thus, degradation is not related to a change in the electrolyte properties.

The free energy parameters are analyzed with the same method, and the results are shown in Figures 4.11d to 4.11i. Low values of the rmse and, thus, good reproduction of the experimental behavior are gained by optimizing all activation free energy values in Figure 4.11d. The activation free energy was found to be the best descriptor for the degradation process with a maximum rmse value not exceeding 0.11 mA cm^{-2}, which is significantly lower compared to the error values of 0.18 mA cm^{-2} for the reaction energy in Figure 4.11e and 0.22 mA cm^{-2} for the interaction free energies in Figure 4.11f, respectively. Optimizing only activation free energies of the deprotonation steps hardly increase the rmse in Figure 4.11g. Also, the change of the reaction energy in Figure 4.11h or the interaction energy in Figure 4.11i of only deprotonation steps gives comparable rmse values with a change in all steps. Evaluated with a high rmse value of up to 0.55 mA cm^{-2} in Figure 4.11j, the change in the density of active sites is not able to explain the experimentally observed degradation behavior solely. Best reproduction is obtained by the optimization of the activation and reaction free energies of the deprotonation steps, evaluated with a rmse remaining for each evaluated timestep below the 0.1 mA cm^{-2} threshold in Figure 4.11k. The simulation results and identified parameter values of this case are shown in Figure 4.12.

The activation free energy was found to be the best descriptor for the degradation process, whereas changing only the reaction and the interaction free energies showed significantly higher deviations from experiments. Reducing the full set of energy parameters to only deprotonation-related parameters was found to hardly increase the errors, which indicates that deprotonation processes are significantly impacted by catalyst degradation. On this knowledge base, a combination of parameters, including the density of active sites and activation and reaction free energies of the deprotonation processes, was evaluated. The reproducibility was drastically improved and led to excellent reproduction of the experimental CV. The simulated cyclic voltammograms in Figure 4.12a present all experimentally observed degradation features: the drastic decrease in OER current density, the slight absolute increase in redox transition currents, and the shift of anodic peak position toward higher and cathodic peak position toward lower potentials. The parameters which changed and are consequently responsible for replicating the degrading CV performance can be individually assessed. The density of active sites increases up to 20 % after 8 h of operation, as shown in Figure 4.12b. The significant increase is most likely attributed to a loss of binder material, which leads to faster exposure of active material than dissolution[110] of active material. A decrease of active material provoked by dissolution is, thus, excluded from beeing responsible for the observed performance decrease of the catalyst. The reaction free energies of all four deprotonation steps reveal only minor changes below 0.04 eV of the value for the pristine material in Figure 4.12c, which corresponds to < 2.8 % relative changes. The most significant changes are exhibited in Figure 4.12d with the changes in activation free energies of all four deprotonation steps. There is a clear correlation between time of degradation and activation free energy. After a fast increase during the first hours, a linear increase in activation energies

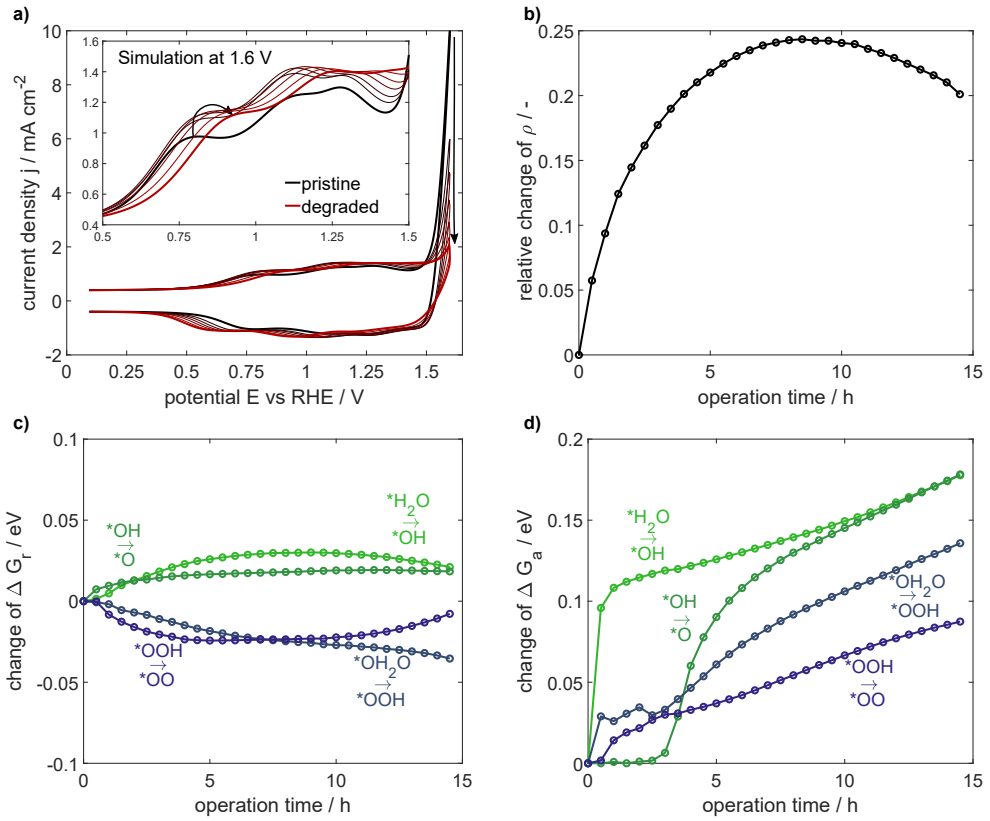

Figure 4.12: Simulation of the effect of degradation of Ir oxide catalyst during 15 h of operation at 1.6 V. a) Changes in the cyclic voltammograms from pristine (black) to degraded (red) correspond to the states after operation for each 150 min, b) relative change of site density and changes in c) free reaction energies, and d) activation energies.

is observed for all four activation energy parameters; slopes are similar for all four steps. This observation of changes in electrocatalytic material properties corresponds well to an experimentally reported partially reversible formation of oxygen vacancies during degradation, which was reported to occur on rutile IrO_2 nanoparticles under constant potential operation at 1.6 V.[104] Two likely pathways were proposed and shown in Figure 4.13.

One possibility would be the formation of a lattice oxygen vacancy by saturating a vacant CUS site * to form *O. In the second proposed pathway, molecular O_2 is formed by combining oxygen from the already *O-occupied site with a lattice oxygen atom. As in the present study, high coverage of *O is observed at such high potentials, the observed degradation is attributed to the formation of oxygen vacancies by combining oxygen from the *O-covered site with a lattice oxygen atom to form molecular O_2. As the formation rate of the oxygen vacancies is rather slow compared to the overall OER rate, the results at high potential are insufficient to prove

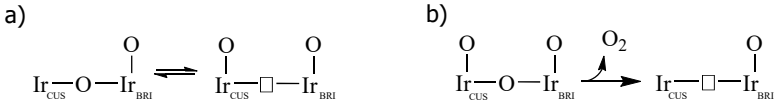

Figure 4.13: Proposed pathways of the vacancy formation on the IrO_2 surface a) from the free * CUS site and b) by the formation of molecular oxygen from the oxygen atom of the *O species with a near-surface atom. The bridge Ir site is denoted with BRI.

that formation via the free surface species * is negligible. However, as no significant amount of degradation is seen at a low potential, where free sites * are prevalent, and as degradation monotonically correlates to potential, the degradation is most likely related to the *O-covered sites, which are prevalent at high potentials. The amount of one of the species being present at the surface does not correlate with the formation of oxygen vacancies, but higher potentials do. The oxygen vacancy formation process and, thus, the degradation are identified as potential-driven.
Major conclusions can be drawn from the above-given analysis. First, the assumed mechanism is able to describe the electrocatalytic behavior not only on the pristine IrO_2 catalyst but also on all transient states during the long-term aging test. Furthermore, the observed loss in electrocatalytic activity is correlated with a catalyst-related degradation process. This was correlated here to the significant increase in the density of active sites and the activation free energy of deprotonation steps. After several hours of degradation, the change in activation free energy of the elementary deprotonation steps is identified to correlate linearly with time and with the formation of oxygen vacancies[104] during the degradation process.

4.4 Concluding Remarks

A microkinetic model of the oxygen evolution reaction on IrO_2 nanoparticles was presented, which elucidates performance limitations by single surface processes and the impact of catalyst degradation on surface processes occurring during OER. In contrast to state-of-the-art approaches, a comprehensive description of the kinetics, thermodynamics, and their changes due to degradation was identified by the use of experimental data. Electrocatalyst-related parameters, such as thermodynamic energies and the density of active sites, were analyzed, and an in-depth understanding of the dynamic formation of surface species was given.
The identified microkinetic model was shown to be highly robust, as it reproduces experimental cyclic voltammograms at various potential scan rates and polarization curves and shows similar trends to X-ray spectroscopic methods. Moreover, the identified free energy values are predominantly in the range of reported values by DFT studies. In contrast to DFT calculations, the parameters were determined experimentally. The model provided a deep insight into not only thermodynamics but also kinetic limitations. In contrast to kinetic modeling methods relying on

steady-state or quasi-equilibrium assumptions, the presented dynamic model enabled resolving the microkinetic quantities of individual elementary processes. Furthermore, the method was shown to be highly effective in studying the decrease of catalyst performance in-depth by reproducing experimental degradation. It is thus a highly attractive, complementary method for kinetic and degradation analysis.

Analysis of the simulated reaction rates and surface coverages of adsorbed species indicate three main limitations during the OER: (i) low water adsorption ($^*O + {}^*H_2O \rightleftharpoons {}^*OH_2O$) leads to an accumulation of $^*O$ species. (ii) The third deprotonation step ($^*OOH \rightleftharpoons {}^*OO + H^+ + e^-$) is identified as the potential determining step due to the high reaction free energy. (iii) A notable activation energy barrier limits the oxygen detachment ($^*O \rightarrow {}^* + O_2$). Regarding the search for a catalyst with better performance, it can be suggested to focus on active sites that not only catalyze the electrochemical deprotonation but also facilitate the water adsorption and oxygen detachment steps.

Further, analysis of degradation-related changes in CV revealed a catalyst-related loss in activity. The assumed reaction mechanism can also reproduce degraded catalyst behavior and, thus, remains valid for the degraded state as well. The identified change in the parameters demonstrates that the degradation is correlated to a nonlinear increase and a subsequent slower linear increase in the activation free energy of the deprotonation steps. In the study, the main reason for the loss in activity is identified as a material-related change, which is correlated to the formation of oxygen vacancies on $^*O$ sites.

Future efforts to develop stable electrocatalytic materials may focus on understanding their degradation process and elaborate strategies to reduce its impact. The present study provides insights even into the thermodynamics and kinetics on a long timescale. It demonstrates that microkinetic modeling is a viable method to understand electrocatalytic surface processes even for degrading material states. The methodology is not limited to OER on rutile IrO_2; the studies in the following chapter 5 indicate its applicability to other OER catalysts, such as the highly active RuO_2 and mixtures of both. The mixtures are of special interest, as they provide the benefits from both transition metal oxides, high stability and high activity.

5 Microkinetic Barriers of the Oxygen Evolution on the Oxides of Iridium, Ruthenium and their Binary Mixtures[7]

5.1 Introduction

In contrast to the last chapters, which primarily investigate Ir-based materials, the study presented here focuses on Ru-based catalysts. Rutile-structured RuO_2 offers record activity amongst various oxides for catalyzing the OER in acidic media.[10, 41–43] It outperforms IrO_2 in terms of a low overpotential, but its stability is modest due to a dissolution rate of 300 pg cm^{-2} s^{-1}, which is 100 times higher compared to its competitor IrO_2.[12] Although this drawback prevents its widespread use in commercial PEM systems, the catalyst is an excellent model system for studying the relationships between material properties and high OER performance.

To increase the electrocatalytic activity of the OER and reduce the amount of the very scarce and, thus, expensive iridium, binary oxide mixtures containing various transition metals were investigated.[7, 10, 11, 133] So far, the most promising catalyst results from the combination of Ir and Ru oxide, as it benefits from both the high OER activity found for RuO_2 and the high stability of IrO_2.[12, 15] Rutile-structured nanoparticles[110, 134], as well as sputtered films[135] of $Ir_xRu_{1-x}O_2$ mixtures, show increasing activity with higher Ru content, while electrocatalytic stability is highest at a relative Ir content of 0.2 when an intermittent current is applied in acidic electrolyte.[135]

The high electrocatalytic activity of single transition metal oxides is explained by complex catalytic processes: the overall OER proceeds in multiple consecutive steps in which the catalyst surface provides active sites to form adsorbed but reactive intermediate species. According to

[7] Parts of this chapter have been published in the following articles:
[2] **Geppert, J.**; Röse, P.; Pauer, S.; Krewer, U. *ChemElectroChem* **2022**, *10*, e202200481.
[110] Escalera-López, D.; Czioska, S.; **Geppert, J.**; Boubnov, A.; Röse, P.; Saraçi, E.; Krewer, U., Grunwaldt, J.-D.; Cherevko, S. *ACS Catal.* **2021**, *11*, 9300-9316.
Results that did not originate from the work of the author of this dissertation are marked accordingly.

DFT studies on the OER on IrO_2[17, 44] and RuO_2[17, 22], several species, such as $^*O$, $^*OH$, and $^*OOH$, are thermodynamically favorable. They are produced by the adsorption of water and subsequent deprotonation.

It is crucial to quantify the kinetics of all reaction steps individually to understand the overall performance of the electrocatalytic OER. This allows for analysis of the major process limitations in order to provide suggestions to optimize the catalysts further.

Thermodynamic binding energies of adsorbed OER intermediate species are reported for the single rutile structured transition metal oxides IrO_2 and RuO_2 and indicate the following process limitations: due to its high reaction energy, the formation of the $^*OOH$ species on the CUS of the (110) RuO_2 surface is reported to determine the potential of the overall process.[17, 45] In contrast, on the IrO_2 active site, the reaction energy of the $^*OOH$ formation is significantly smaller, and the subsequent deprotonation step is potential-determining as this step is thermodynamically less favorable.[1, 44] In the previous microkinetic modeling study in chapter 4, further kinetic limitations of the OER on rutile IrO_2 are identified by slow water adsorption on the $^*O$ species and the oxygen detachment,[1] which confirms DFT-based findings.[47] Such kinetic limitations have not yet been explicitly quantified for the RuO_2 material.

Despite the progress in the field, less effort was made to analyze the mechanism and kinetics of binary Iridium-Ruthenium oxide mixtures. It is known that they form well-mixed bulk structures[136, 137] as the bulk formation energy gets lowered.[138] The surface processes under OER conditions, however, are rarely studied. In a recent study by Reksten et al., lumped kinetic equations were derived for analyzing various options for limiting steps at combined Ir-Ru active sites.[139] By parameterizing the equations with experimental steady-state polarization curves, the deprotonation of the $^*OH$ species was identified as a rate-limiting step.[139] However, further studies showed that good agreement with the experimental polarization data might be insufficient for reliable kinetic identification. This was pointed out in microkinetic studies, in which different sets of parameters and, thus, limiting steps were able to reproduce the same polarization curve of the general OER.[24, 25] Also, the assumption of a combined active site contradicts DFT-based findings of distinguishable Ru and Ir active sites. It was predicted that the CUS consists of either Ir or Ru surface atoms and that they show composition-dependent binding energies for $^*O$, $^*OH$, and $^*OOH$ adsorbed species.[138] This theory was recently supported by experimental CV measurements of deprotonation currents on the binary oxides, which are clearly assigned to either the pure RuO_2 or IrO_2.[110] The finding of the Ir-content-dependent binding energies[138] indicates that transferring the insights from the single transition metal oxides to binary mixtures might not be trivial. However, a significant influence on the OER performance can be expected. This impact of the material mixing on the kinetics of all individual steps in the OER mechanism on distinguishable Ir and Ru active surface sites was, to the best of my knowledge, never been reported so far.

For reliable identification of the kinetic surface processes, the use of dynamic analysis is suggested. It contains more information than analysis under steady state or quasi-equilibrium assumptions, which may lead to multiple solutions, as discussed above.[25] For dynamic analysis, a dynamic microkinetic modeling approach of the complex OER mechanism has shown to be a powerful tool to reproduce and study the interactions during a catalytic process.[1] In addition, the method allows for validating the model and its parameters with dynamic experimental data such as impedance spectroscopy[32, 33] and CV measurements.[3, 27, 28]
Within this chapter, the reaction kinetics and process interactions during the OER on rutile structured Ir-, Ru- and $Ir_xRu_{1-x}O_2$ mixtures are determined and analyzed by employing a microkinetic model approach. A widely accepted OER mechanism from literature provides the basis to formulate the model equations. Parameterization is conducted by comparing the dynamic simulation results to experimental CV curves. With this, thermodynamic parameters such as the free reaction energies and free activation energies of individual process steps are quantified. Theoretical findings on the single transition metal oxides IrO_2 and RuO_2 are not only confirmed experimentally, but also the kinetics of individual process steps during the OER on binary $Ir_xRu_{1-x}O_2$ mixtures are quantified and clarified. In a later section, an in-depth understanding of the performance-limiting reactions and identification of synergetic effects by material mixing will be given.

5.2 Methods

5.2.1 Experimental Characterization

To parameterize the microkinetic model, a proper experimental dataset is required. Here the experimental method is only briefly summarized as it contains steps, which are already described in subsection 4.2.4: rutile structured single crystal nanoparticles, which were produced by flame spray pyrolysis and calcination at 600 °C, had been provided by the Institute for Chemical Technology and Polymer Chemistry at KIT.[8] 2 mg of the material was mixed with 750 µL of deionized water, 250 µL of isopropanol 8.58 µL of Nafion 5 % dispersion (D-520, VWR) and 1.2 µL of 1 M KOH. 10 µL of the resulting ink was drop-casted onto in a glassy carbon working electrode with a geometric area of A = 0.1963 cm^2. The electrode with the pristine particles was put into the PTFE cell filled with 0.1 M H_2SO_4 electrolyte solution together with a Pt wire as a counter electrode and a HydroFlex reversible hydrogen electrode from Gaskatel GmbH. Using a Gamry Reference 600+ potentiostat, impedance spectroscopy measurements at open circuit potential with frequencies from $f = 10^{-1}$ to $f = 10^5$ Hz and a perturbation amplitude of $E = 10$ mV as well as three consecutive CV curves in between potentials of $E = 0.05$ and 1.6 V were recorded

[8] Production of the particles was done by S. Czioska.

with different potential rates of dE/dt = {200, 100, 50, 25, 200} mV s^{-1}. The potential was corrected afterward by the Ohmic resistances gained from the impedance spectroscopy analyses. The consideration of data over such a wide potential range is important due to the fact that the faradaic current of only the OER itself provides little information for parameter identification as multiple processes contribute here to the overall current simultaneously.[25] Aiming for better process discrimination, the careful analysis of the potential region prior to the OER allows for gaining essential kinetic information about the reactions proceeding here as well.

5.2.2 The OER Mechanism on Rutile Oxides

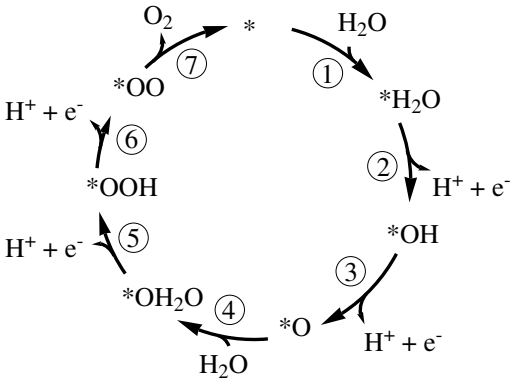

Figure 5.1: Adsorbate evolution mechanism of the OER. The catalyst active site is denoted with an asterisk *.

For modeling the processes at the catalytic surface, the adsorbate evolving mechanism is assumed to take place, as it is widely agreed on in literature for IrO_2,[44] RuO_2[45], and even for their mixtures[138, 139]. It is shown in Figure 5.1 and consists of water adsorbing on the active site, denoted with *, in equations 5.1 and 5.4, producing $^*H_2O$ and $^*OH_2O$, respectively. Via deprotonation in equations 5.2, 5.3, 5.5, and 5.6, several respective intermediate species $^*OH$, $^*O$, $^*OOH$, and $^*OO$ are formed and adsorbed O_2 is detached in equation 5.7, resulting in the final product of molecular oxygen.

5.2.3 Model Equations and Parameterization

To simulate the dynamic changes during a CV, the equations for the time dependent potential in equation 2.24 and the reaction rates in equation 2.18 are used. The surface coverages θ_j by a void or adsorbed species $j \in \Omega_{\text{sur}} = \{^*; ^*H_2O; ^*OH; ^*O; ^*OH_2O; ^*OOH; ^*OO\}$ are defined, so they sum up to unity $x \cdot \sum \theta_j^{\text{Ir}} + (1-x) \cdot \sum \theta_j^{\text{Ru}} = 1$, and the activities a_j of all electrolyte

species $j \in \Omega_{el} = \{H^+; H_2O; O_2\}$ are set constant as given by the experimental conditions. The matrix of the stoichiometric coefficients $\boldsymbol{\nu}$ of the adsorbed species, the electrolyte species, and the transferred electrons are derived from the mechanism in Figure 5.1 in forward $\boldsymbol{\nu}_+$ and backward direction $\boldsymbol{\nu}_-$. The pre-exponential frequency factor k_0 is set to a constant value for all reactions to avoid over-parameterization, as the experimental data do not allow for determining the frequency factor and the free activation energy independently.[140] Further, the function taking Hill-de-Boer type adsorption into account, as well as the surface species balance and the current balance are implemented as given in equation 2.21, equation 2.22 and equation 2.23, respectively.
The resulting current density j of a cyclically applied potential is compared to experimental current j_{exp} during the CV with the aim of estimating the model parameters, which are the free energies, the density of active sites, and the double-layer capacitance. For best estimation, the root mean squared error in equation 3.16 is minimized by two optimization algorithms: 10^6 sets of randomly defined parameter values are simulated. The 20 sets of parameters resulting in the lowest rmse are further optimized by the MATLAB build-in pattern search algorithm, each with a total of 98,000 objective function iterations. For the reaction free energy parameters of the single transition metal oxides RuO_2 and IrO_2, and the binary mixtures, a profile rmse analysis with deviations of {(-0.2); -0.1; -0.05; 0; 0.05; 0.1; (0.2)} eV was conducted with 25,000 objective function iterations. This is used in the same way as the profile likelihood method is used to check for parameter identifiability.[141]

5.3 Results and Discussion

In the following sections, a detailed kinetic and thermodynamic analysis of the single transition metal oxides RuO_2 and IrO_2, as well as the binary mixtures $Ir_xRu_{1-x}O_2$, is given. First, the experimental findings of the CV measurements are presented, and the influence of atomic material composition on the OER activity is investigated. An in-depth and qualitative analysis and discussion of the microkinetics and the thermodynamic energies of single adsorption steps on the single transition metal oxides RuO_2 and IrO_2 will be provided in the second section. The results were gained from the model-based analysis method. In short, the model equations were derived based on an OER mechanism gained from literature and shown in Figure 5.1. The reaction rates were considered in the forward and backward directions for chemical and electrochemical processes at the active sites. This allows for dynamic simulations and the identification of the kinetic and thermodynamic properties by comparison to experimental CV curves. After the analysis of the single transition metal oxides, the microkinetics at $Ir_xRu_{1-x}O_2$ mixtures will be reported and discussed in detail, as well as the effect of material mixing on the OER performance.

5.3.1 Experimental Dynamic Current Response

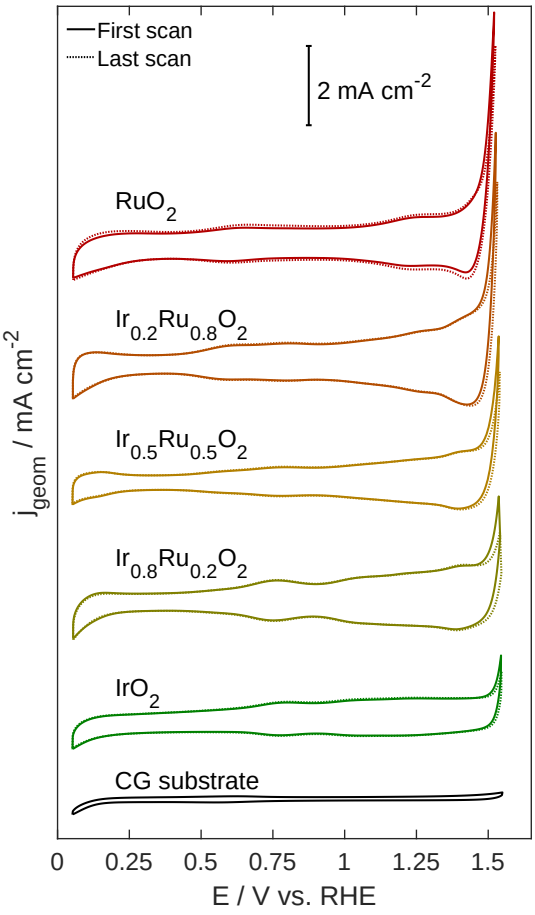

Figure 5.2: Experimental CV curves of RuO_2 (red), IrO_2 (green), and binary mixtures of $Ir_xRu_{1-x}O_2$ nanoparticulated catalysts in a 0.1 M H_2SO_4 solution at room temperature and a scan rate of 200 mV s^{-1}. The third cycle of the first measured scan is shown with a solid line, and the third cycle of the last scan was measured after a series of three scans with five different scan rates to determine the stability of the materials and shown with a dashed line. A reference measurement with the glassy carbon substrate is shown in black.

The cyclic voltammograms of all nanoparticles as well as a reference measurement of the glassy carbon substrate, are shown in Figure 5.2. The effect of the nanoparticles is clearly observable as the respective current responses differ significantly from the measurement with the substrate

only. On RuO_2, three broad redox transitions are visible at potentials of 0.66, 1.23, and 1.43 V. Also, three redox transitions can be detected on IrO_2 but at different potentials of 0.79. 1.12 and 1.3 V. The features correlate with the oxidation of the active sites or of already adsorbed species by deprotonation steps.[22, 142–144] Interestingly, such redox transitions are also found at similar potentials in the measurements of the binary mixed oxides. The findings indicate that on the surface of the mixtures, both Ir and Ru active sites are active and define their electrochemical properties. The magnitude of the current density on the specific potentials, which is associated with processes on the Ir and Ru sites, changes in qualitative accordance with the material compositions. This is additional evidence of the presence of individual active Ir and Ru sites.

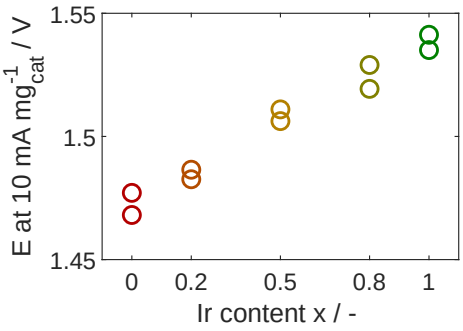

Figure 5.3: Experimentally observed OER potential at a catalyst mass normalized current of 10 mA $mg^{-1}{}_{cat}$. Each circle indicates an independent measurement.

The third cycles of both the first and the last scan in Figure 5.2 differ only insignificantly. This leads to the conclusion of a stable state of electrodes during the measurement time of about 15 minutes, which allows for a valid analysis of the OER activity. The current density at the highest measured potential of 1.55 V is the highest for the RuO_2 sample and, thus, shows the highest OER turnover frequency. The OER overpotentials are quantified at a mass-normalized current density value of 10 mA mg_{cat}^{-1} to provide a better comparison of the activity between the samples. The resulting values of two independent measurements are given in Figure 5.3. A linear trend of an increasing overpotential with higher Ir content is observed, which is in accordance with the literature.[15, 135, 145] This shows a distinct connection between the material and structural specification and the activity of the OER. With the aim to provide insights into the kinetics and thermodynamics of the electrochemical processes on the surface of the different materials, a model-based analysis will be given in the following sections.

5.3.2 Kinetic Analysis of the OER at RuO_2 and IrO_2

For the following model-based analysis, high model validity is key to providing accurate and trustworthy results. With a three-step parameter estimation algorithm, which contains global and local optimization as well as a check for parameter identifiability, the main process of defining parameter values was carefully conducted. Excellent agreement between the experimental CV results and the dynamic simulation data is shown for the OER on RuO_2 in Figure 5.4a and on IrO_2 in Figure 5.4b. The experimentally observed features for RuO_2 and IrO_2 are reproduced well by the models, and both simulations show low rmse of 0.024 and 0.069 mA cm^{-2}, respectively. Even when applying different potential scan rates, good reproducibility is achieved, as shown in the appendix in Figure A.4. The high identifiability of the free reaction energy parameters is visible from rmse profile analysis shown in the appendix in Figure A.2 and A.3. In conclusion, a valid model with identified parameters is gained, which shows trustworthy results due to its excellent reproduction of experimental data.

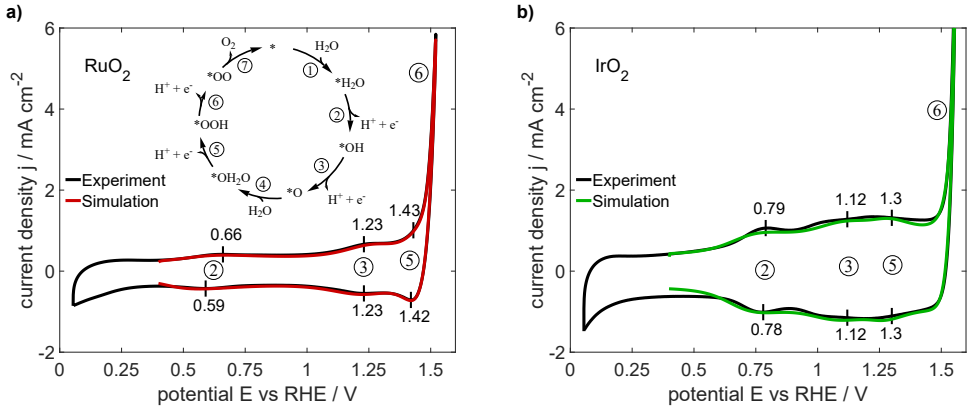

Figure 5.4: Experimental and simulated CV curves a) on RuO_2 and b) on IrO_2 nanoparticulated catalysts in a 0.1 M H_2SO_4 solution at room temperature and a scan rate of 200 mV s^{-1}. The numbers in the figures correspond to the reaction steps of the reaction mechanism shown in the inset.

The assumed mechanism in Figure 5.1 and the corresponding kinetics are thus a valid choice to reproduce the dynamic electrochemical behavior on both catalysts. In order to elucidate the kinetic limitations at RuO_2 and compare them to the kinetics at IrO_2, the seven reaction steps in equations 5.1 to 5.7 can now be analyzed individually over a wide potential range. The model parameters to describe the processes on IrO_2 are already given in the last chapter in Table 4.1 and are discussed in section 4.3.2. The sets of the estimated parameters for the reaction free energies, the activation free energies, and the interaction free energies of the RuO_2 catalyst are given in Table 5.1. The values of the reaction free energy are normalized to electrochemical standard conditions, which are defined at room temperature and with the activities of all substances at

Table 5.1: Values for the reaction free energy, the activation free energy, and the reactant species interaction energy of reaction steps 1 to 7 on RuO_2 identified by reproducing CV with the microkinetic model.

step	ΔG_r^0 / eV	ΔG_a / eV	ΔG_{int} / eV
1	0.25	0.19	0
2	0.51	0.10	0.20
3	1.28	0	0.13
4	0.39	0.09	0.06
5	1.44	0	0.20
6	1.37	0.0.	0.20
7	-0.32	0.34	0.19

unity. Note that, unless specified, the values are given at 0 V. Further identified parameters on the RuO_2 material are the double-layer capacitance of C_{dl} = 11.05 F m^{-2} and the density of active sites of $\rho = 0.65 \cdot 10^{-4}$ mol m^{-2}.
At the lowest simulated potential of 0.4 V, water adsorption takes place:

$$^* + H_2O \overset{r_1}{\rightleftharpoons} {}^*H_2O \tag{5.1}$$

The ratio between the free active site * and adsorbed water is defined by the reaction free reaction energy, which was quantified to $\Delta G_{r,1}^0$ = 0.24 eV on RuO_2 and $\Delta G_{r,1}^0$ = 0.11 eV on IrO_2. Water adsorption is, therefore, thermodynamically unfavorable, whereas kinetic simulation yields a water coverage of 10.4 % on the RuO_2 surface and 34.8 % on the IrO_2 surface. The high amount of free active sites on RuO_2 is also known from near ambient pressure X-ray photoelectron spectroscopy on RuO_2.[146] An increase in potential above 0.4 V starts the electrochemically driven deprotonation of adsorbed water, given in equation 5.2.

$$^*H_2O \overset{r_2}{\rightleftharpoons} {}^*OH + H^+ + e^- \tag{5.2}$$

The reaction free energy values of $\Delta G_{r,2}^0$ = 0.51 eV on RuO_2 and $\Delta G_{r,2}^0$ = 0.73 eV on IrO_2 correlate with the potentials of the first redox transitions in Figure 5.4. Deviations from the noted potential values arise due to the preceding slow water adsorption. The small but notable value of the activation free energy for this process on RuO_2 of $\Delta G_{a,2}$ = 0.1 eV is in good agreement with the shift in the absolute cathodic to anodic peak maxima observed in the experimental CV. On IrO_2, rather no shift is observed between cathodic and anodic absolute peak maxima of the experimental redox transition; this corresponds to an activation energy of $\Delta G_{r,2}$ = 0 eV. Comparably low activation barriers of deprotonation steps were also reported in a DFT study, in which

die authors explain this finding by the short traveling distance of the proton from the surface oxygen to the water molecule in the electrolyte.[112] A further increase in potential initiates the second deprotonation step, the deprotonation of *OH, in equation 5.3.

$$^{*}\mathrm{OH} \overset{r_3}{\rightleftharpoons} {}^{*}\mathrm{O} + \mathrm{H}^{+} + \mathrm{e}^{-} \tag{5.3}$$

Mayor differences are observed in the potential and the reaction free energy parameters of this redox transition between both materials. On RuO_2, the process starts at a higher potential, which corresponds to a higher reaction free energy of $\Delta G^0_{\mathrm{r},3}$ = 1.28 eV on RuO_2 than $\Delta G^0_{\mathrm{r},3}$ = 1.12 eV on IrO_2. In comparison to DFT-based calculations,[111] the estimation for the reaction free energy on RuO_2 is in good accordance, but the value on IrO_2 is slightly lower.
The subsequent step is the second water adsorption:

$$^{*}\mathrm{O} + \mathrm{H_2O} \overset{r_4}{\rightleftharpoons} {}^{*}\mathrm{OH_2O} \tag{5.4}$$

On both catalysts, this chemical reaction requires high reaction energies of $\Delta G^0_{\mathrm{r},4}$ = 0.39 eV on RuO_2 and $\Delta G^0_{\mathrm{r},4}$ = 0.54 eV on IrO_2. This finding is qualitatively in good agreement with reported DFT results for RuO_2[141] and IrO_2[47]. This reaction energy does not only influence the lower potential region. It also has a significant impact on the OER performance at potentials above 1.5 V. Figure 5.5a shows the free energies of all reaction steps on RuO_2 and IrO_2 corrected to the standard redox potential of the OER of 1.23 V. It is clearly visible, that the second water adsorption in step 4 possesses the largest free energy of all steps. In consequence, this step limits the overall process chemically and causes a high accumulation of the reactant species on the surface, as shown in the appendix in Figures A.6 and A.7 on the Ru and the Ir active site, respectively. Adsorbed atomic oxygen, *O, is dominant even at the highest simulated potentials of 1.55 V and 1.6 V, at which the OER is typically performed. This proves that the chemical adsorption of water limits the overall OER rate. The third deprotonation step in equation 5.5

$$^{*}\mathrm{OH_2O} \overset{r_5}{\rightleftharpoons} {}^{*}\mathrm{OOH} + \mathrm{H}^{+} + \mathrm{e}^{-} \tag{5.5}$$

occurs on RuO_2 directly at the onset of the exponential increase of the OER, which has the overall highest value in reaction free energy of $\Delta G^0_{\mathrm{r},5}$ = 1.44 eV. Hence, it describes the potential determining step of the OER. As shown in the energy diagram in Figure 5.5b, an applied potential of 1.44 V is required to reach equilibrium conditions for this process step. On IrO_2, in contrast, the energy is lower with a value of $\Delta G^0_{\mathrm{r},5}$ = 1.23 eV, and, thus, the reaction takes place at potentials lower than the actual OER onset. The reaction free energy of the fourth deprotonation step

$$^{*}\mathrm{OOH} \overset{r_6}{\rightleftharpoons} {}^{*}\mathrm{OO} + \mathrm{H}^{+} + \mathrm{e}^{-} \tag{5.6}$$

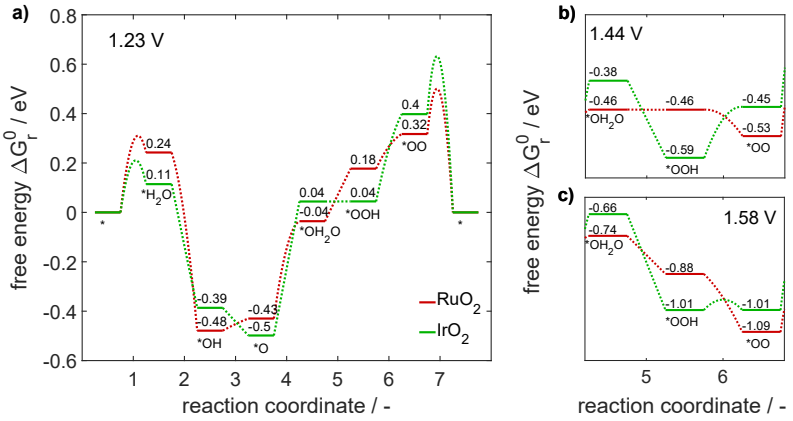

Figure 5.5: Energy diagrams along the reaction coordinate of the OER mechanism are given in Figure 5.1 on RuO_2 (red) and on IrO_2 (green). The potential dependent reaction free energy values are denoted in full lines, and the activation free energy barriers are in dotted lines. Values are given at electrochemical standard conditions (room temperature and the activities of all substances at unity) and different potentials of a) 1.23 V, b) 1.44 V, and c) 1.58 V.

on RuO_2 $\Delta G^0_{r,6}$ = 1.37 eV is smaller than the value from the previous step and is, thus, not the potential limiting step. However, on IrO_2, this step is crucial. With a reaction free energy value of $\Delta G^0_{r,6}$ = 1.58 eV as the overall maximum, it represents the potential determining step. According to the energy diagram in Figure 5.5c, the thermodynamic equilibrium is reached at an applied potential of 1.58 V. The final step of the OER reaction mechanism marks the oxygen detachment given in equation 5.7.

$$^*\mathrm{OO} \xrightarrow{r_7} {}^* + \mathrm{O_2} \tag{5.7}$$

The chemical process is thermodynamically favorable due to negative reaction free energies of $\Delta G^0_{r,7}$ = -0.32 eV on RuO_2 and $\Delta G^0_{r,7}$ = -0.40 eV on IrO_2, suggesting a fast reaction. Yet, the step faces a strong kinetic barrier. In contrast to the previous reaction steps, very high activation free energies of $\Delta G_{a,7}$ = 0.34 eV on RuO_2 and $\Delta G_{a,7}$ = 0.43 eV on IrO_2 are quantified for the oxygen release, which is in qualitative agreement with DFT-based findings on IrO_2 of ΔG_a = 0.58 eV.[47] These activation barriers not only limit the overall OER process but also lead to an accumulation of the reactant species *OO on the Ru and the Ir active site, as shown in the appendix in Figure A.6 and A.6, respectively.

In conclusion, the OER performance is constrained by three steps on each catalyst material: a chemical limitation by water adsorption on *O in equation 5.4, the potential defining deprotonation of $^*OH_2O$ on RuO_2 in equation 5.5 and of *OOH on IrO_2 in equation 5.6. Finally, a kinetic limitation of the oxygen detachment in equation 5.7 is observed and explained by the high activation energy. Although the mechanism is identical on both materials, the catalytic activity is

especially defined by the energy values of the respective potential determining steps. As those steps are different, it is analyzed in the following, how the processes interact when mixing the materials.

5.3.3 Kinetic Analysis of the OER at Oxide Mixtures of $Ir_xRu_{1-x}O_2$

Binary mixtures of transition metal oxides may inherit characteristics from both materials. Ideally, this can lead to improved overall properties. For example, the binary mixtures of RuO_2 and IrO_2 provide lowered bulk formation energy[138] and are, thus, more stable than pure RuO_2[110]. They further show increased OER activity in comparison to the single metal oxide IrO_2.[110] In the following, the OER kinetics on $Ir_xRu_{1-x}O_2$ mixtures are analyzed in order to understand the interactions and processes on the active sites and surface species, which lead to the observed increase in OER performance.

For the kinetic analysis of the binary transition metal oxides $Ir_xRu_{1-x}O_2$, separate active sites consisting of Ru and Ir, are assumed as found by DFT calculations[138] and in dynamic CV experiments[110]. In consequence, the OER mechanism, including all the adsorption, desorption, and deprotonation steps shown in Figure 5.1, is assumed to proceed on both active sites independently. In the first step, the energy parameter values quantified for RuO_2 and IrO_2 were used for the simulation. In addition, the relative Ir content x and the density of active sites were parameterized in order to minimize the deviation from experimental data. The experimental and simulated CV curves are given in the appendix in Figure A.5. A clear discrepancy between the experimental and simulated current density is observable between 1.3 V and 1.5 V. This results in deviations that are higher than for the single oxides and indicate that the kinetics of at least one reaction step is not reproduced correctly by the parameters from the single oxides. Mixing the material causes, thus, interactions, which possibly have a synergetic effect on the activity and will be analyzed in the following.

To evaluate whether a change in energy parameters without modification of the OER mechanism allows for properly describing the experimentally observed behavior of the mixtures, the parameters were newly identified by using the parameters from RuO_2 and IrO_2 as initial values for the Ru and Ir active sites, respectively. The assumption of different energy values is in full agreement with DFT calculations, which suggested a change in the binding energy of adsorbed species with different relative Ir content.[138] Also, the density of active sites, the double-layer capacitance, and the relative content of Ir active sites were identified. A change in the relative Ir content of the surface composition was considered to account for possible deviations between the nominal bulk and the surface.[110] The estimated reaction free energy values are given for both active sits of all mixtures in Table 5.2. The free energy parameters estimated for the activation

and interaction are given in the appendix in Tables A.3 and A.4, respectively, and the values quantified for the density of active sites, the double-layer capacitance, and the relative Ir content are noted in Table A.5. The results of the profile rmse analysis are published in the supporting information in [2]. The resulting simulated CV curves in Figure 5.6 show an excellent agreement with the experimental CV curves for all three binary catalyst mixtures. This confirms that the mechanism still holds but that there exist energetic interactions for the mixtures.

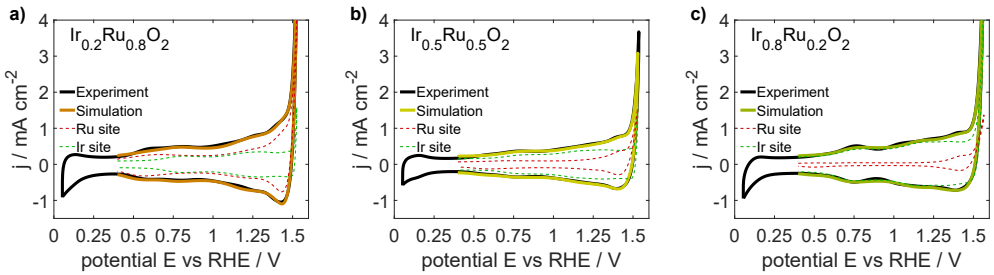

Figure 5.6: Experimental and simulated cyclic voltammetry curves on the binary oxides a) $Ir_{0.2}Ru_{0.8}O_2$, b) $Ir_{0.5}Ru_{0.5}O_2$ and c) $Ir_{0.8}Ru_{0.2}O_2$, with rmse values of 0.033, 0.017, and 0.032 mA cm^{-2}, respectively. The simulations allow for distinguishing between the processes at the Ru and Ir active sites, which results in the current densities given with the dotted red and green lines, respectively. The data was recorded at 200 mV s^{-1} in 0.1 M H_2SO_4 solution at room temperature.

The analysis of the free energy values and the changes of surface coverages with potential in Figure A.6 and A.7 in the appendix reveal similar process limitations for all mixtures as for the previously discussed single oxides: On both Ir and Ru active sites, the water adsorption step in equation 5.4 shows limiting behavior. Also, the oxygen detachment step of Equation 5.7 faces a high, thus kinetically limiting, activation energy. The highest reaction free energy on the Ir active site is obtained for the deprotonation of $^*OOH$ in Equation (5.6) for all mixtures. Moreover, the highest reaction free energy on the Ru active site is identified for the deprotonation of $^*OH_2O$, equation 5.5, for all mixtures with high Ru-content, i.e., $Ir_{0.2}Ru_{0.8}O_2$ and $Ir_{0.5}Ru_{0.5}O_2$. In contrast, for $Ir_{0.8}Ru_{0.2}O_2$, the deprotonation energy of $^*OH_2O$ gets lower, and the deprotonation of $^*OOH$ becomes limiting, similar to the Ir-sites. Since the highest reaction free energy on the Ru active site is lower compared to the value on the Ir site, the mentioned steps on the Ru active site determine the overall potential.

Now, the contribution of Ru and Ir sites to the performance of the CV is analyzed. At $Ir_{0.2}Ru_{0.8}O_2$, the current density shown in Figure 5.6a is strongly impacted by deprotonation on both Ru and Ir active sites. The single processes at Ir and Ru sites occur at similar potentials as on the discussed single oxides; as the potentials differ between RuO_2 and IrO_2, redox transitions at Ir and Ru sites can be distinguished. The large share of Ir to the current in the CV can be explained as follows: Although the nominal relative bulk Ir content is 0.2, the identified relative active site content at the surface is twice this value, with a share of 0.4. Thus, the Ir signal contributes much more than

Table 5.2: Estimated parameter values of the reaction free energies of the surface processes of intermediate species on $Ir_xRu_{1-x}O_2$. Please note that only the adsorbed species are indicated in the reaction equations.

Ir site: ΔG_r^0 **/ eV**	$\mathbf{Ir_{0.2}Ru_{0.8}O_2}$	$\mathbf{Ir_{0.5}Ru_{0.5}O_2}$	$\mathbf{Ir_{0.8}Ru_{0.2}O_2}$
$^* \rightarrow {}^*H_2O$	0.15	0.21	0.16
$^*H_2O \rightarrow {}^*OH$	0.74	0.72	0.71
$^*OH \rightarrow {}^*O$	1.22	1.21	1.18
$^*O \rightarrow {}^*OH_2O$	0.44	0.44	0.44
$^*OH_2O \rightarrow {}^*OOH$	1.27	1.27	1.30
$^*OOH \rightarrow {}^*OO$	1.55	1.57	1.58
$^*OO \rightarrow {}^*$	-0.46	-0.50	-0.45
Ru site: ΔG_r^0 **/ eV**			
$^* \rightarrow {}^*H_2O$	0.22	0.27	0.24
$^*H_2O \rightarrow {}^*OH$	0.51	0.56	0.51
$^*OH \rightarrow {}^*O$	1.26	1.29	1.34
$^*O \rightarrow {}^*OH_2O$	0.35	0.28	0.36
$^*OH_2O \rightarrow {}^*OOH$	1.44	1.40	1.34
$^*OOH \rightarrow {}^*OO$	1.32	1.31	1.37
$^*OO \rightarrow {}^*$	-0.19	-0.19	-0.25

20 % to the CV curves at potentials below OER. Indeed, a similar accumulated Ir content on the surface was also experimentally found by conducting XPS and was explained by the comparably fast dissolution of Ru species in the acidic electrolyte.[12, 110] The experimental values of the XPS characterization[9] in Figure 5.7 are in good accordance with the model results. The accumulation of Ir at the surface can also be seen in the experimental and simulation data of $Ir_{0.5}Ru_{0.5}O_2$ and is less pronounced in the data of $Ir_{0.8}Ru_{0.2}O_2$. Finally, it is interesting to see for $Ir_{0.2}Ru_{0.8}O_2$ a notable difference between current shares in the CV between the adsorption region and the OER region. Whereas currents in the adsorption region below 1.5 V are equally strong on both active sites, the turnover frequency of the OER is mainly defined by the processes at the Ru active sites: Ru sites convert more than two third of the electrons at the highest simulated potential of 1.55 V. Thus, Ru sites are more active during the OER.
In Figure 5.6b, the experimental and simulated cyclic voltammograms of $Ir_{0.5}Ru_{0.5}O_2$ are shown.

[9] XPS characterization was conducted by D. Escalera-López.

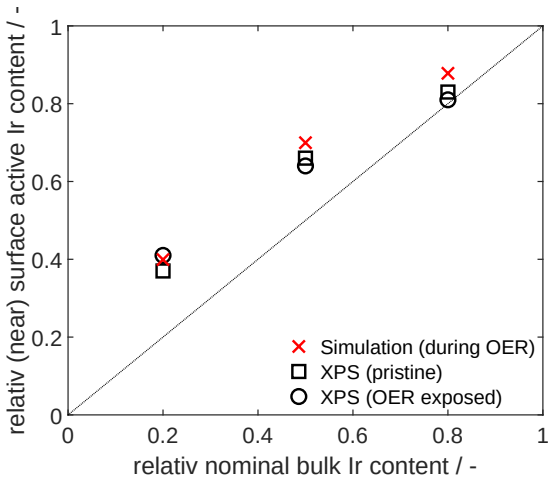

Figure 5.7: Model-based estimation and XPS-measured values of the relative content of Ir active sites on the surface in comparison to the nominal bulk content. The experimental data was gained from Escalera-López et al.[110].

At potentials prior to the oxygen evolution, the main current contribution arises from the deprotonation processes on the Ir active site. Also, here the identified share of active Ir sites on the catalyst surface is 0.7 and thus higher than the bulk value. This observation corresponds to the XPS-measured relative surface Ir content of the same material.[110] As a result, the contribution of the processes on Ir to the overall current in the CV is much higher than at $Ir_{0.2}Ru_{0.8}O_2$. At the OER potential of 1.55 V, the number of electrons that are transferred at all active Ir and Ru sites is roughly the same. This seemingly contradicts thermodynamic expectations, as the reaction energy of the potential determining step on Ir sites, $\Delta G^0_{r,6}$ = 1.57 eV, is higher than on the Ru site with $\Delta G^0_{r,5}$ = 1.40 eV. Yet, it can be well explained by the increased Ir site content and the kinetics, as the share of the surface covered by reactant species differs from of $\theta_{Ru,\,OH_2O} < 0.01$ on the Ru site to $\theta_{Ir,\,OOH} = 0.17$ on the Ir site. Thus, the potential determining step on the Ru site is decelerated due to the low amount of both the reactant species and the active sites.

Finally, the CV curves of the $Ir_{0.8}Ru_{0.2}O_2$ binary oxide and the corresponding partial current densities are given in Figure 5.6b. They show dominating processes at the Ir site over the full potential range due to the fact that the estimated share of Ir active sites given in Figure 5.7 is 0.88. Nevertheless, as the OER processes at 1.55 V, the Ru site still contributes roughly 20 % of the total current density. Thus, the turnover frequency per active site is still higher on the Ru site than on the Ir site.

Having discussed the partial currents in the CV curves on the Ir and Ru active sites, the synergetic effect of material mixing on the potential determining OER steps is now elucidated. An overview of the changes in reaction free energies, which essentially determine the activity of the IrO_2, RuO_2, and their mixed oxides, is shown in Figure 5.8. As previously explained, for

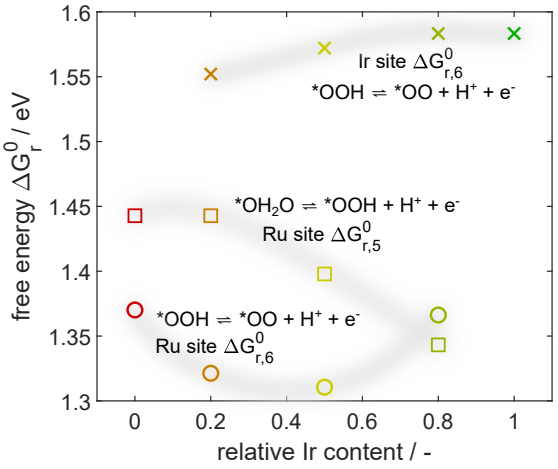

Figure 5.8: Reaction free energy values identified for the potential determining deprotonation steps of the OER on the Ru active site (circle, square) and the Ir active site (x) of RuO_2, IrO_2, and the $Ir_xRu_{1-x}O_2$ mixtures with respect to the nominal relative content of bulk Ir.

Ir-contents until 50 %, the potential determining step of OER on the Ru active site is the deprotonation step ($^*OH_2O \rightleftharpoons {}^*OOH + H^+ + e^-$) given in equation 5.5. In contrast, on the Ir active site, the deprotonation step ($^*OOH \rightleftharpoons {}^*O + H^+ + e^-$) in equation 5.6 was identified as the potential determining step of the reaction. For the energy values, there is a clear trend that applies to both sites: as the content of the dominant active site decreases, the reaction free energy of this site is lowered. Thus, the mixed oxides exhibit a synergetic effect that results in higher OER activity at both individual active sites. On the Ru site, this effect is strongest for the mixed oxides with a relative Ir content of 0.8. On this material, the reaction free energy $\Delta G^0_{r,5}$ = 1.34 eV of the step in equation 5.5 is lowered and undercuts the reaction free energy $\Delta G^0_{r,6}$ = 1.37 eV of the subsequent process in equation 5.6. This results in $^*OOH$ deprotonation becoming the potential determining step on Ru for high Ir contents. Despite the fact of a lowered share of active Ru sites present at the surface, the synergies promoted by the material structure provide overall improved kinetics at both active sites.

This work clearly shows that while the same mechanism holds for the single transition metal oxides and the binary mixtures, the material mixing leads to a decrease in reaction free energies of the potential determining steps and, thus, improved OER performance at both active sites. As the reaction free energies are directly related to the binding energy of adsorbed species, it is shown that these can be tuned by adding other atoms in such a way that higher catalytic activity is achieved. While $Ir_xRu_{1-x}O_2$ is also commercially attractive, it serves as a well-characterized material to study the origin of this effect and a possible correlation to the electronic band structure to gain an in-depth understanding of the active catalyst material. Ir mixing with other materials than Ru lowers the cost and might also provide an increased activity of the Ir active sites. This

prediction might be especially useful for future studies which are aiming for further catalyst development.

5.4 Concluding Remarks

In the presented chapter, an in-depth kinetic analysis of the reactions and adsorption processes and their limitations on Ir and Ru active sites during the OER via a microkinetic model is provided. The kinetic model and the underlying mechanism allow for reproducing CV curves of IrO_2, RuO_2, and their binary mixtures $Ir_xRu_{1-x}O_2$. The surfaces of the binary mixed oxides $Ir_xRu_{1-x}O_2$ show an accumulation of Ir active sites, which exceeds that of the bulk stoichiometry and is in accordance with recent experimental studies. Major findings are that two chemical steps, which are the water adsorption ($^*O + OH_2O \rightleftharpoons {}^*OH_2O$) and the oxygen release ($^*OO \rightarrow {}^* + O_2$), significantly impact the OER on all catalysts. Further, two different deprotonation steps, depending on whether the active site consists of Ru ($^*OH_2O \rightleftharpoons {}^*OOH + H^+ + e^-$) or Ir ($^*OOH \rightleftharpoons {}^*OO + H^+ + e^-$), determine the OER potential at which the OER is conducted. The study reveals that the surface processes of the OER are taking place on both the Ru and the Ir active sites, individually, by quantification of both corresponding current densities. Additionally, a positive synergetic impact on the electrocatalytic activity by mixing the materials is revealed: the thermodynamic reaction free energies of the potential determining steps are lowered for the processes on both the Ru and the Ir active sites. In consequence, not only the presence of the highly active Ru sites provides increased performance, but also the compositional change leads to better Ir site activity. This effect might have a beneficial impact on further mixed oxide catalyst development.

6 Conclusion and Outlook[10]

6.1 Conclusion

This dissertation contributes to understanding the surface processes at Ir- and Ru-based electrocatalysts during the OER. Therefore, microkinetic models were established, validated with dynamic measurements, and employed to analyze the reaction on promising but differently structured catalyst materials. Chapter 2 addressed the first research question: "How can the complex electrocatalytic processes on Ir- and Ru-based anodes be described comprehensively in terms of modeling?" In the context of the principles of electrocatalytic water splitting, well-established findings and fundamental correlations from the literature are presented. Based on this, the set of model equations was derived so that it allows for dynamic simulations that are not restricted by the common quasi-equilibrium or the steady-state approximation.
Furthermore, the effect of parameter variations and the assumption of different adsorption types on the dynamic model output was examined and insight into basic model correlations are given. Based on this analysis, it was concluded that the model allows for a comprehensive description of the electrocatalytic processes by associating reaction kinetics and thermodynamic energies with experimentally observable currents. In addition, this method provides the essential opportunity for parameterization and validation by dynamic experiments such as CV and EIS but also polarization measurements. The ability to correlate simulations directly to experimental data represents a new and significant benefit over the state-of-the-art model approaches commonly used to investigate the kinetics of the OER. In conclusion, this methodology allows for a comprehensive and experimentally validated analysis of electrocatalytic reactions.
The developed model-based methodology was then applied to OER catalysts for the first time to address the second research question: "How do the material structure and composition affect the reaction kinetics of intermediate and product species formation during a dynamic OER

[10] Parts of this chapter have been published in the following articles:
[1] **Geppert, J.**; Röse, P.; Czioska, S.; Escalera-López, D.; Boubnov, A.; Saraçi, E.; Cherevko, S.; Grunwaldt, J.-D.; Krewer, U. *J. Am. Chem. Soc.* **2022**, *144*, 13205-13217.
[2] **Geppert, J.**; Röse, P.; Pauer, S.; Krewer, U. *ChemElectroChem* **2022**, *10*, e202200481.
[3] **Geppert, J.**; Kubannek, F.; Röse, P.; Krewer, U. *Electrochim. Acta* **2021**, *380*, 137902-137914.

operation?" To answer this question, common OER catalysts with different structures and compositions and, thus, electrocatalytic properties were analyzed: the active Ir-based hydrous Ir, the catalytically very stable rutile IrO_2, and the highly active rutile RuO_2, as well as binary mixtures $Ir_xRu_{1-x}O_2$, which exhibit a trade-off between catalytic stability and activity.
In chapter 3, the investigation of the OER on hydrous Ir was conducted. Two proposed mechanisms based on DFT calculations and experimental findings were evaluated. Only the simulation results of the theory-based mechanism could describe and explain the cyclic voltammograms, even at different potential rates. The simulation implies that oxygen is evolving mainly via a fast single-site pathway ($^*OO \rightarrow {}^* + O_2$) with an effective reaction rate that is several orders of magnitude faster than the slow rate of the dual-site ($2\,^*O \rightarrow 2\,^* + O_2$) pathway. Intermediate states of roughly 7 % Ir(III), 25 % Ir(IV), and 63 % Ir(V) are present at typical OER potentials of 1.6 V vs RHE. The kinetic limitation of the water adsorption explains counterintuitive experimental findings of a reduced iridium species Ir(III) during highly oxidizing potentials. Although chemical water adsorption is generally thermodynamically favored, it is kinetically proceeding slower than the electrochemical steps at high overpotentials. In the lower potential range from 0.05 to 1.5 V vs RHE, the stepwise oxidation of the iridium is accompanied by van der Waals ad- and desorption processes. Overall, the analysis shows that the dynamic microkinetic modeling approach is a powerful tool to analyze electrocatalytic microkinetics in-depth and to bridge the gap between thermodynamic calculations and dynamic experiments for the first time quantitatively.
In chapter 4, the anodic benchmark electrocatalyst in PEM water electrolysis, the nanoparticulated rutile-structured IrO_2, was studied at its pristine and OER-degraded state. The dynamic microkinetic model was extended by directly implementing the thermodynamics and validated using cyclic voltammetry at different stages of degradation. Herewith, interactions of individual surface processes were revealed and analyzed. For the pristine catalyst, it was shown that the interaction of three different processes, which are the adsorption of water, one potential-driven deprotonation step, and the detachment of oxygen, limits the overall reaction turnover. During the reaction, the active IrO_2 surface is covered mainly by $^*O$, $^*OOH$, and $^*OO$ adsorbed species with a share, dependent on the applied potential, of 44, 28, and 20 % at an overpotential of 350 mV, respectively. Further, the simulations verify the universal relation of a logarithmic trend in elementary charge with increasing current density and the decrease in oxidation state by increasing the OER operating potential. For the degraded catalysts, it was shown that the loss in electrocatalytic activity during degradation is correlated to an increase in the activation energy of deprotonation processes, whereas reaction energies were marginally affected. As the effect of electrolyte-related parameters does not cause such a decrease, the model-based analysis demonstrates that material changes trigger the performance loss. In combination with results from *operando* XAS, the formation of oxygen vacancies was identified to provoke the material degradation. The insights in this chapter into the degradation of IrO_2 and its effect on the surface processes provide the basis for a deeper understanding of degrading active sites for the optimization of the oxygen evolution performance.

In chapter 5, the highest OER activity of rutile-structured catalysts was analyzed by applying the model-based method to RuO_2. A direct comparison is drawn to the stable benchmark IrO_2 and binary mixtures $Ir_xRu_{1-x}O_2$, which show a trade-off between activity and stability. The surfaces of the oxide mixtures $Ir_xRu_{1-x}O_2$ were found to consist of actives sites of both Ir and Ru. The predicted accumulated amount of Ir compared to the nominal bulk is in accordance with XPS findings. The OER mechanism is processed on both active sites independently and at different overpotentials. It was shown that there is a correlation between performance and the relative Ir content, which can be explained by the reaction free energies of two limiting deprotonation steps. These are, in particular, the formation of the adsorbate species $^*OOH$ on rutile RuO_2 and $^*OO$ on IrO_2. The respective reaction free energies are quantified to 1.44 and 1.58 eV, which are the highest values of the process, thus determining the overpotential. The additional finding of adsorbed oxygen $^*O$ covering > 40 % of the active sites during the OER suggests that subsequent water adsorption is the major performance-limiting step. Finally, a synergetic effect between both active sites on the binary transition metal oxides is identified: the respective other metal lowers the potential determining reaction energy on the Ru or Ir active site. This insight into the surface processes on Ir and Ru binary oxides active sites can be leveraged for further OER catalyst development.
In summary, the microkinetic modeling approach was used to analyze the electrocatalytic OER on common catalysts under dynamic process conditions. While the theoretical analysis of the parameter variation in chapter 2 provides a conformity check, the studies in chapters 3, 4, and 5 confirm that the established model is a viable tool to describe the complex electrocatalytic processes on Ir- and Ru-based anodes. It is therefore considered a direct answer to the first scientific question raised at the beginning of this document. Furthermore, by applying this methodology, the dissertation provides not only an in-depth microkinetic analysis of the OER on various catalysts but also of how structural changes, such as the formation of oxygen vacancies or composition in mixtures, affect reaction kinetics and the formation of intermediate and product species. Therefore, the studies comprehensively describe the answer to the second research question. Overall, the approach based on a microkinetic model is presented, for the first time, as a viable tool to answer current scientific questions about the OER on Ir- and Ru-based anodes.

6.2 Outlook

So far, this dissertation focuses mainly on a small selection of catalytic materials and their in-depth analysis. However, it is well known that production parameters affect the atomic structure and microscopic shape of a catalyst and influence the OER activity. For example, the calcination temperature can easily tune the particle size and crystallinity of Ir oxide nanoparticles. Also, reactive sputtering methods can produce epitaxially grown thin films with a single facet. A

systematic analysis of such physically well-characterized materials would reveal further trends in the reaction kinetics. Such analyses might also be extended to other operating conditions such as different pH, temperature, and pressure and their effect on the material degradation.
Despite the general agreement in the scientific community nowadays on the OER mechanism occurring on rutile materials, as presented in this dissertation, alternative pathways are proposed occasionally. Since the microkinetic approach allows for quantifying specific steps, it can be adjusted to evaluate the validity and proportion of the overall turnover frequency of various pathways. Assisting DFT-based analyses by providing quantitative insights into reaction rates is especially advisable.
Although the anode-electrolyte interaction in a PEM electrolyzer cell is highly relevant for the performance, other components may be addressed. To understand their impact on the input variables of the reaction kinetics, such as pH, potential, and mass transport, and to elucidate the effect on degradation at different operating points and strategies, a multiscale model or digital twin can be helpful. In either approach, the microkinetic model presented in this dissertation can be incorporated as an essential model component. It may be directly transferable to the use on the cell level.
Despite its here presented application on the OER, the methodology is considered transferable and beneficial in analyzing further electrocatalysts and reactions. The presented model equations are generally valid and serve surface processes other than water adsorption and deprotonation. Its application can be envisioned for many more electrocatalytic systems that can be characterized well by CV. The electrocatalytic CO_2 reduction, the oxygen reduction reaction or the electrolysis of larger molecules are examples of promising reactions in an energy system based on renewable energies. They can benefit from the presented approach. The presented studies in this dissertation serve as examples and as a physical basis for a wide range of electrocatalytic and kinetic studies for further reactions and processes in the field of electrochemical engineering.

Bibliography

(1) Geppert, J.; Röse, P.; Czioska, S.; Escalera-López, D.; Boubnov, A.; Saraçi, E.; Cherevko, S.; Grunwaldt, J.-D.; Krewer, U. Microkinetic Analysis of the Oxygen Evolution Performance at Different Stages of Iridium Oxide Degradation. *J. Am. Chem. Soc.* **2022**, *144*, 13205–13217.

(2) Geppert, J.; Röse, P.; Pauer, S.; Krewer, U. Microkinetic Barriers of the Oxygen Evolution on the Oxides of Iridium, Ruthenium and their Binary Mixtures. *ChemElectroChem* **2022**, *9*, e202200481.

(3) Geppert, J.; Kubannek, F.; Röse, P.; Krewer, U. Identifying the oxygen evolution mechanism by microkinetic modelling of cyclic voltammograms. *Electrochim. Acta* **2021**, *380*, 137902–137914.

(4) Kalz, K. F.; Kraehnert, R.; Dvoyashkin, M.; Dittmeyer, R.; Glaser, R.; Krewer, U.; Reuter, K.; Grunwaldt, J. D. Future Challenges in Heterogeneous Catalysis: Understanding Catalysts under Dynamic Reaction Conditions. *ChemCatChem* **2017**, *9*, 17–29.

(5) Seh, Z. W.; Kibsgaard, J.; Dickens, C. F.; Chorkendorff, I.; Norskov, J. K.; Jaramillo, T. F. Combining theory and experiment in electrocatalysis: Insights into materials design. *Science* **2017**, *355*.

(6) Bernt, M.; Gasteiger, H. A. Influence of Ionomer Content in IrO_2/TiO_2 Electrodes on PEM Water Electrolyzer Performance. *J. Electrochem. Soc.* **2016**, *163*, F3179–F3189.

(7) Carmo, M.; Fritz, D. L.; Mergel, J.; Stolten, D. A comprehensive review on PEM water electrolysis. *IInt. J. Hydrog. Energy* **2013**, *38*, 4901–4934.

(8) Ivanova, M.; Peters, R.; Müller, M.; Haas, S.; Seidler, M. F.; Mutschke, G.; Eckert, K.; Röse, P.; Calnan, S.; Bagacki, R.; Schlatmann, R.; Grosselindemann, C.; Schäfer, L.-A.; Menzler, N. H.; Weber, A.; van de Krol, R.; Liang, F.; Abdi, F. F.; Brendelberger, S.; Neumann, N.; Grobbel, J.; Roeb, M.; Sattler, C.; Duran, I.; Dietrich, B.; Hofberger, C.; Stoppel, L.; Uhlenbruck, N.; Wetzel, T.; Rauner, D.; Hecimovic, A.; Fantz, U.; Kulyk, N.; Harting, J.; Guillon, O. Technological Pathways to Produce Compressed and Highly Pure Hydrogen from Solar Power. *Angew. Chem. Int. Ed.* **2023**, e202218850.

(9) Hansen, J. N.; Prats, H.; Toudahl, K. K.; Morch Secher, N.; Chan, K.; Kibsgaard, J.; Chorkendorff, I. Is There Anything Better than Pt for HER? *ACS Energy Lett.* **2021**, *6*, 1175–1180.

(10) Man, I. C.; Su, H.-Y.; Calle-Vallejo, F.; Hansen, H. A.; Martínez, J. I.; Inoglu, N. G.; Kitchin, J.; Jaramillo, T. F.; Nørskov, J. K.; Rossmeisl, J. Universality in Oxygen Evolution Electrocatalysis on Oxide Surfaces. *ChemCatChem* **2011**, *3*, 1159–1165.

(11) Shi, Z.; Wang, X.; Ge, J.; Liu, C.; Xing, W. Fundamental understanding of the acidic oxygen evolution reaction: mechanism study and state-of-the-art catalysts. *Nanoscale* **2020**, *12*, 13249–13275.

(12) Cherevko, S.; Geiger, S.; Kasian, O.; Kulyk, N.; Grote, J.-P.; Savan, A.; Shrestha, B. R.; Merzlikin, S.; Breitbach, B.; Ludwig, A.; Mayrhofer, K. J. J. Oxygen and hydrogen evolution reactions on Ru, RuO_2, Ir, and IrO_2 thin film electrodes in acidic and alkaline electrolytes: A comparative study on activity and stability. *Catal. Today* **2016**, *262*, 170–180.

(13) Gunasooriya, G. T. K. K.; Nørskov, J. K. Analysis of Acid-Stable and Active Oxides for the Oxygen Evolution Reaction. *ACS Energy Lett.* **2020**, *5*, 3778–3787.

(14) Cherevko, S.; Geiger, S.; Kasian, O.; Mingers, A.; Mayrhofer, K. J. Oxygen evolution activity and stability of iridium in acidic media. Part 2. – Electrochemically grown hydrous iridium oxide. *J. Electroanal. Chem.* **2016**, *774*, 102–110.

(15) Kasian, O.; Geiger, S.; Stock, P.; Polymeros, G.; Breitbach, B.; Savan, A.; Ludwig, A.; Cherevko, S.; Mayrhofer, K. J. J. On the Origin of the Improved Ruthenium Stability in RuO_2–IrO_2 Mixed Oxides. *J. Electrochem. Soc.* **2016**, *163*, F3099.

(16) Rossmeisl, J.; Logadottir, A.; Nørskov, J. K. Electrolysis of water on (oxidized) metal surfaces. *Chem. Phys.* **2005**, *319*, 178–184.

(17) Rossmeisl, J.; Qu, Z. W.; Zhu, H.; Kroes, G. J.; Nørskov, J. K. Electrolysis of water on oxide surfaces. *J. Electroanal. Chem.* **2007**, *607*, 83–89.

(18) Rossmeisl, J.; Jensen, K. D.; Petersen, A. S.; Arnarson, L.; Bagger, A.; Escudero-Escribano, M. Realistic Cyclic Voltammograms from Ab Initio Simulations in Alkaline and Acidic Electrolytes. *J. Phys. Chem. C* **2020**, *124*, 20055–20065.

(19) Halldin Stenlid, J.; Campos dos Santos, E.; Arán-Ais, R. M.; Bagger, A.; Johansson, A. J.; Roldan Cuenya, B.; Rossmeisl, J.; Pettersson, L. G. M. Uncovering the electrochemical interface of low-index copper surfaces in deep groundwater environments. *Electrochim. Acta* **2020**, *362*, 137111.

(20) McCrum, I. T.; Janik, M. J. pH and Alkali Cation Effects on the Pt Cyclic Voltammogram Explained Using Density Functional Theory. *J. Phys. Chem. C* **2016**, *120*, 457–471.

(21) Hörmann, N. G.; Reuter, K. Thermodynamic Cyclic Voltammograms Based on Ab Initio Calculations: Ag(111) in Halide-Containing Solutions. *J. Chem. Theory Comput.* **2021**, *17*, 1782–1794.

(22) Rao, R. R.; Kolb, M. J.; Giordano, L.; Pedersen, A. F.; Katayama, Y.; Hwang, J.; Mehta, A.; You, H.; Lunger, J. R.; Zhou, H.; Halck, N. B.; Vegge, T.; Chorkendorff, I.; Stephens, I. E. L.; Shao-Horn, Y. Operando identification of site-dependent water oxidation activity on ruthenium dioxide single-crystal surfaces. *Nature Catal.* **2020**, *3*, 516–525.

(23) Vidal-Iglesias, F. J.; Solla-Gullón, J.; Montiel, V.; Aldaz, A. An Easy Method for Calculating Kinetic Parameters of Electrochemical Mechanisms: Temkin's Formalism. *Electrocatalysis* **2015**, *6*, 148–154.

(24) Marshall, A. T.; Vaisson-Béthune, L. Avoid the quasi-equilibrium assumption when evaluating the electrocatalytic oxygen evolution reaction mechanism by Tafel slope analysis. *Electrochem. Commun.* **2015**, *61*, 23–26.

(25) Marshall, A. T.; Herritsch, A. Understanding the Hydrogen and Oxygen Evolution Reactions through Microkinetic Models. *ECS Trans.* **2018**, *85*, 121.

(26) Shinagawa, T.; Garcia-Esparza, A. T.; Takanabe, K. Insight on Tafel slopes from a microkinetic analysis of aqueous electrocatalysis for energy conversion. *Sci. Rep.* **2015**, *5*, 1–21.

(27) Schön, P.; Krewer, U. Revealing the complex sulfur reduction mechanism using cyclic voltammetry simulation. *Electrochim. Acta* **2021**, *373*, 137523.

(28) Haisch, T.; Kubannek, F.; Nikitina, L.; Nikitin, I.; Pott, S.; Clees, T.; Krewer, U. The origin of the hysteresis in cyclic voltammetric response of alkaline methanol electrooxidation. *Phys. Chem. Chem. Phys.* **2020**, *22*, 16648–16654.

(29) Clees, T.; Nikitin, I.; Nikitina, L.; Pott, S.; Krewer, U.; Haisch, T. In *Proceedings of 8th International Conference on Simulation and Modeling Methodologies, Technologies and Applications - Volume 1: SIMULTECH*, SciTePress: 2018, pp 279–288.

(30) Kubannek, F.; Krewer, U. A Cyclone Flow Cell for Quantitative Analysis of Kinetics at Porous Electrodes by Differential Electrochemical Mass Spectrometry. *Electrochim. Acta* **2016**, *210*, 862–873.

(31) Röhe, M.; Kubannek, F.; Krewer, U. Processes and Their Limitations in Oxygen Depolarized Cathodes: A Dynamic Model-Based Analysis. *ChemSusChem* **2019**, *12*, 2373–2384.

(32) Krewer, U.; Christov, M.; Vidaković, T.; Sundmacher, K. Impedance spectroscopic analysis of the electrochemical methanol oxidation kinetics. *J. Electroanal. Chem.* **2006**, *589*, 148–159.

(33) Krewer, U.; Vidaković-Koch, T.; Rihko-Struckmann, L. Electrochemical Oxidation of Carbon-Containing Fuels and Their Dynamics in Low-Temperature Fuel Cells. *ChemPhysChem* **2011**, *12*, 2518–44.

(34) Heinrich, M.; Wolff, N.; Harting, N.; Laue, V.; Röder, F.; Seitz, S.; Krewer, U. Physico-Chemical Modeling of a Lithium-Ion Battery: An Ageing Study with Electrochemical Impedance Spectroscopy. *Batter. Supercaps* **2019**, *2*, 530–540.

(35) Vidaković-Koch, T. R.; Panić, V. V.; Andrić, M.; Petkovska, M.; Sundmacher, K. Nonlinear Frequency Response Analysis of the Ferrocyanide Oxidation Kinetics. Part I. A Theoretical Analysis. *J. Phys. Chem. C* **2011**, *115*, 17341–17351.

(36) Wolff, N.; Harting, N.; Röder, F.; Heinrich, M.; Krewer, U. Understanding nonlinearity in electrochemical systems. *Eur. Phys. J.: Spec. Top.* **2019**, *227*, 2617–2640.

(37) Mao, Q.; Krewer, U. Total harmonic distortion analysis of oxygen reduction reaction in proton exchange membrane fuel cells. *Electrochim. Acta* **2013**, *103*, 188–198.

(38) Wagman, D. D.; Evans, W. H.; Parker, V. B.; Schumm, R. H.; Halow, I. The NBS tables of chemical thermodynamic properties. Selected values for inorganic and C_1 and C_2 organic substances in SI units. *J. Phys. Chem. Ref. Data* **1982**, *11*, 2–392.

(39) Matsumoto, Y.; Sato, E. Electrocatalytic properties of transition metal oxides for oxygen evolution reaction. *Mater. Chem. Phys.* **1986**, *14*, 397–426.

(40) Cherevko, S.; Zeradjanin, A. R.; Topalov, A. A.; Kulyk, N.; Katsounaros, I.; Mayrhofer, K. J. Dissolution of Noble Metals during Oxygen Evolution in Acidic Media. *ChemCatChem* **2014**, *6*, 2219–2223.

(41) Lee, Y.; Suntivich, J.; May, K. J.; Perry, E. E.; Shao-Horn, Y. Synthesis and Activities of Rutile IrO_2 and RuO_2 Nanoparticles for Oxygen Evolution in Acid and Alkaline Solutions. *J. Phys. Chem. Lett.* **2012**, *3*, 399–404.

(42) Paoli, E. A.; Masini, F.; Frydendal, R.; Deiana, D.; Malacrida, P.; Hansen, T. W.; Chorkendorff, I.; Stephens, I. E. Fine-tuning the activity of oxygen evolution catalysts: The effect of oxidation pre-treatment on size-selected Ru nanoparticles. *Catal. Today* **2016**, *262*, 57–64.

(43) Trasatti, S. Electrocatalysis in the anodic evolution of oxygen and chlorine. *Electrochim. Acta* **1984**, *29*, 1503–1512.

(44) Ping, Y.; Nielsen, R. J.; Goddard W. A., 3. The Reaction Mechanism with Free Energy Barriers at Constant Potentials for the Oxygen Evolution Reaction at the IrO_2 (110) Surface. *J. Am. Chem. Soc.* **2017**, *139*, 149–155.

(45) Rao, R. R.; Kolb, M. J.; Halck, N. B.; Pedersen, A. F.; Mehta, A.; You, H.; Stoerzinger, K. A.; Feng, Z.; Hansen, H. A.; Zhou, H.; Giordano, L.; Rossmeisl, J.; Vegge, T.; Chorkendorff, I.; Stephens, I. E. L.; Shao-Horn, Y. Towards identifying the active sites on RuO_2(110) in catalyzing oxygen evolution. *Energy Environ. Sci.* **2017**, *10*, 2626–2637.

(46) Bockris, J. O. Kinetics of Activation Controlled Consecutive Electrochemical Reactions: Anodic Evolution of Oxygen. *J. Chem. Phys.* **1956**, *24*, 817–827.

(47) Zagalskaya, A.; Evazzade, I.; Alexandrov, V. Ab Initio Thermodynamics and Kinetics of the Lattice Oxygen Evolution Reaction in Iridium Oxides. *ACS Energy Lett.* **2021**, *6*, 1124–1133.

(48) Arrhenius, S. Über die Reaktionsgeschwindigkeit bei der Inversion von Rohrzucker durch Säuren. *Z. Phys. Chem.* **1889**, *4*.

(49) Eyring, H. The Activated Complex in Chemical Reactions. *J. Chem. Phys.* **1935**, *3*, 107–115.

(50) Evans, M. G.; Polanyi, M. Some applications of the transition state method to the calculation of reaction velocities, especially in solution. *Trans. Faraday Soc.* **1935**, *31*.

(51) Marcus, R. A. On the Theory of Electron-Transfer Reactions. VI. Unified Treatment for Homogeneous and Electrode Reactions. *J. Chem. Phys.* **1965**, *43*, 679–701.

(52) Bard, A. J.; Faulkner, L. R., *Electrochemical Methods: Fundamentals and Applications, 2nd Edition*; Wiley: 2001.

(53) Eliaz, N.; Gileadi, E., *Physical Electrochemistry: Fundamentals, Techniques, and Applications, 2nd Edition*; Wiley-VCH: 2018.

(54) Volmer, M. Thermodynamische Folgerungen ans der Zustandsgleichung für adsorbierte Stoffe. *Z. Phys. Chem.* **1925**, *115U*, 253–260.

(55) De Boer, J. H., *The dynamical character of adsorption*; Clarendon Press: London, 1953.

(56) Frumkin, A. Die Kapillarkurve der höheren Fettsäuren und die Zustandsgleichung der Oberflächenschicht. *Z. Phys. Chem.* **1925**, *116U*, 466–484.

(57) Afonso, R.; Gales, L.; Mendes, A. Kinetic derivation of common isotherm equations for surface and micropore adsorption. *Adsorption* **2016**, *22*, 963–971.

(58) Langmuir, I. The Adsorption of Gases on Plane Surfaces of Glass, Mica and Platinum. *J. Am. Chem. Soc.* **1918**, *40*, 1361–1403.

(59) Hill, T. L. Statistical Mechanics of Multimolecular Adsorption II. Localized and Mobile Adsorption and Absorption. *J. Chem. Phys.* **1946**, *14*, 441–453.

(60) Hill, T. L. Statistical Thermodynamics of the Transition Region between Two Phases. II. One Component System with a Plane Interface. *J. Chem. Phys.* **1952**, *20*, 141–144.

(61) Van der Waals, J. D., *Over de Continuiteit van den Gas- en Vloeistoftoestand*; Sijthoff: 1873.

(62) Saraby-Reintjes, A. Electrocatalysis under Temkin adsorption conditions. *J. Chem. Soc., Faraday Trans.* **1987**, *83*.

(63) Lewandowski, A.; Szymczyk, K. Adsorption of monoterpene alcohols at the water–air interface. *Adsorption* **2019**, *25*, 301–308.

(64) Böld, W.; Breiter, M. Untersuchung des anodischen Aufbaus und der kathodischen Reduktion der Sauerstoffbelegung am Rhodium und Iridium. *Electrochim. Acta* **1961**, *5*, 169–179.

(65) Rand, D. A. J.; Woods, R.; Melbourne, P. Cyclic Voltammetric Studies on Iridium Electrodes in Sulphuric Acid Solutions. *J. Electroanal. Chem.* **1974**, *55*, 375–381.

(66) Petit, M. A.; Plichon, V. Anodic electrodeposition of iridium oxide films. *J. Electroanal. Chem.* **1998**, *444*, 247–252.

(67) Kasian, O.; Geiger, S.; Li, T.; Grote, J. P.; Schweinar, K.; Zhang, S.; Scheu, C.; Raabe, D.; Cherevko, S.; Gault, B.; Mayrhofer, K. J. Degradation of iridium oxides via oxygen evolution from the lattice: Correlating atomic scale structure with reaction mechanisms. *Energy Environ. Sci.* **2019**, *12*, 3548–3555.

(68) Conway, B. E.; Mozota, J. Behaviour Processes At Oxidized Iridium. *Electrochim. Acta* **1983**, *28*, 9.

(69) Mozota, J.; Conway, B. E. Surface and Bulk Processes At Oxidized Iridium Stage and Transition To Reversible Oxide Film Behaviour. *Electrochim. Acta* **1983**, *28*, 1–8.

(70) Burke, L. D.; Mulcahy, J. K.; Whelan, D. P. Preparation of an oxidized iridium electrode and the variation of its potential with pH. *J. Electroanal. Chem.* **1984**, *163*, 117–128.

(71) Pickup, P. G.; Birss, V. I. The kinetics of charging and discharging of iridium oxide films in aqueous and non-aqueous media. *J. Electroanal. Chem.* **1988**, *240*, 185–199.

(72) Gottesfeld, S.; Srinivasan, S. Electrochemical and optical studies of thick oxide layers on iridium and their electrocatalytic activities for the oxygen evolution reaction. *J. Electroanal. Chem.* **1978**, *86*, 89–104.

(73) Buckley, D. N.; Burke, L. D. The oxygen electrode. Part 5.—Enhancement of charge capacity of an iridium surface in the anodic region. *J. Chem. Soc., Faraday Trans.* **1975**, *71*, 1447.

(74) Kötz, R.; Neff, H.; Stucki, S. Anodic Iridium Oxide Films: XPS-Studies of Oxidation State Changes and O_2-Evolution. *J. Electrochem. Soc.* **1984**, *131*, 72.

(75) Michell, D.; A .J. Rand, D.; Woods, R. Analysis of the anodic oxygen layer on iridium by X-ray emission, electron diffraction and electron microscopy. *J. Electroanal. Chem.* **1977**, *84*, 117–126.

(76) Mo, Y.; Stefan, I. C.; Cai, W. B.; Dong, J.; Carey, P.; Scherson, D. A. In situ iridium LIII-edge X-ray absorption and surface enhanced Raman spectroscopy of electrodeposited iridium oxide films in aqueous electrolytes. *J. Phys. Chem. B* **2002**, *106*, 3681–3686.

(77) Geiger, S.; Kasian, O.; Shrestha, B. R.; Mingers, A. M.; Mayrhofer, K. J. J.; Cherevko, S. Activity and Stability of Electrochemically and Thermally Treated Iridium for the Oxygen Evolution Reaction. *J. Electrochem. Soc.* **2016**, *163*, F3132–F3138.

(78) Da Silva, G. C.; Perini, N.; Ticianelli, E. A. Effect of temperature on the activities and stabilities of hydrothermally prepared IrO_x nanocatalyst layers for the oxygen evolution reaction. *Appl. Catal., B* **2017**, *218*, 287–297.

(79) Pfeifer, V.; Jones, T. E.; Velasco Vélez, J. J.; Massué, C.; Greiner, M. T.; Arrigo, R.; Teschner, D.; Girgsdies, F.; Scherzer, M.; Allan, J.; Hashagen, M.; Weinberg, G.; Piccinin, S.; Hävecker, M.; Knop-Gericke, a.; Schlögl, R. The electronic structure of iridium oxide electrodes active in water splitting. *Phys. Chem. Chem. Phys.* **2016**, *18*, 2292–2296.

(80) Hüppauff, M. Valency and Structure of Iridium in Anodic Iridium Oxide Films. *J. Electrochem. Soc.* **1993**, *140*, 598.

(81) Minguzzi, A.; Lugaresi, O.; Achilli, E.; Locatelli, C.; Vertova, A.; Ghigna, P.; Rondinini, S. Observing the oxidation state turnover in heterogeneous iridium-based water oxidation catalysts. *Chem. Sci.* **2014**, *5*, 3591–3597.

(82) Hillman, A. R.; Skopek, M. A.; Gurman, S. J. X-ray spectroscopy of electrochemically deposited iridium oxide films: Detection of multiple sites through structural disorder. *Phys. Chem. Chem. Phys.* **2011**, *13*, 5252–5263.

(83) Saveleva, V. A.; Wang, L.; Teschner, D.; Jones, T.; Gago, A. S.; Friedrich, K. A.; Zafeiratos, S.; Schlögl, R.; Savinova, E. R. Operando Evidence for a Universal Oxygen Evolution Mechanism on Thermal and Electrochemical Iridium Oxides. *J. Phys. Chem. Lett.* **2018**, *9*, 3154–3160.

(84) Klyukin, K.; Zagalskaya, A.; Alexandrov, V. Ab Initio Thermodynamics of Iridium Surface Oxidation and Oxygen Evolution Reaction. *J. Phys. Chem. C* **2018**, *122*, 29350–29358.

(85) Otten, J. M.; Visscher, W. The anodic behaviour of iridium. I. The effect of potential cycling. *J. Electroanal. Chem.* **1974**, *55*, 1–11.

(86) Birss, V. Electron Microscopy Study of Formation of Thick Oxide Films on Ir and Ru Electrodes. *J. Electrochem. Soc.* **1984**, *131*, 1502.

(87) Steegstra, P.; Busch, M.; Panas, I.; Ahlberg, E. Revisiting the Redox Properties of Hydrous Iridium Oxide Films in the Context of Oxygen Evolution. *J. Phys. Chem. C* **2013**, *117*, 20975–20981.

(88) Kasian, O.; Grote, J. P.; Geiger, S.; Cherevko, S.; Mayrhofer, K. J. The Common Intermediates of Oxygen Evolution and Dissolution Reactions during Water Electrolysis on Iridium. *Angew. Chem. Int. Ed.* **2018**, *57*, 2488–2491.

(89) Hansen, H. A.; Viswanathan, V.; Nørskov, J. K. Unifying Kinetic and Thermodynamic Analysis of 2 e^- and 4 e^- Reduction of Oxygen on Metal Surfaces. *J. Phys. Chem. C* **2014**, *118*, 6706–6718.

(90) Bessler, W. G.; Gewies, S.; Vogler, M. A new framework for physically based modeling of solid oxide fuel cells. *Electrochim. Acta* **2007**, *53*, 1782–1800.

(91) Hückel, E. General discussion. *Trans. Faraday Soc.* **1932**, *28*, 410–447.

(92) Cassel, H. M. Cluster Formation and Phase Transitions in the Adsorbed State. *J. Phys. Chem.* **1944**, *48*, 195–202.

(93) Laviron, E. The use of linear potential sweep voltammetry and of a.c. voltammetry for the study of the surface electrochemical reaction of strongly adsorbed systems and of redox modified electrodes. *J. Electroanal. Chem.* **1979**, *100*, 263–270.

(94) Vidaković, T.; Christov, M.; Sundmacher, K. A method for rough estimation of the catalyst surface area in a fuel cell. *J. Appl. Electrochem.* **2009**, *39*, 213–225.

(95) Pickup, P. G.; Birss, V. I. A model for anodic hydrous oxide growth at iridium. *J. Electroanal. Chem.* **1987**, *220*, 83–100.

(96) Das, K. Single Ion Activities in Aqueous Sulfuric Acid Solutions: A New Extra-Thermodynamic Assumption. *J. Solut. Chem.* **1988**, *17*, 327.

(97) Robertson, E. B.; Dunford, H. B. The State of the Proton in Aqueous Sulfuric Acid. *J. Am. Chem. Soc.* **1964**, *86*, 5080.

(98) McIntyre, J. D. E.; Basu, S.; Peck, W. F.; Brown, W. L.; Augustyniak, W. M. Cation insertion reactions of electrochromic tungsten and iridium oxide films. *Phys. Rev. B* **2002**, *25*, 7242–7254.

(99) Burke, L. D.; O'Sullivan, E. J. Oxygen gas evolution on hydrous oxides - An example of three-dimensional electrocatalysis? *J. Electroanal. Chem.* **1981**, *117*, 155.

(100) Stoerzinger, K. A.; Qiao, L.; Biegalski, M. D.; Shao-Horn, Y. Orientation-Dependent Oxygen Evolution Activities of Rutile IrO_2 and RuO_2. *J. Phys. Chem. Lett.* **2014**, *5*, 1636–41.

(101) Gottesfeld, S. Electrochromism in Anodic Iridium Oxide Films. *J. Electrochem. Soc.* **1979**, *126*, 742.

(102) Gonzalez, D.; Heras-Domingo, J.; Pantaleone, S.; Rimola, A.; Rodriguez-Santiago, L.; Solans-Monfort, X.; Sodupe, M. Water Adsorption on MO_2 (M = Ti, Ru, and Ir) Surfaces. Importance of Octahedral Distortion and Cooperative Effects. *ACS Omega* **2019**, *4*, 2989–2999.

(103) Bagger, A.; Arán-Ais, R. M.; Halldin Stenlid, J.; Campos dos Santos, E.; Arnarson, L.; Degn Jensen, K.; Escudero-Escribano, M.; Roldan Cuenya, B.; Rossmeisl, J. Ab Initio Cyclic Voltammetry on Cu(111), Cu(100) and Cu(110) in Acidic, Neutral and Alkaline Solutions. *ChemPhysChem* **2019**, *20*, 3096–3105.

(104) Czioska, S.; Boubnov, A.; Escalera-López, D.; Geppert, J.; Zagalskaya, A.; Röse, P.; Saraçi, E.; Alexandrov, V.; Krewer, U.; Cherevko, S.; Grunwaldt, J.-D. Increased Ir–Ir Interaction in Iridium Oxide during the Oxygen Evolution Reaction at High Potentials Probed by Operando Spectroscopy. *ACS Catal.* **2021**, 10043–10057.

(105) Czioska, S.; Ehelebe, K.; Geppert, J.; Escalera-López, D.; Boubnov, A.; Saraçi, E.; Mayerhöfer, B.; Krewer, U.; Cherevko, S.; Grunwaldt, J.-D. Heating up the OER: Investigation of IrO_2 OER Catalysts as Function of Potential and Temperature**. *ChemElectroChem* **2022**, *9*, e202200514.

(106) Gao, J.; Xu, C. Q.; Hung, S. F.; Liu, W.; Cai, W.; Zeng, Z.; Jia, C.; Chen, H. M.; Xiao, H.; Li, J.; Huang, Y.; Liu, B. Breaking Long-Range Order in Iridium Oxide by Alkali Ion for Efficient Water Oxidation. *J. Am. Chem. Soc.* **2019**, *141*, 3014–3023.

(107) Minke, C.; Suermann, M.; Bensmann, B.; Hanke-Rauschenbach, R. Is iridium demand a potential bottleneck in the realization of large-scale PEM water electrolysis? *Int. J. Hydrog. Energy* **2021**, *46*, 23581–23590.

(108) Ehelebe, K.; Escalera-López, D.; Cherevko, S. Limitations of aqueous model systems in the stability assessment of electrocatalysts for oxygen reactions in fuel cell and electrolysers. *Curr. Opin. Electrochem.* **2021**, *29*, 100832.

(109) El-Sayed, H. A.; Weiß, A.; Olbrich, L. F.; Putro, G. P.; Gasteiger, H. A. OER Catalyst Stability Investigation Using RDE Technique: A Stability Measure or an Artifact? *J. Electrochem. Soc.* **2019**, *166*, F458–F464.

(110) Escalera-López, D.; Czioska, S.; Geppert, J.; Boubnov, A.; Röse, P.; Saraçi, E.; Krewer, U.; Grunwaldt, J.-D.; Cherevko, S. Phase- and Surface Composition-Dependent Electrochemical Stability of Ir-Ru Nanoparticles during Oxygen Evolution Reaction. *ACS Catal.* **2021**, 9300–9316.

(111) Briquet, L. G. V.; Sarwar, M.; Mugo, J.; Jones, G.; Calle-Vallejo, F. A New Type of Scaling Relations to Assess the Accuracy of Computational Predictions of Catalytic Activities Applied to the Oxygen Evolution Reaction. *ChemCatChem* **2017**, *9*, 1261–1268.

(112) Dickens, C. F.; Kirk, C.; Nørskov, J. K. Insights into the Electrochemical Oxygen Evolution Reaction with ab Initio Calculations and Microkinetic Modeling: Beyond the Limiting Potential Volcano. *J. Phys. Chem. C* **2019**, *123*, 18960–18977.

(113) Exner, K. S.; Over, H. Beyond the Rate-Determining Step in the Oxygen Evolution Reaction over a Single-Crystalline IrO_2(110) Model Electrode: Kinetic Scaling Relations. *ACS Catal.* **2019**, *9*, 6755–6765.

(114) Exner, K. S. A Universal Descriptor for the Screening of Electrode Materials for Multiple-Electron Processes: Beyond the Thermodynamic Overpotential. *ACS Catal.* **2020**, *10*, 12607–12617.

(115) Nong, H. N.; Falling, L. J.; Bergmann, A.; Klingenhof, M.; Tran, H. P.; Spori, C.; Mom, R.; Timoshenko, J.; Zichittella, G.; Knop-Gericke, A.; Piccinin, S.; Perez-Ramirez, J.; Cuenya, B. R.; Schlögl, R.; Strasser, P.; Teschner, D.; Jones, T. E. Key role of chemistry versus bias in electrocatalytic oxygen evolution. *Nature* **2020**, *587*, 408–413.

(116) Dam, A. P.; Papakonstantinou, G.; Sundmacher, K. On the role of microkinetic network structure in the interplay between oxygen evolution reaction and catalyst dissolution. *Sci. Rep.* **2020**, *10*, 14140.

(117) Weiß, A.; Siebel, A.; Bernt, M.; Shen, T. H.; Tileli, V.; Gasteiger, H. A. Impact of Intermittent Operation on Lifetime and Performance of a PEM Water Electrolyzer. *J. Electrochem. Soc.* **2019**, *166*, F487–F497.

(118) Naito, T.; Shinagawa, T.; Nishimoto, T.; Takanabe, K. Recent advances in understanding oxygen evolution reaction mechanisms over iridium oxide. *Inorg. Chem. Front.* **2021**, *8*, 2900–2917.

(119) Inaba, M.; Quinson, J.; Arenz, M. pH matters: The influence of the catalyst ink on the oxygen reduction activity determined in thin film rotating disk electrode measurements. *J. Power Sources* **2017**, *353*, 19–27.

(120) Garsany, Y.; Ge, J.; St-Pierre, J.; Rocheleau, R.; Swider-Lyons, K. E. Analytical Procedure for Accurate Comparison of Rotating Disk Electrode Results for the Oxygen Reduction Activity of Pt/C. *J. Electrochem. Soc.* **2014**, *161*, F628–F640.

(121) Reier, T.; Teschner, D.; Lunkenbein, T.; Bergmann, A.; Selve, S.; Kraehnert, R.; Schlögl, R.; Strasser, P. Electrocatalytic Oxygen Evolution on Iridium Oxide: Uncovering Catalyst-Substrate Interactions and Active Iridium Oxide Species. *J. Electrochem. Soc.* **2014**, *161*, F876–F882.

(122) Sanchez Casalongue, H. G.; Ng, M. L.; Kaya, S.; Friebel, D.; Ogasawara, H.; Nilsson, A. In situ observation of surface species on iridium oxide nanoparticles during the oxygen evolution reaction. *Angew. Chem. Int. Ed.* **2014**, *53*, 7169–72.

(123) Alia, S. M.; Rasimick, B.; Ngo, C.; Neyerlin, K. C.; Kocha, S. S.; Pylypenko, S.; Xu, H.; Pivovar, B. S. Activity and Durability of Iridium Nanoparticles in the Oxygen Evolution Reaction. *J. Electrochem. Soc.* **2016**, *163*, F3105–F3112.

(124) Boudart, M. Ammonia synthesis: The bellwether reaction in heterogeneous catalysis. *Top. Catal.* **1994**, *1*, 405–414.

(125) Sen, F. G.; Kinaci, A.; Narayanan, B.; Gray, S. K.; Davis, M. J.; Sankaranarayanan, S. K. R. S.; Chan, M. K. Y. Towards accurate prediction of catalytic activity in IrO_2 nanoclusters via first principles-based variable charge force field. *J. Mater. Chem. A* **2015**, *3*, 18970–18982.

(126) Kralchevsky, P. A.; Danov, K. D.; Kolev, V. L.; Broze, G.; Mehreteab, A. Effect of Nonionic Admixtures on the Adsorption of Ionic Surfactants at Fluid Interfaces. 1. Sodium Dodecyl Sulfate and Dodecanol. *Langmuir* **2003**, *19*, 5004–5018.

(127) Jung, S.; McCrory, C. C. L.; Ferrer, I. M.; Peters, J. C.; Jaramillo, T. F. Benchmarking nanoparticulate metal oxide electrocatalysts for the alkaline water oxidation reaction. *J. Mater. Chem. A* **2016**, *4*, 3068–3076.

(128) Watzele, S.; Hauenstein, P.; Liang, Y.; Xue, S.; Fichtner, J.; Garlyyev, B.; Scieszka, D.; Claudel, F.; Maillard, F.; Bandarenka, A. S. Determination of Electroactive Surface Area of Ni-, Co-, Fe-, and Ir-Based Oxide Electrocatalysts. *ACS Catal.* **2019**, *9*, 9222–9230.

(129) Limaye, A. M.; Zeng, J. S.; Willard, A. P.; Manthiram, K. Bayesian data analysis reveals no preference for cardinal Tafel slopes in CO_2 reduction electrocatalysis. *Nat. Commun.* **2021**, *12*, 703.

(130) Zagalskaya, A.; Alexandrov, V. Role of Defects in the Interplay between Adsorbate Evolving and Lattice Oxygen Mechanisms of the Oxygen Evolution Reaction in RuO_2 and IrO_2. *ACS Catal.* **2020**, *10*, 3650–3657.

(131) Mayrhofer, K. J. J.; Meier, J. C.; Ashton, S. J.; Wiberg, G. K. H.; Kraus, F.; Hanzlik, M.; Arenz, M. Fuel cell catalyst degradation on the nanoscale. *Electrochem. Commun.* **2008**, *10*, 1144–1147.

(132) Mauritz, K. A.; Moore, R. B. State of Understanding of Nafion. *Chem. Rev.* **2004**, *104*, 4535–85.

(133) Zhang, K.; Zou, R. Advanced Transition Metal-Based OER Electrocatalysts: Current Status, Opportunities, and Challenges. *Small* **2021**, *17*, e2100129.

(134) Cheng, J.; Zhang, H.; Chen, G.; Zhang, Y. Study of $Ir_xRu_{1-x}O_2$ oxides as anodic electrocatalysts for solid polymer electrolyte water electrolysis. *Electrochim. Acta* **2009**, *54*, 6250–6256.

(135) Kötz, R.; Stucki, S. Stabilization of RuO_2 by IrO_2 for anodic oxygen evolution in acid media. *Electrochim. Acta* **1986**, *31*, 1311–1316.

(136) Roginskaya, Y. E.; Varlamova, T. V.; Goldstein, M. D.; Belova, I. D.; Galyamov, B. S.; Shifrina, R. R.; Shepelin, V. A.; Fateev, V. N. Formation, structure and electrochemical properties of IrO_2-RuO_2 oxide electrodes. *Mater. Chem. Phys.* **1991**, *30*, 101–113.

(137) Murakami, Y.; Miwa, K.; Ueno, M.; Ito, M.; Yahikozawa, K.; Takasu, Y. Morphology of Ultrafine RuO_2-IrO_2 Binary Oxide Particles Prepared by a Sol-Gel Process. *J. Electrochem. Soc.* **2019**, *141*, L118–L120.

(138) Man, I. C. Theoretical study of Electro-catalysts for oxygen evolution, Ph.D. Thesis, Technical University of Denmark, 2011.

(139) Reksten, A. H.; Thuv, H.; Seland, F.; Sunde, S. The oxygen evolution reaction mechanism at $Ir_xRu_{1-x}O_2$ powders produced by hydrolysis synthesis. *J. Electroanal. Chem.* **2018**, *819*, 547–561.

(140) Ikeshoji, T.; Otani, M. Toward full simulation of the electrochemical oxygen reduction reaction on Pt using first-principles and kinetic calculations. *Phys. Chem. Chem. Phys.* **2017**, *19*, 4447–4453.

(141) Ma, Z.; Zhang, Y.; Liu, S.; Xu, W.; Wu, L.; Hsieh, Y.-C.; Liu, P.; Zhu, Y.; Sasaki, K.; Renner, J. N.; Ayers, K. E.; Adzic, R. R.; Wang, J. X. Reaction mechanism for oxygen evolution on RuO_2, IrO_2, and RuO_2@IrO_2 core-shell nanocatalysts. *J. Electroanal. Chem.* **2018**, *819*, 296–305.

(142) Mattos-Costa, F.; de Lima-Neto, P.; Machado, S.; Avaca, L. Characterisation of surfaces modified by sol-gel derived $Ru_xIr_{1-x}O_2$ coatings for oxygen evolution in acid medium. *Electrochim. Acta* **1998**, *44*, 1515–1523.

(143) Galizzioli, D.; Tantardini, F.; Trasatti, S. Ruthenium dioxide: a new electrode material. I. Behaviour in acid solutions of inert electrolytes. *J. Appl. Electrochem.* **1974**, *4*, 57–67.

(144) Horkans, J.; Shafer, M. W. An Investigation of the Electrochemistry of a Series of Metal Dioxides with Rutile-Type Structure: MoO_2, WO_2, ReO_2, RuO_2, OsO_2, and IrO_2. *J. Electrochem. Soc.* **1977**, *124*, 1202.

(145) Kötz, R.; Stucki, S. Oxygen Evolution and Corrosion on Ruthenium-Iridium Alloys. *J. Electrochem. Soc.* **1985**, *132*, 103.

(146) Saveleva, V. A.; Wang, L.; Luo, W.; Zafeiratos, S.; Ulhaq-Bouillet, C.; Gago, A. S.; Friedrich, K. A.; Savinova, E. R. Uncovering the Stabilization Mechanism in Bimetallic Ruthenium-Iridium Anodes for Proton Exchange Membrane Electrolyzers. *J. Phys. Chem. Lett.* **2016**, *7*, 3240–5.

(147) Cole, S. R.; Chu, H.; Greenland, S. Maximum likelihood, profile likelihood, and penalized likelihood: a primer. *Am. J. Epidemiol.* **2014**, *179*, 252–60.

(148) Raue, A.; Kreutz, C.; Maiwald, T.; Bachmann, J.; Schilling, M.; Klingmuller, U.; Timmer, J. Structural and practical identifiability analysis of partially observed dynamical models by exploiting the profile likelihood. *Bioinformatics* **2009**, *25*, 1923–9.

List of Symbols and Abbreviations

List of Symbols

A	area	m^2
a	activity	–
C	capacitance	$F\ m^{-2}$
c	concentration	$mol\ m^{-3}$
E	electrical potential	V
e	elementary charge	As
F	Faraday constant	$A\ s\ mol^{-1}$
f	frequency	Hz
G	free energy	eV
g	interaction factor	–
i	current	A
j	current density	$A\ m^{-2}$
j_0	exchange current density	$A\ m^{-2}$
K	equilibrium constant	-
k	rate constant	s^{-1}
k_0	pre-exponential frequency factor	s^{-1}
k_B	Boltzmann constant	$eV\ K^{-1}$
o	nominal oxidation state	–
p	pressure	$N\ m^{-2}$
q	charge	A s
R	resistance	Ω
r	reaction rate	s^{-1}
T	temperature	K
t	time	s

x	molar fraction	-
α	charge transfer coefficient	–
β	symmetry factor	–
δ	change in oxidation state	–
ν	stoichiometric coefficient	–
Ω	species	–
ρ	density of active sites	m^{-2}
θ	coverage	–

Indices

+	forward
-	backward
a	activation
dl	double layer
el	electrolyte
int	interaction
r	reaction
sur	surface

Abbreviations

BRI	Bridge
CUS	Coordinatively unsaturated site
CV	Cyclic voltammetry
DFT	Density functional theory
ECSA	Electroactive surface area
EIS	Electrochemical impedance spectroscopy
HER	Hydrogen evolution reaction
OER	Oxygen evolution reaction
PCET	Proton-coupled electron transfer

PEEK	Polyether ether ketone
PEM	Proton exchange membrane
PTFE	Polytetrafluoroethylene
RDE	Rotating disc electrode
RHE	Reversible hydrogen electrode
rmse	Root mean square error
XAS	X-ray absorption spectroscopy
XPS	X-ray photoelectron spectroscopy

A Modeling Details

A.1 Model Code of a PCET

The model code provided in this section is based on the mathematical description in section 2.4 and used to calculate the results in section 2.5.

File: start.m

```
%% Microkinetic model of electrocatalytic surface processes
clear all

% Define parameters
run parameterset.m

% Select adsorption isotherm: 'Langmuir', 'Frumkin' or Hill-de-Boer'
p.ads_isotherm = 'Hill-de-Boer';

% Run model
run dynamic_model

% Tidy up
clearvars -except sim p
```

File: parameterset.m

```
%% Define model parameters

p.e = 1.6021766*10^-19; % elementary charge [J eV^-1] = [C]
p.F = 96485;            % Faraday constant [As mol^-1]
p.k_B = 8.617333*10^-5; % Boltzmann constant [eV K^-1]

p.T = 298.15;           % temperatur [K]
p.R_ohm = 20;           % ohmic electrolyte resistance [Ohms]
p.r = 2.5*10^-3;        % electrode radius [m]
p.A = pi*p.r^2;         % geometric electrode area [m^2]
p.C_dl = 0.025;         % double layer capacitance [F m^-2]
p.rho = 10^-4;          % density of active sites [mol m^-2]

p.a_H = 1;              % activity of H+ ions [-]
p.a_H2O = 1;            % activity of H2O [-]
p.a = [p.a_H];         % activtiy vector [-]

p.k_0 = 343.1;          % pre-exponential frequency factor [s^-1]
p.beta = 0.5;           % symmetry factor [-]

p.dG_a = [0]';          % activation free energy vector [eV]
p.dG_r = [1]';          % reaction free energy vector [eV]
p.dG_int = [0 0];       % interaction free energy vector [eV]
p.nu_f = [[0 0 1 0]];   % forward soichiometric coefficients matrix
p.nu_b = [[1 1 0 1]];   % backward soichiometric coefficients matrix

p.nu = p.nu_f - p.nu_b; % soichiometric coefficients matrix
p.iel = 1;              % index of electrolyte species [=1:length(p.a)]
p.ie = 2;               % index of electrons [=length(p.a)+1]
p.isur = 3:4;           % index of surface species [=p.ie+1:length(p.nu)]

p.E_min = 0.5;          % minimum (starting) potential [V]
p.E_max = 1.5;          % maximum potential [V]
p.dE = 0.200;           % potential scan rate [V s^-1]
p.E_num = 500;          % number of potential steps [-]
```

File: dynamic_model.m

```
%% Simulate equilibrium conditions at starting potential
% Define ode solver input
p.experiment = 'CP';
p.t = linspace(0,10,10);
x0 = [ones(1,length(p.isur))./length(p.isur) p.E_min];

% Set solver options and run solver
options = odeset('abstol', 10^-12, 'MaxStep', 0.01);
[t y] = ode23s(@dynamic_ode, p.t, x0, options, p);

%% Simulate cyclic voltammogram experiment
% Define ode solver input
p.experiment = 'CV';
p.t = linspace(0,2*(p.E_max-p.E_min)/p.dE,2*p.E_num);
x0 = [y(end,1:end-1) p.E_min];

% Set solver options and run solver
options = odeset('abstol', 10^-12, 'MaxStep', 0.01);
[t y] = ode23s(@dynamic_ode, p.t, x0, options, p);

%% Postprocessing the dynamic CV simulation output
% Restructure solver output
sim.theta = y(1:end,1:end-1);
sim.t = t(1:end);
sim.E = y(1:end,end);
sim.Edot = diff(y(:,end))./diff(sim.t);
sim.Edot(end+1) = sim.Edot(end);
sim.E_ext = [p.E_min + p.t(1:p.E_num)*p.dE p.E_max - ...
            (p.t(p.E_num+1:2*p.E_num)-p.t(p.E_num))*p.dE]';

% Calculate reaction rates
for i = 1:length(sim.E)
    [sim.r(i,:)]  = dynamic_rates(p,sim.theta(i,:),sim.E(i));
end

% Calculate current density
sim.j = p.F .* p.rho .* sum(-p.nu(:,p.ie)'.*(sim.r),2) + p.C_dl*sim.Edot;
```

File: dynamic_ode.m

```
function [dxdt] = dynamic_ode(t,x,p)

% Allocate coverage and potential
theta = x(1:end-1)';
E = x(end);

% Define the potential depending on the selected experiment
switch p.experiment
    case 'CV'
        [val idx] = min(abs(p.t - t));
        if idx <= p.E_num
            E_ext = p.E_min + t*p.dE;
        end
        if idx > p.E_num
            E_ext = p.E_max - (t-p.t(p.E_num))*p.dE;
        end
    case 'CP'
            E_ext = p.E_min;
end

% Calculate reaction rates
[r] = dynamic_rates(p,theta,E);

% Calculate change in theta
dtheta = sum(-p.nu(:,p.isur).*(r),1)';

% Calculate change in Potential including R correction and double layer
dE = (E_ext - E - p.A*p.R_ohm*p.F*p.rho*sum(-p.nu(:,p.ie).*(r),1)) ...
    / (p.A*p.R_ohm*p.C_dl) / (max(p.t)/length(p.t));

% Output vector is defined as the derivatives of the input vector
dxdt = [dtheta; dE];
end
```

File: dynamic_rates.m

```
function [r] = dynamic_rates(p,theta,E)

% Calculate adsorption functions of the selected isoterm
switch p.ads_isotherm
    case 'Langmuir'
        f_f = 1;
        f_b = 1;
    case 'Frumkin'
        f_f = exp(p.beta*(...
              prod((p.dG_int.*theta./(p.k_B*p.T)).^p.nu_f(:,p.isur),2)...
             -prod((p.dG_int.*theta./(p.k_B*p.T)).^p.nu_b(:,p.isur),2)));
        f_b = exp((1-p.beta)*(...
              prod((p.dG_int.*theta./(p.k_B*p.T)).^p.nu_b(:,p.isur),2)...
             -prod((p.dG_int.*theta./(p.k_B*p.T)).^p.nu_f(:,p.isur),2)));
    case 'Hill-de-Boer'
        f_f = exp(p.beta*(...
              prod((p.dG_int.*theta./(p.k_B*p.T)).^p.nu_f(:,p.isur),2)...
             -prod((p.dG_int.*theta./(p.k_B*p.T)).^p.nu_b(:,p.isur),2)...
             +prod(theta.^p.nu_f(:,p.isur)./theta.^p.nu_b(:,p.isur),2)...
             -prod(theta.^p.nu_b(:,p.isur)./theta.^p.nu_f(:,p.isur),2)));
        f_f(isnan(f_f)) = 1;
        f_b = exp((1-p.beta)*(...
              prod((p.dG_int.*theta./(p.k_B*p.T)).^p.nu_b(:,p.isur),2)...
             -prod((p.dG_int.*theta./(p.k_B*p.T)).^p.nu_f(:,p.isur),2)...
             +prod(theta.^p.nu_b(:,p.isur)./theta.^p.nu_f(:,p.isur),2)...
             -prod(theta.^p.nu_f(:,p.isur)./theta.^p.nu_b(:,p.isur),2)));
        f_b(isnan(f_b)) = 1;
end

% Calculate reaction rates
r_f = prod([p.a.^p.nu_f(:,p.iel) theta.^p.nu_f(:,p.isur)],2).*f_f.*p.k_0...
      .*exp((-p.dG_a-p.beta*p.dG_r+p.beta.*abs(p.nu(:,p.ie)).*E)...
             ./(p.k_B*p.T));
r_f(isnan(r_f)) = 0;
r_b = prod([p.a.^p.nu_b(:,p.iel) theta.^p.nu_b(:,p.isur)],2).*f_b.*p.k_0...
      .*exp((-p.dG_a+(1-p.beta)*p.dG_r-(1-p.beta).*abs(p.nu(:,p.ie)).*E)...
             ./(p.k_B*p.T));
r_b(isnan(r_b)) = 0;
r = r_f-r_b;
end
```

A.2 Parameter Identification Process[11]

The identification of the parameter values of the reaction free energies, the activation free energies and the interaction free energies, the double layer capacitance and the density of active sites requires to solve the optimization problem given in equation A.1.

$$\begin{aligned} P: \quad & \min_{x} \mathcal{J}(x) \\ \text{s.t.} \quad & x_{\text{lb}} \leq x \leq x_{\text{ub}} \end{aligned} \tag{A.1}$$

$\mathcal{J}$ is the objective function defined by the root mean squared error given in equation 3.16. x is the vector of input variables $x \in \{\Delta G^0_{\text{r},i},\ \Delta G_{\text{a},i},\ \Delta G_{\text{int},j},\ \rho,\ c_{\text{dl}}\},\ \forall i,\ \forall j$ of the set of reactions i and the set of adsorbed species j. For pristine IrO_2 the design space is defined by the lower and upper bound values x_{lb} and x_{ub} respectively, given by the minimal and maximal values of the ranges in Table A.1.

Table A.1: Ranges of the reaction free energy, the activation free energy, and the reactant species interaction energy of reaction steps 1 to 7 and the the double layer capacitance and the density of active sites on IrO_2 defining the design space for the parameter identification process.

step	ΔG^0_{r} / eV	ΔG_{a} / eV	ΔG_{int} / eV	ρ / mol m^{-2}	c_{dl} / F m^{-2}
1	[-3, 1]	[0, 0.15]	[0, 0.2]		
2	[0.7, 0.9]	[0, 0.15]	[0, 0.2]		
3	[1.0, 1.2]	[0, 0.15]	[0, 0.2]		
4	[-2, 2]	[0, 0.15]	[0, 0.2]		
5	[1.0, 1.4]	[0, 0.15]	[0, 0.2]		
6	[1.5, 2.0]	[0, 0.15]	[0, 0.2]		
7	4.92 eV - $\sum_{i \neq 7} \Delta G^0_{\text{r,i}}$	[0, 1.65]	[0, 0.2]		
-				$[8 \cdot 10^{-5}, 20 \cdot 10^{-5}]$	[18, 20]

The ranges of the reaction free energy values of the electrochemical steps were set in such way that they are able to reproduce the features in the CV e.g. the peak positions. For chemical steps, the ranges of the reaction free energies were selected in between wider limits, as they are not

[11] Parts of this section have been published in the supporting information of the following article:
[1] **Geppert, J.**; Röse, P.; Czioska, S.; Escalera-López, D.; Boubnov, A.; Saraçi, E.; Cherevko, S.; Grunwaldt, J.-D.; Krewer, U. *J. Am. Chem. Soc.* **2022**, *144*, 13205-13217.

easily specifiable by the experimental current response. The reaction free energy of the oxygen detachment (step 7: $^{*}OO \rightarrow {}^{*} + O_2$) is constrained by the thermodynamic formation energy $\sum \Delta G_r^0 = 4.92$ eV of the overall OER ($2H_2O \rightarrow 2H_2 + O_2$). As a consequence of the definition of the pre-exponential frequency factor k_0 = 343.2 s^{-1}, the lower limits of the activation free energies were set to ΔG_a = 0 eV as described in section 2.5. The upper limits are assumed to a value of 0.15 eV, since no significant peak to peak difference is observable in the CV of the pristine IrO_2 material. One exception is the oxygen detachment (step 7: $^{*}OO \rightarrow {}^{*} + O_2$) which was found by DFT calculations to have an activation energy up to 0.58 eV[44, 47] and, thus, the respective activation free energy upper limit was increased to 1.65 eV. Lower and upper limits of the interaction energies of adsorbed species were set to 0 eV and 0.2 eV, respectively. The density of active sites and the double layer capacitance were found suitable to describe the experimental data of pristine IrO_2 in the ranges of $[8 \cdot 10^{-5}, 20 \cdot 10^{-5}]$ mol m^{-2} and [18, 20] F m^{-2}, respectively and were used to define the design space.

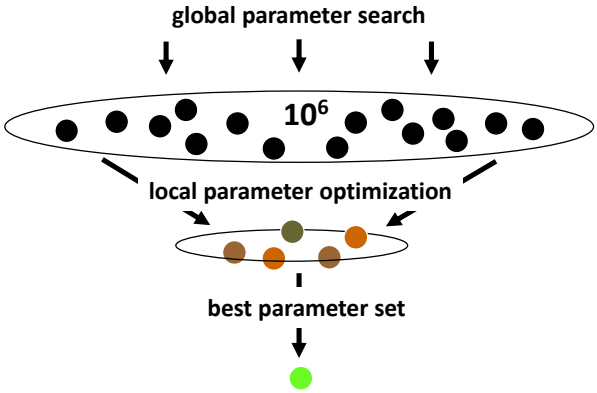

Figure A.1: Schematic illustration of the two-step parameter identification process including the global parameter search of 10^6 randomly selected sets of parameters and the local parameter optimization of the best sets.

The optimization process was conducted in two steps, as illustrated in Figure A.1. In a first step, the dynamic simulations were performed by randomly defining 10^6 sets of parameters within suitable ranges shown for pristine IrO_2 in Table A.1. In a second step, the sets of parameters with the lowest rmse values were locally optimized by the use of a pattern search algorithm i. e. *patternsearch* provided by MATLAB. This algorithm requires higher computational costs and was, hence, only applied on the most promising sets of parameters. The simulation data gained with the best optimized set matches the experimental data of pristine IrO_2 exceptionally well with a rmse value of only 0.066 mA cm^{-2}. The simulation results and the parameter values are shown in Figure 4.5 and in Table 4.1, respectively.
The pattern search algorithm was also applied to identify the model parameter values of the

steadily degrading catalytic system. Successively, the CV curves which were measured after each 30 minutes of operation at 1.6 V were used as input data in the objective function to minimize the rmse. In every step, the values from the previously optimized set served as initial parameters. The simulation results are shown in Figure 4.12.

A.3 Profile rmse Analysis[12]

The profile rmse analysis was conducted to ensure parameter identifiability of the reaction energy values. The method follows the profile likelihood analysis described elsewhere[147, 148] but uses the rmse instead of the likelihood as a measure of deviation. Therefore, the free reaction energy parameters were successively variated from the identified value found by the method described in section 4.3, each by values of {(-0.2); -0.1; -0.05; 0; 0.05; 0.1; (0.2)} eV. Values in brackets are only used for $\Delta G_{r,4}$ and $\Delta G_{r,7}$ on IrO_2. Then, the rmse was minimized by the pattern search algorithm, which was applied for all other parameters, each with 25,000 objective function iterations.

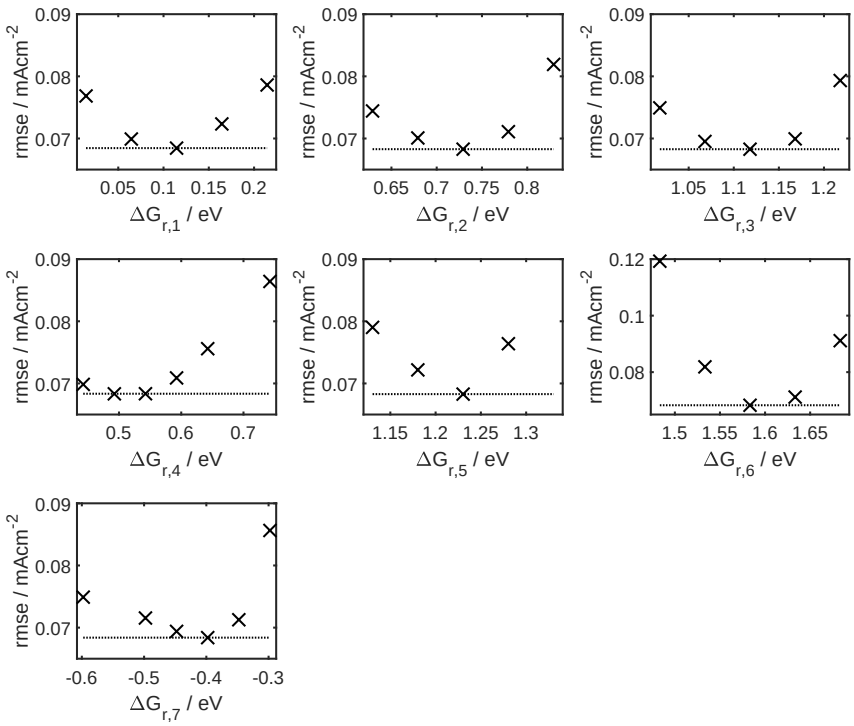

Figure A.2: Rmse profile analysis of the reaction free energy parameters of the OER mechanism on IrO_2. The dotted line indicates the lowest value gained by pattern search optimization.

[12] The graphs in this section have been published in the following article:
[2] **Geppert, J.**; Röse, P.; Pauer, S.; Krewer, U. *ChemElectroChem* **2022**, *10*, e202200481.

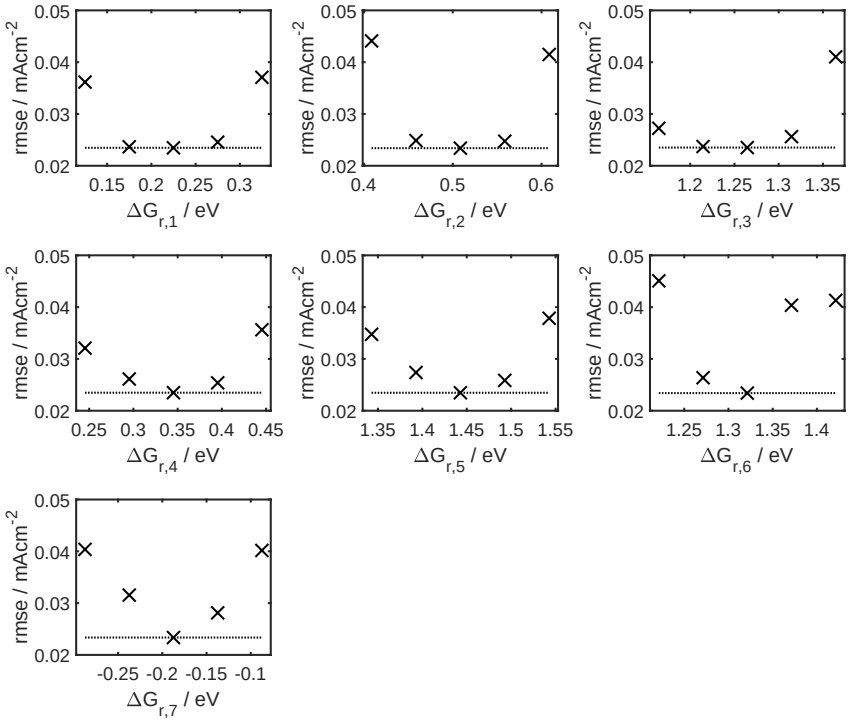

Figure A.3: Rmse profile analysis of the reaction free energy parameters of the OER mechanism on RuO_2. The dotted line indicates the lowest value gained by pattern search optimization.

In Figures A.2 and A.3, the resulting rmse values for variations of all reaction energy parameters and all optimized variations are given for IrO_2 and RuO_2, respectively. Local minima in the profile rmse are observed, which indicates high identifiability of all analyzed parameters. As the minima in all profile rmse match the rmse found for the identified model parameters, this analysis confirms that optimal reaction free energy values were identified.

A.4 Simulations with Different Scan Rates[13]

Dynamic microkinetic simulations allow for an arbitrary change of the model input, i.e., the applied potential over time. In Figure A.4, the simulated and the measured CV curves prove that the model can reproduce the typical experimental variation in the potential scan rate. In direct comparison, the trend of higher absolute current density with increasing scan rates from 25 up to 200 mV s^{-1} is valid for simulation and experiment in the lower potential range up to 1.45 V vs RHE. Also, the exponential increase in current density at the higher potentials during the OER matches all potential scan rates. Both are in good agreement, proving that the microkinetic model can reproduce this dynamic behavior.

[13] The Graphs in this section have been published in the following articles:
[1] **Geppert, J.**; Röse, P.; Czioska, S.; Escalera-López, D.; Boubnov, A.; Saraçi, E.; Cherevko, S.; Grunwaldt, J.-D.; Krewer, U. *J. Am. Chem. Soc.* **2022**, *144*, 13205-13217.
[2] **Geppert, J.**; Röse, P.; Pauer, S.; Krewer, U. *ChemElectroChem* **2022**, *10*, e202200481.

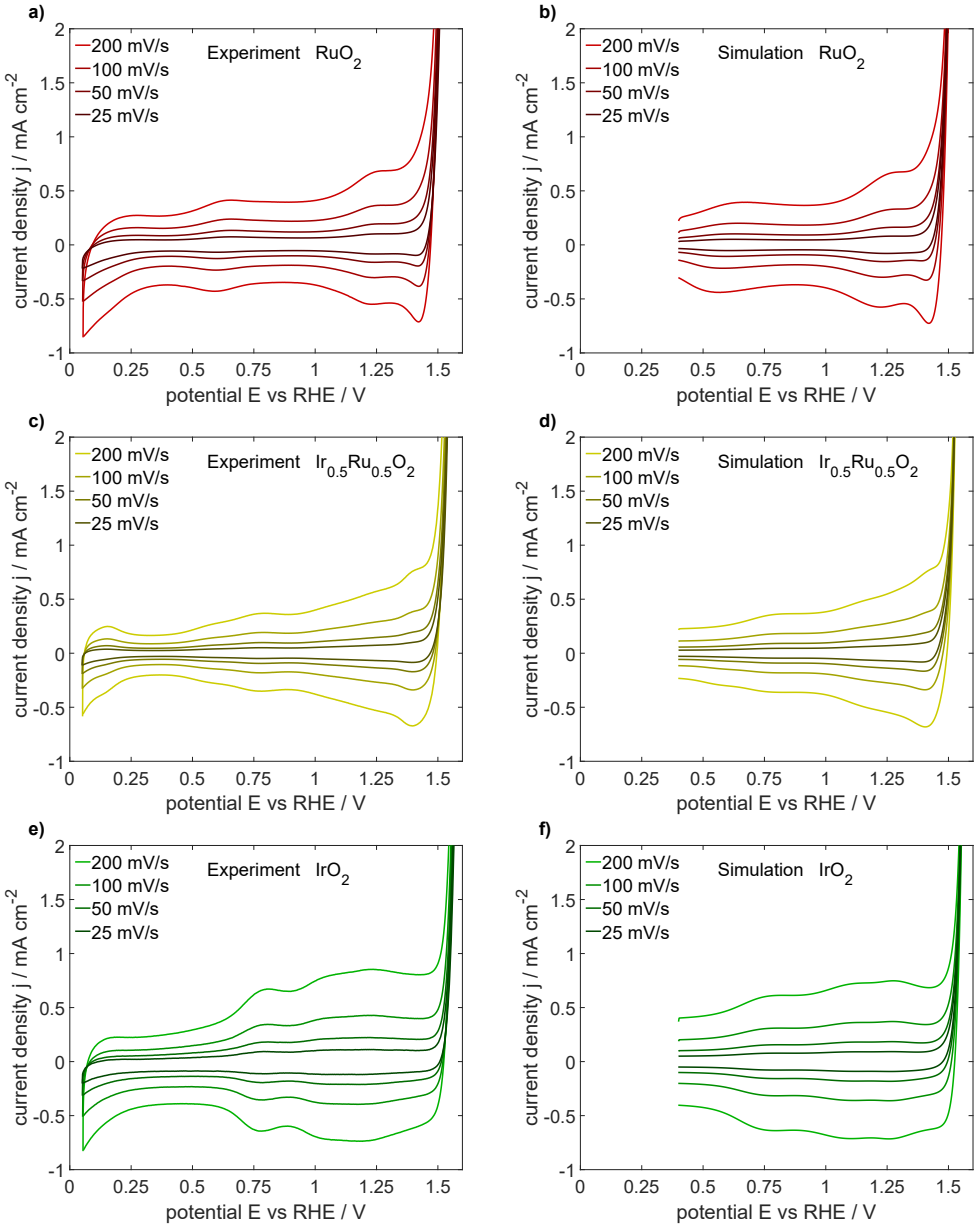

Figure A.4: Experimental a), c), e) and simulated b), d), f) CV curves of the different catalysts at scan rates of 25, 50, 100, and 200 mV s^{-1} in 0.1 M H_2SO_4.

A.5 Simulations with Fixed Energy Values[14]

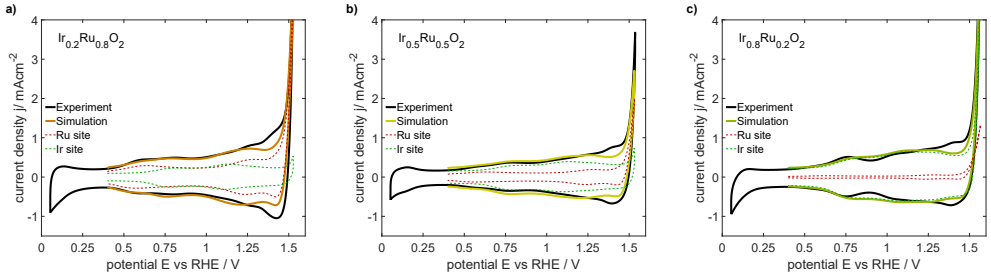

Figure A.5: Experimental and simulated CV curves on the binary oxides a) $Ir_{0.2}Ru_{0.8}O_2$, b) $Ir_{0.5}Ru_{0.5}O_2$, and c) $Ir_{0.8}Ru_{0.2}O_2$ using the same energy parameter set as quantified for the single oxides RuO_2 and IrO_2. High rmse values of 0.155, 0.082, and 0.098 mA cm^{-2} are obtained for the catalysts, respectively, indicating that the assumptions may not be trustworthy. The simulations allow us to distinguish between the processes at the Ru and Ir active sites, which results in the current densities given with dotted red and green lines, respectively.

[14] The graphs in this section have been published in the following article:
[2] **Geppert, J.**; Röse, P.; Pauer, S.; Krewer, U. *ChemElectroChem* **2022**, *10*, e202200481.

A.6 Coverages of Adsorbed Species[15]

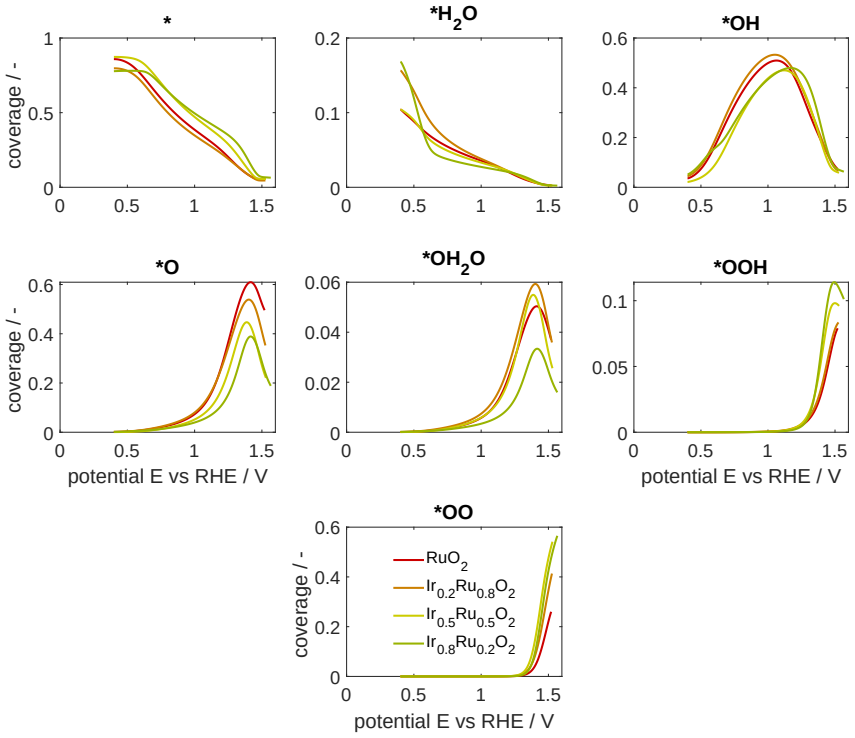

Figure A.6: Surface coverage on Ru sites by intermediate species on RuO_2 and $Ir_xRu_{1-x}O_2$.

[15] The graphs in this section have been published in the following article:
[2] **Geppert, J.**; Röse, P.; Pauer, S.; Krewer, U. *ChemElectroChem* **2022**, *10*, e202200481.

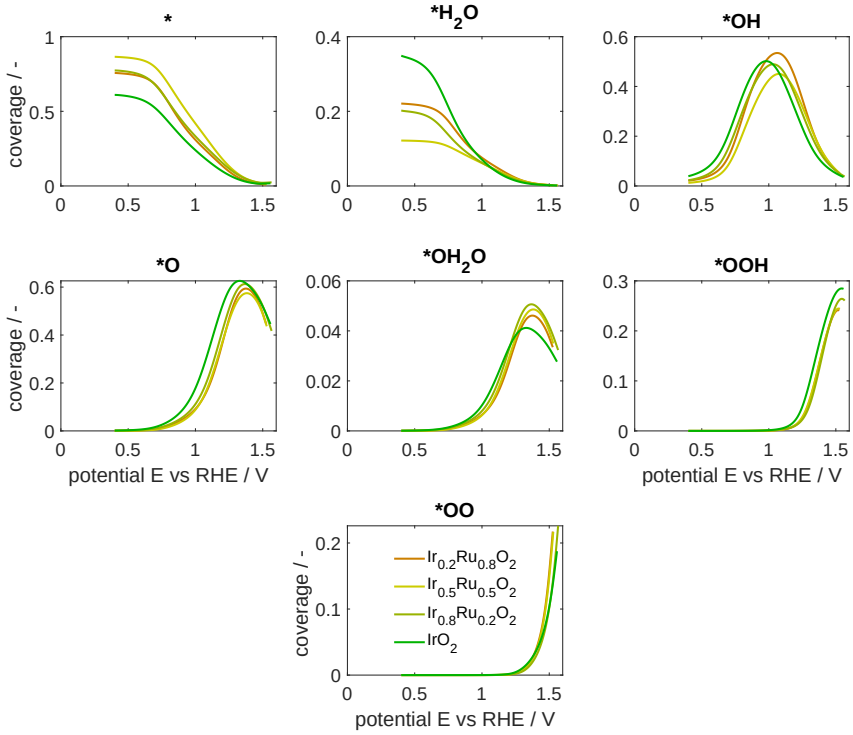

Figure A.7: Surface coverage on Ir sites by intermediate species on IrO_2 and $Ir_xRu_{1-x}O_2$.

A.7 Model Parameter Values[16]

Table A.2: Estimated parameter values of the reaction free energies of the surface processes of intermediate species on RuO_2, IrO_2, and $Ir_xRu_{1-x}O_2$. Please note that only the adsorbed species are indicated in the reaction equations.

Ir site: ΔG_r^0 **/ eV**	RuO_2	$Ir_{0.2}Ru_{0.8}O_2$	$Ir_{0.5}Ru_{0.5}O_2$	$Ir_{0.8}Ru_{0.2}O_2$	IrO_2
$^* \rightarrow {}^*H_2O$		0.15	0.21	0.16	0.11
$^*H_2O \rightarrow {}^*OH$		0.74	0.72	0.71	0.73
$^*OH \rightarrow {}^*O$		1.22	1.21	1.18	1.12
$^*O \rightarrow {}^*OH_2O$		0.44	0.44	0.44	0.54
$^*OH_2O \rightarrow {}^*OOH$		1.27	1.27	1.30	1.23
$^*OOH \rightarrow {}^*OO$		1.55	1.57	1.58	1.58
$^*OO \rightarrow {}^*$		-0.46	-0.50	-0.45	-0.40
Ru site: ΔG_r^0 **/ eV**					
$^* \rightarrow {}^*H_2O$	0.24	0.22	0.27	0.24	
$^*H_2O \rightarrow {}^*OH$	0.51	0.51	0.56	0.51	
$^*OH \rightarrow {}^*O$	1.28	1.26	1.29	1.34	
$^*O \rightarrow {}^*OH_2O$	0.39	0.35	0.28	0.36	
$^*OH_2O \rightarrow {}^*OOH$	1.44	1.44	1.40	1.34	
$^*OOH \rightarrow {}^*OO$	1.37	1.32	1.31	1.37	
$^*OO \rightarrow {}^*$	-0.32	-0.19	-0.19	-0.25	

[16] The data in this section have been published in the following articles:
[1] **Geppert, J.**; Röse, P.; Czioska, S.; Escalera-López, D.; Boubnov, A.; Saraçi, E.; Cherevko, S.; Grunwaldt, J.-D.; Krewer, U. *J. Am. Chem. Soc.* **2022**, *144*, 13205-13217.
[2] **Geppert, J.**; Röse, P.; Pauer, S.; Krewer, U. *ChemElectroChem* **2022**, *10*, e202200481.

Table A.3: Estimated parameter values of the activation free energies of the surface processes of intermediate species on RuO_2, IrO_2, and $Ir_xRu_{1-x}O_2$. Please note that only the adsorbed species are indicated in the reaction equations.

Ir site: ΔG_a / eV	**RuO_2**	**$Ir_{0.2}Ru_{0.8}O_2$**	**$Ir_{0.5}Ru_{0.5}O_2$**	**$Ir_{0.8}Ru_{0.2}O_2$**	**IrO_2**
$^* \rightarrow {}^*H_2O$		0	0	0.15	0.15
$^*H_2O \rightarrow {}^*OH$		0.02	0.06	0.07	0
$^*OH \rightarrow {}^*O$		0	0	0	0
$^*O \rightarrow {}^*OH_2O$		0	0	0	0
$^*OH_2O \rightarrow {}^*OOH$		0	0	0	0
$^*OOH \rightarrow {}^*OO$		0	0	0	0.04
$^*OO \rightarrow {}^*$		0.61	0.54	0.43	0.43
Ru site: ΔG_a / eV					
$^* \rightarrow {}^*H_2O$	0.19	0	0.23	0.30	
$^*H_2O \rightarrow {}^*OH$	0.10	0.19	0.10	0.10	
$^*OH \rightarrow {}^*O$	0	0.10	0.10	0.10	
$^*O \rightarrow {}^*OH_2O$	0.09	0.09	0	0	
$^*OH_2O \rightarrow {}^*OOH$	0	0	0	0	
$^*OOH \rightarrow {}^*OO$	0.02	0	0	0	
$^*OO \rightarrow {}^*$	0.34	0.34	0.34	0.34	

Table A.4: Estimated parameter values of the interaction free energy of the surface adsorbed intermediate species on RuO_2, IrO_2, and $Ir_xRu_{1-x}O_2$.

Ir site: ΔG_{int} / eV	**RuO_2**	**$Ir_{0.2}Ru_{0.8}O_2$**	**$Ir_{0.5}Ru_{0.5}O_2$**	**$Ir_{0.8}Ru_{0.2}O_2$**	**IrO_2**
*		0.19	0	0.10	0.20
*H_2O		0.20	0.20	0.20	0.15
*OH		0.20	0.20	0.12	0.11
*O		0.20	0.18	0.12	0.13
*OH_2O		0.16	0	0	0
*OOH		0	0	0	0.03
*OO		0.20	0.20	0.04	0.01
Ru site: ΔG_{int} / eV					
*	0.00	0.12	0	0	
*H_2O	0.20	0	0	0.20	
*OH	0.13	0.20	0	0.09	
*O	0.06	0.20	0.20	0	
*OH_2O	0.20	0.18	0.20	0.20	
*OOH	0.20	0.20	0.20	0.20	
*OO	0.19	0.20	0	0	

Table A.5: Estimated parameter values of the density of active sites and the double-layer capacitance, both normalized to the geometrical electrode area, and the relative amount of active Ir sites of the RuO_2, the IrO_2, and their mixtures.

	RuO_2	**$Ir_{0.2}Ru_{0.8}O_2$**	**$Ir_{0.5}Ru_{0.5}O_2$**	**$Ir_{0.8}Ru_{0.2}O_2$**	**IrO_2**
ρ / mol m^{-2}	$0.65 \cdot 10^{-4}$	$0.83 \cdot 10^{-4}$	$0.46 \cdot 10^{-4}$	$0.73 \cdot 10^{-4}$	$1.40 \cdot 10^{-4}$
C_{dl} / F m^{-2}	11.05	11.05	11.03	11.03	19.60
x / -	0	0.40	0.70	0.88	1.00